Background Error Estimation in an Atmospheric Limited Area Model

Gergely Bölöni

Ph.D. dissertation

Eötvös Loránd University, Faculty of Science
Ph.D. School for Earth Sciences, Geography-Meteorology Program

School leader: Prof. Dr. Gyula Gábris, D.Sc., MTA
Program leader: Prof. Dr. József Nemes-Nagy, D.Sc., MTA

Thesis advisors:
Dr. Roger Randriamampianina, Ph.D., MTA
Assoc. Prof. Dr. István Matyasovszky, Ph.D., ELTE

Hungarian Meteorological Service
Division for Methodological Developments

2011

Acknowledgments

I would like to thank my two thesis advisors, Roger Randriamampianina and István Matyasovszky, for their kind attention on my work and for making suggestions to improve the final structure and text of my thesis. I am very much grateful for having the possibility to work together with several colleagues experienced in background error modeling through the ALADIN and RC LACE consortia whose advises usually inspired me a lot. I am especially grateful to Loïk Berre and Claude Fischer from whom I have learned almost all what I know on background error modeling and on the ALADIN data assimilation code. I enjoyed to learn from them both through discussions and reading their great papers. I appreciate very much the work done together with Kristian Horvath, on the tuning of background errors during his visits at the Hungarian Meteorological Service during 2004-2006. I would like to thank András Horányi, Gábor Radnóti and Maria Derková to give me the first introduction to NWP and data assimilation and to Edit Adamcsek the useful discussions we had on background error modeling. I appreciate very much the help I have got from Benedikt Strajnar on the preparation of LBC files from the ECMWF Ensemble Data Assimilation experiments used in my thesis, as well as his very detailed and valuable remarks on this text. Finally, I am also very thankful to my colleagues at the NWP team of the Hungarian Meteorological Service for their patience and for letting me concentrate on writing if I needed.

Contents

Chapter 1

Introduction

Numerical Weather Prediction (NWP) is an essential component of modern weather forecasting, providing numerical solution to the atmosphere's governing differential equations, namely the hydro-thermodynamic equations. These partial differential equations are discretized both in time and space and are integrated by numerical methods on computers. As a result, the weather forecast is given in discrete time steps on a three dimensional grid and the system providing the forecast is called the NWP model. A particularly important and interesting area of NWP called atmospheric data assimilation is in the focus of the dissertation, which is the science of estimating the best possible initial conditions (analysis) for the hydro-thermodynamic equations. The importance of starting the forecast from the best possible analysis is extremely high, given the non-linearity of the hydro-thermodynamic equations which imply high sensitivity to the initial conditions.

An essential source of information in data assimilation is the background, which is usually a short-range forecast of the NWP model valid at the analysis time. The background is corrected by the atmospheric observations providing the analysis during the process of data assimilation. Errors of the background are unknown and their estimation is of great importance regarding the success of data assimilation, given the fact that they are taken into account with the aim of giving a proper weight to the background, and thus, implicitly also to the observations. Another aspect that makes the estimation of background errors highly important, is that they are correlated in space, which gives the mean to spread out the information content of the observations in 3 dimensions. Background errors of different meteorological variables are also correlated, which enables multivariate adjustments in the analysis, representing dynamical and physical atmospheric balances.

The thesis focuses on the estimation of background errors, and more specifically on its aspects in a Limited Area Modeling (LAM) framework, namely when the NWP model is integrated over a certain geographical region of the Earth. The experiments discussed were performed with the Hungar-

ian version of the ALADIN [1] LAM (ALADIN/HU) using lateral boundary forcing by the ARPEGE [2] and IFS [3] global NWP systems and the resources of the supercomputer maintained at the Hungarian Meteorological Service (OMSZ) [4]. Also, a great proportion of conclusions and technical developments related to the present work is to be utilized in the operational short range weather forecasting system of OMSZ. The thesis is structured as follows.

Chapter 2 gives an overview of atmospheric data assimilation in general and describes the role of background and observation errors within this field in more detail. Being the NWP system a multi dimensional one, the background and observation errors are taken into account in the form of a covariance matrices. Main properties of these error covariance matrices are described as well as the way they impact the analysis in the process of data assimilation. In the second part of the chapter, particularities of the data assimilation scheme implemented in the ALADIN model are described.

The simulation of background errors is discussed in chapter 3. Background error simulation is known as the process of designing and collecting a statistical sample for the computation of the background error covariance matrix. The challenge is to define and generate a sample, which represent the error of the background corresponding to the given NWP system as much as possible. Background error simulation in a LAM framework raises further issues, which are tackled via extensive experiments in this part of the thesis using the ALADIN/HU system. Background errors are composed of different sources of uncertainties, present in the NWP system. These uncertainties are results of imperfections of the analysis (initial conditions), the lateral boundary conditions (LBC: in case of a LAM, these conditions ensure the adjustment to the driving NWP model at the lateral boundaries) and also the NWP model itself. In the second part of chapter 3, these three counterparts of background uncertainties are simulated and diagnosed in the ALADIN/HU LAM.

Background errors are variable in time, as weather predictability also varies according to the actual season, weather regime or atmospheric flow. This time variation is accounted for in chapter 4 with a rather simplified approach by diagnosing the seasonal variability and the diurnal cycle in the background error covariances of ALADIN/HU.

Chapter 5 is dedicated to the "a posteriori" diagnosis and tuning of the ALADIN/HU background errors. "A posteriori" diagnosis and tuning are methodologies to diagnose and correct deficiencies of the background error covariance matrix, such as variances, standard deviations, correlation length-scales or multivariate adjustments. It is explained and demonstrated that "a posteriori" diagnostics are always relevant, given the fact that the background error simulation and covariance modeling is never perfect.

In chapter 6 technical developments on the ALADIN data assimilation code are described. Namely, improvements of the spatial representation of horizontal correlations are proposed and coded

[1] Aire Limitée Adaptation Dynamique Développement International
[2] Action de Recherche Petite Echelle Grande Echelle
[3] Integrated Forecasting System
[4] OMSZ: Országos Meteorológiai Szolgálat

for ALADIN/HU. The impact of the improved representations is discussed.

Chapter 7 consists of a general discussion of the thesis where the main conclusions of the presented work are drawn.

Chapter 2

Atmospheric data assimilation and the role of background errors

Atmospheric data assimilation is an important area of NWP, which aims at providing the best possible initial conditions for the model forecast. During the process of data assimilation all the available information are combined about the state of the atmosphere within a time period often called the assimilation window. Available information are typically a background state, observations, and known dynamical constraints of the atmosphere. The combination of these information is optimal in a least square sense, which means that the expectation of the difference between the truth and the analysis (i.e. our estimation of the truth) is minimal. The success of data assimilation is particularly important considering the fact that atmospheric processes are of chaotic nature, which implies a large sensitivity of the hydro-thermodynamic equations to the initial conditions.

2.1 Data assimilation based on the optimal estimation theory

In order to explain the principle of data assimilation, let us introduce the following notations:

- $\mathbf{x}$: the model state, i.e. the atmospheric state described by the model
- $\mathbf{x}_t$: the truth, i.e. the true atmospheric state on the model grid
- $\mathbf{x}_a$: the analysis, i.e. our estimation of the truth valid at the time we want the forecast to start
- $\mathbf{x}_b$: the background, i.e. a short range model forecast valid at the analysis time
- $\mathbf{y}$: the observations of the atmosphere available in the assimilation window
- H: $\mathbf{x} \mapsto \mathbf{y}$ the observation operator mapping from the model space to the observation space

It is important to mention that the vectors $\mathbf{x}$, $\mathbf{x}_t$, $\mathbf{x}_b$ and $\mathbf{x}_a$ are all of dimension of 10^7 as they contain the prognostic variables of the hydro-thermodynamic equations (typically surface pressure, wind, temperature and humidity) on the three dimensional regular grid of the model. The vector of the observations ($\mathbf{y}$) is of dimension of 10^5 including surface, radiosonde and aircraft data as well as remotely sensed data, such as satellites, wind profilers, GPS or radars. The spatial distribution of observations is irregular and their locations does not match the model grid-points in most of the cases. The observation operator H thus maps from the 10^7 dimensional space of the model ($\mathbf{x}$) to the 10^5 dimensional space of the observations ($\mathbf{y}$), making possible to compare these informations.

Neither the background nor the observations describe the atmosphere perfectly. Their errors are defined by their distance from the true state:

$$\mathbf{e}_b = \mathbf{x}_t - \mathbf{x}_b \tag{2.1}$$

$$\mathbf{e}_o = H\mathbf{x}_t - \mathbf{y} \tag{2.2}$$

Being the errors defined, their covariance matrices can be written as:

$$\mathbf{B} = E[\mathbf{e}_b, \mathbf{e}_b{}^T] \tag{2.3}$$

$$\mathbf{R} = E[\mathbf{e}_o, \mathbf{e}_o{}^T] \tag{2.4}$$

where $E[...]$ stands for the statistical expectation and ^{T} for the transpose ($\mathbf{e}_b \sim 10^7, \mathbf{B} \sim 10^7 * 10^7$ and $\mathbf{e}_o \sim 10^5, \mathbf{R} \sim 10^5 * 10^5$). It can be shown, that assuming unbiased observations and background ($E[\mathbf{e}_o] = E[\mathbf{e}_b] = 0$) with Gaussian error distribution, the maximum likelihood estimation for the analysis $\mathbf{x}_a$ is equivalent with the minimization of the so-called variational cost function with respect to $\mathbf{x}$:

$$J(\mathbf{x}) = J_o(\mathbf{x}) + J_b(\mathbf{x}) \tag{2.5}$$

$$= \frac{1}{2}(\mathbf{x} - \mathbf{x}_b)^T\mathbf{B}^{-1}(\mathbf{x} - \mathbf{x}_b) + \frac{1}{2}(\mathbf{y} - H\mathbf{x})^T\mathbf{R}^{-1}(\mathbf{y} - H\mathbf{x}) \tag{2.6}$$

$$\mathbf{x}_a = arg\ min\ J(\mathbf{x}) \tag{2.7}$$

An intuitive interpretation of the above variational estimation ([47] *Lorenc* 1986, [61] *Thépaut and Courtier* 1991, [5] *Bouttier and Courtier* 1999) is as follows. The terms J_o and J_b of the right hand side measure the distance of the analysis from the background and from the observations respectively, normalized by their error covariance matrices $\mathbf{B}$ and $\mathbf{R}$. This implies that all the available information in the analysis is taken into account according to its reliability. As $J(\mathbf{x})$ is a quadratic form, its minimum is found if its gradient with respect to $\mathbf{x}$ is zero:

$$\nabla_{\mathbf{x}} J(\mathbf{x}_a) = 0 \tag{2.8}$$

Taking the gradient of $J(\mathbf{x})$ with respect to the vector $\mathbf{x}$, one gets the so-called analysis equation:

$$\mathbf{x}_a = \mathbf{x}_b + \mathbf{K}(\mathbf{y} - H\mathbf{x}_b) \tag{2.9}$$

with

$$\mathbf{K} = \mathbf{B}\mathbf{H}^T(\mathbf{H}\mathbf{B}\mathbf{H}^T + \mathbf{R})^{-1} \tag{2.10}$$

where the matrix $\mathbf{H}$ is the Jacobian (tangent linear) and $\mathbf{H}^T$ is the conjugate transpose (adjoint) of H. One has to note here that the observation operator H is often non-linear in practice, namely in case of remote sensing data (e.g. satellites, radar data) where the observed quantity (e.g. radiance, reflectivity) is related to the model state (temperature, pressure, wind, humidity) in a complicated and non-linear way. However, in the analysis equation (2.9) it is assumed that the observation operator H can be linearized around the background state $\mathbf{x}_b$ for increments $\delta\mathbf{x}$ in the range of $\mathbf{x}_a - \mathbf{x}_b$, that is $H\mathbf{x}_a - H\mathbf{x}_b \approx \mathbf{H}(\mathbf{x}_a - \mathbf{x}_b) = \mathbf{H}\delta\mathbf{x}$.

It might be an important remark that the analysis equation (2.9) can be deduced with the least square estimation as well (besides the maximum likelihood estimation). In the least square estimation the analysis is assumed to be a linear combination of the observations and the background. The weights of the linear combination are to be estimated with the condition that the squared error of the analysis should be minimal i.e. $E[(\mathbf{x}_t - \mathbf{x}_a)^2] = 0$. With the assumption of unbiased background and observations ($E[\mathbf{e}_o] = E[\mathbf{e}_b] = 0$) the least-square estimation gives the analysis equation (2.9) with the same $\mathbf{K}$ weighting matrix as given by (2.10).

In this interpretation the analysis equation (2.9) can be seen as the correction of the background field $\mathbf{x}_b$ by the observation increments $\mathbf{y} - H\mathbf{x}_b$ (innovations) weighted by the matrix $\mathbf{K}$ (Kalman gain). Taking into account the form of $\mathbf{K}$, one has to notice that the correction $\delta\mathbf{x} = \mathbf{x}_a - \mathbf{x}_b$ (analysis increment) is mainly determined by the reliability of the background and the observations again, which are represented respectively by the inverse of the error covariance matrices $\mathbf{B}$ and $\mathbf{R}$.

In line with the two interpretations above (the variational cost function (2.6) and the analysis equation (2.9 and 2.10)) one may recognize that the error covariance matrices $\mathbf{B}$ and $\mathbf{R}$ are of crucial importance in the analysis process. We refer to the next section for expressing the role of these covariance matrices in more detail.

2.2 The role of error covariance matrices

In order to give a more detailed interpretation of the role of the error covariance matrices $\mathbf{B}$ and $\mathbf{R}$, we propose to study the analysis equation (2.9)-(2.10) in the following simplified system. Let our model grid to consist of two grid-points i and j. Our vector of background field $\mathbf{x}_b$ can then be expressed by components as $(x_{b,i}, x_{b,j})^T$. Let y be a single observation taken exactly in the grid-point j. Let us assume that the error variances of the background are known and that they are the same in both grid-points , that is $\sigma^2_{b,i} = \sigma^2_{b,j} = \sigma^2_b$. Also we consider the background error covariance between the two grid-points $cov_b = cov_{b,(i,j)} = cov_{b,(j,i)}$ to be known, as well as the observation error variance σ^2_o.

In this simple case the matrices $\mathbf{H}$,$\mathbf{B}$ and $\mathbf{R}$ read as:

$$\mathbf{H} = \begin{pmatrix} 0 & 1 \end{pmatrix} \quad \mathbf{B} = \begin{pmatrix} \sigma_b^2 & cov_b \\ cov_b & \sigma_b^2 \end{pmatrix} \quad \mathbf{R} = \sigma_o^2 \tag{2.11}$$

which implies the following form of the analysis equation (2.9)-(2.10):

$$\begin{pmatrix} x_{a,i} \\ x_{a,j} \end{pmatrix} = \begin{pmatrix} x_{b,i} \\ x_{b,j} \end{pmatrix} + \begin{pmatrix} \frac{cov_b}{\sigma_b^2+\sigma_o^2} \\ \frac{\sigma_b^2}{\sigma_b^2+\sigma_o^2} \end{pmatrix} (y - x_{b,j}) \tag{2.12}$$

Let us denote the analysis increments $(x_{a,i} - x_{b,i})$ and $(x_{a,j} - x_{b,j})$ by δx_i and δx_j respectively, while the innovation $(y - x_{b,j})$ by Δy_j emphasizing that the innovation is understood in grid-point j. Now writing up the equation (2.12) by components, one gets:

$$\delta x_i = \frac{cov_b}{\sigma_b^2 + \sigma_o^2} \Delta y_j \tag{2.13}$$

$$\delta x_j = \frac{\sigma_b^2}{\sigma_b^2 + \sigma_o^2} \Delta y_j \tag{2.14}$$

Expressing Δy_j from equation (2.14) and writing it to equation (2.13), one gets:

$$\delta x_i = corr_b \quad \delta x_j \tag{2.15}$$

where $corr_b = cov_b/\sigma_b^2$ is the background error correlation between the grid-points i and j. The following physical interpretation is valid for the above equations. Equation (2.13) shows how the innovation in grid-point j is propagated to an analysis increment in grid-point i. This process can be seen as two consecutive steps ([19] *Daley* (1991)). Namely, equation (2.14) can be interpreted as a first step generating the analysis increment in grid-point j by weighting the innovation with a factor of $\frac{\sigma_b^2}{\sigma_b^2+\sigma_o^2}$. As this factor is smaller than one (given the fact that both σ_b^2 and σ_o^2 are positive), the analysis increment δx_j is always smaller than the innovation Δy_j. This implies that this step is often understood as a filtering step because the information content of the observation is filtered while generating a correction on the background. The equation (2.15) then propagates the increment δx_j in space, namely into the grid-point i, which gives δx_i. That is why this step is often called as the propagation step. The propagation is determined by $corr_b$, which is the background error correlation between the grid-points i and j. Given the fact that $|corr_b| < 1$ by definition, δx_i will be smaller than δx_j, which is in accordance with our intuition that the observation y, which is located in grid-point j will have a larger influence on the analysis increment at this point than on the analysis increment in grid-point i.

Following [11] *Berre* (2001) and [37] *Hollingsworth* (1987) the filtering and propagation steps can be identified in the multidimensional case as well by multiplying the analysis equation (2.9) by $\mathbf{HBH}^T$ and its inverse:

$$\delta\mathbf{x} = \mathbf{BH}^T(\mathbf{HBH}^T)^{-1}(\mathbf{HBH}^T)(\mathbf{HBH}^T + \mathbf{R})^{-1}\mathbf{d} \tag{2.16}$$

where $\delta\mathbf{x}$ and $\mathbf{d}$ denote respectively the analysis increment ($\mathbf{x}_a - \mathbf{x}_b$) and the innovation ($\mathbf{y} - H\mathbf{x}_b$). Here the multiplication by $(\mathbf{HBH}^T)(\mathbf{HBH}^T + \mathbf{R})^{-1}$ filters the innovations turning them into analysis increments at the observation locations, while the multiplication by $\mathbf{BH}^T(\mathbf{HBH}^T)^{-1}$ represents the spatial propagation of the analysis increments from the observation locations onto the model grid. The filtering step involves only the error covariances of the observations $\mathbf{R}$ and those of the background mapped to the observation space $\mathbf{HBH}^T$, that is, in this step only analysis increments at observation locations are generated. The propagation step then transforms the analysis increments provided at the observation locations into analysis increments at model grid-points implied by the matrix $\mathbf{BH}^T$, which represent the background error covariances between the observation locations and the model grid-points. In addition a normalization by the background error variances mapped to the observation space is done (multiplication by $(\mathbf{HBH}^T)^{-1}$), so that the increment due to the propagation step remains limited in the range $[-1, 1]$. With other words, the propagation step is realized practically through the background error correlations and not the covariances. One has to note here that the propagation step can be understood more generally, than it is explained above. Besides the spatial propagation, the analysis increment of a certain atmospheric variable (e.g. temperature) can be transformed into an analysis increment of another variable (e.g humidity) if the background error correlations between the different variables are known. Such transformation is usually called as the multivariate propagation of the analysis increment.

The above evaluation points out that the observation error covariance matrix $\mathbf{R}$ has a role in the filtering step only, while the background error covariance matrix $\mathbf{B}$ is in play in the propagation step too (besides the filtering step). In today's assimilation systems a usual simplification is that zero covariances are assumed between observation errors at different locations and also between observation errors of different atmospheric variables or instruments. This highly simplifies the observation error covariance matrix $\mathbf{R}$, namely into a diagonal matrix involving observation error variances for the observed variables only. On the other hand the background error covariance matrix $\mathbf{B}$ is non diagonal and involves both spatial and multivariate covariances of the background errors. This is what gives chance the observed information to spread out in space and also to be transformed in a multivariate sense. It is then rather sensible that the modeling of the matrix $\mathbf{B}$ is of high importance.

2.3 Sources of uncertainties in the background forecast and a general formulation of the background error covariance matrix

In order to review the uncertainties involved in background errors, a general formulation of the background error covariance matrix is given in this section after [43] *Kalman* (1960) and [44] *Kalnay*

(2003). Let us denote the operator of the forecast model by M, which describes the time propagation of the atmospheric state by solving the hydro-thermodynamic system of equations. Using this notation the relation between the background and the analysis state can be formulated as:

$$\mathbf{x}_b^{(i)} = M\mathbf{x}_a^{(i-1)} \tag{2.17}$$

where the index i stands for the time sequence of assimilation steps in the data assimilation cycle. Then, similarly to equations (2.1)-(2.2) one can define the analysis and model errors as follows:

$$\mathbf{e}_a^{(i-1)} = \mathbf{x}_a^{(i-1)} - \mathbf{x}_t^{(i-1)} \tag{2.18}$$

$$\mathbf{e}_M^{(i)} = M\mathbf{x}_t^{(i-1)} - \mathbf{x}_t^{(i)} \tag{2.19}$$

The analysis error is thus defined as the difference of the analysis from the truth, while the model error is defined as the difference from the truth at time i caused by the model forecast starting from the truth as initial state at time $i-1$. Arranging equation (2.19) to $\mathbf{x}_t$ and subtracting it from equation (2.17), one gets:

$$\mathbf{x}_b^{(i)} - \mathbf{x}_t^{(i)} = M\mathbf{x}_a^{(i-1)} - M\mathbf{x}_t^{(i-1)} + \mathbf{e}_M^{(i)}, \tag{2.20}$$

which, under the assumption of the linearity of M (mostly valid for short forecast ranges) can be written as:

$$\mathbf{e}_b^{(i)} = M(\mathbf{x}_a^{(i-1)} - \mathbf{x}_t^{(i-1)}) + \mathbf{e}_M^{(i)} \tag{2.21}$$

$$= M\mathbf{e}_a^{(i-1)} + \mathbf{e}_M^{(i)} \tag{2.22}$$

The above equation shows that, in general, the background error consists of two components:

- the time propagation of the initial (analysis) uncertainty (error) $M\mathbf{e}_a^{(i-1)}$
- the model uncertainty (error) $\mathbf{e}_M^{(i)}$

Writing the formula of $\mathbf{e}_b^{(i)}$ above to the definition of the background error covariance matrix (2.3), and assuming that initial and model errors are uncorrelated, one gets:

$$E[\mathbf{e}_b^{(i)}\mathbf{e}_b^{(i)^T}] = E[(M\mathbf{e}_a^{(i-1)} + \mathbf{e}_M)(M\mathbf{e}_a^{(i-1)} + \mathbf{e}_M^{(i)})^T] \tag{2.23}$$

$$= ME[\mathbf{e}_a^{(i-1)}\mathbf{e}_a^{(i-1)^T}]M^T + E[\mathbf{e}_M\mathbf{e}_M^{(i)^T}] \tag{2.24}$$

that is,

$$\mathbf{B}^{(i)} = M\mathbf{A}^{(i-1)}M^T + \mathbf{Q}^{(i)} \tag{2.25}$$

where $\mathbf{A}^{(i-1)}$ denotes the analysis error covariance matrix at time $i-1$ and $\mathbf{Q}^{(i)}$ denotes the model error covariance matrix. Note that the above equation (2.25) together with the analysis equation (2.9) frames the Kalman Filter theory. It reflects that the background error covariance matrix $\mathbf{B}$ valid at time i can be computed as the sum of the time propagation of the analysis error covariance matrix $\mathbf{A}$ valid at time $i-1$ and the model error covariance matrix $\mathbf{Q}$ valid at time i.

2.4 The background term in the ALADIN limited area model

This section gives an overview of the background error covariance matrix as it is implemented in the ALADIN model. This is done without the claim of completeness, that is, only the most important aspects are described, which are needed to follow the thesis. For a more complete description of the ALADIN background constraint we refer to [10] *Berre* (2000) and to [53] *Rabier et al.* (1998). For more information on the implementation of the ALADIN LAM in general, see [42] *Joly* (1992), [14] *Bubnová et al.* (1993), [54] *Radnóti et al.* (1995), [39] *Horányi et al.* (1996).

2.4.1 The lateral boundary forcing

ALADIN is a limited area model (LAM). It means, that it is applied for regional forecasts, focusing on a certain geographical region of the Earth, instead of solving the prediction problem for the whole globe. As a consequence, in a LAM, the solution of the hydro-thermodynamic equation requires boundary conditions defined on the borders of the given geographical region. These lateral boundary conditions (LBCs) are additional to the top and bottom boundary conditions and to the initial conditions, which are essential in global models too. The physical importance of the LBCs is to synchronize the LAM atmospheric flow with the "outer world", that is, with the atmospheric processes, which are going on outside the region of interest of the LAM. The LBCs for a LAM are usually provided by a simultaneous global forecast, or by another LAM covering a larger region. The model, which provides the LBCs for a LAM is often called a driving model or a host model and the adjustment of the LAM and the LBCs is called coupling. In ALADIN, the coupling is done by the Davies's relaxation scheme ([20] *Davies* 1976). This scheme defines a so called coupling zone (C) around the area of interest (I zone) as also shown in Fig.2.1 (E stands for extension zone, which will be explained in the next section). The C zone is where a smooth relaxation of the LAM fields to the LBCs is done according to the following formula:

$$\mathbf{x}^C = \alpha \mathbf{x}^I + (1-\alpha)\mathbf{x}^{LBC} \tag{2.26}$$

where $\mathbf{x}^I$ is the LAM state, $\mathbf{x}^{LBC}$ is the driving model's state and $\mathbf{x}^C$ is the LAM fields adjusted (coupled) to the LBCs. The function α goes smoothly from 1 to 0 in the C zone from the interior to the exterior. The C zone comprises typically 8 grid-points in the ALADIN model. The LBCs are available with a 3 hourly frequency, however in between, a time interpolation is applied so that the Davies's relaxation can be performed at each time-step (5 minutes in case of ALADIN/HU) during the forecast.

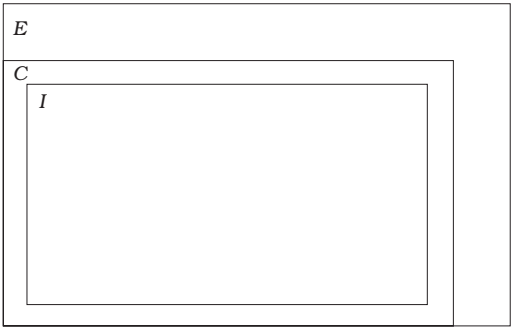

Figure 2.1: Schematic figure of the horizontal geometry in the ALADIN model

2.4.2 The horizontal representation of background errors

The ALADIN model is a spectral LAM. This means that besides the grid-point (or physical) space, meteorological fields are also represented in the so-called spectral space given the bi-Fourier transform ([42] *Joly* 1992):

$$x^z_{m,n} = \frac{1}{JK} \sum_{j=0}^{J-1} \sum_{k=0}^{K-1} x^z_{j,k} e^{-im(2\pi/J)j} e^{-in(2\pi/K)k} \tag{2.27}$$

The notation $x_{m,n}$ stands for the spectral coefficient corresponding to the wavenumber pair (m, n) where m is the wavenumber in x (quasi-latitudinal) and n is the wavenumber in y (quasi-meridional) direction on the Cartesian plane. The notation $x_{j,k}$ stands for the grid-point representation of the model state on a given model level z where J and K are the number of grid-points in the x and y directions. The grid-point representation is reconstructed from the spectral coefficients through the inverse bi-Fourier expansion:

$$x^z_{j,k} = \sum_{m=-M}^{M} \sum_{n=-N}^{N} x^z_{m,n} e^{ij(2\pi/L_x)m} e^{ik(2\pi/L_y)n} \tag{2.28}$$

where M and N are the maximal wavenumbers for m and n, while L_x and L_y denote the size of the LAM domain in x and y directions. Thus each grid-point value is constructed as the sum (superposition) of all Fourier waves in that given point, with amplitudes defined by the corresponding spectral coefficient $x_{m,n}$. The truncation of the inverse bi-Fourier transform (the choice of M and N) is elliptic in the ALADIN model (Fig.2.2), that is:

$$\frac{m^2}{M^2} + \frac{n^2}{N^2} \leq 1 \tag{2.29}$$

The Fourier transform is applicable only on fields, which are periodic over the LAM domain ($C + I$

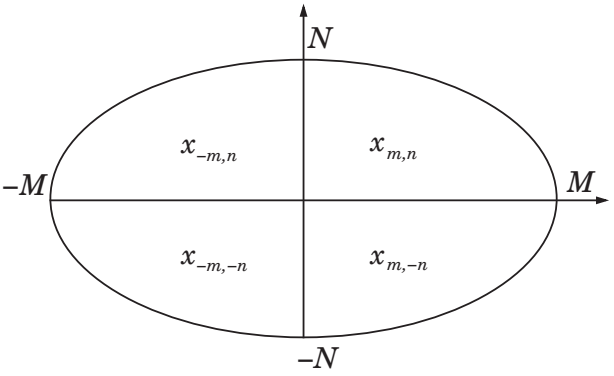

Figure 2.2: The spectral representation of meteorological fields in the ALADIN model

zones in Fig.2.1). As this not necessarily fulfilled, an extension zone (E in Fig.2.1) is also defined where the model fields are smoothly relaxed from their actual values to their values on the opposite side of the $C + I$ zones. As the bi-Fourier expansion describes the meteorological variables as a trigonometric function of the space (in both x and y directions), it offers a reasonable physical analogy for the decomposition of meteorological processes into wave motions, as also often applied in dynamic meteorology ([38] *Holton* 2004, [34] *Götz and Rákóczi* 1981, [52] *Práger* 1982). This implies that in the Fourier decomposition, small wavenumbers can be related to large scale, while large wavenumbers to small scale meteorological processes.

In the ALADIN model a large part of the computations are performed in spectral space instead of the grid-point (or physical) space. Such is the computation of the background term in the variational cost function (2.6) for instance. As a consequence, the background error covariance matrix $\mathbf{B}$ is also computed in spectral space, which makes necessary to explain how covariance computations are done in the Fourier representation. Let (j, k, z) and $(j + \Delta x, k + \Delta y, z')$ be two different locations (grid-points). Following [10] *Berre* (2000), similarly to equations (2.27)-(2.28), the background error covariance of the variables T and q (e.g. temperature and specific humidity) between these two physical locations can be given by the spectral covariances as follows:

$$\overline{T^z_{j,k} q^{z'}_{j+\Delta x,k+\Delta y}} = \sum_{m=-M}^{M} \sum_{n=-N}^{N} \overline{T^z_{m,n} q^{z'*}_{m,n}} e^{2\pi i (\frac{m\Delta x}{L_x} + \frac{n\Delta y}{L_y})} \tag{2.30}$$

where the over-bar stands for the mean (i.e. for the expectation) and * for the complex conjugate. In the current operational versions of the ALADIN model the horizontal structure of background error covariances is assumed to be homogeneous (independent of the geographical location). It can be shown that this assumption implies that the covariances between different (m, n) wavenumber pairs

are zero, that is:

$$\overline{T^z_{m,n} q^{z'*}_{m',n'}} = \delta^{m'}_{m} \quad \delta^{n'}_{n} \quad \overline{T^z_{m,n} q^{z'*}_{m,n}} \tag{2.31}$$

where δ is the Kronecker symbol. Note that this is why in equation (2.30) the indices m and n are the same for both spectral coefficients too. Another assumption applied on the horizontal structure of background error covariances in the ALADIN model is isotropy (independence on the horizontal direction). Under this assumption the spectral covariance computation is further simplified by computing covariances for each total wavenumber k^*:

$$C_{k^*}(T^z, q^{z'}) = \frac{1}{K} \sum_{m,n \leftrightarrow k_*} \overline{T^z_{m,n} q^{z'*}_{m,n}} \tag{2.32}$$

with

$$k^* = N \sqrt{\frac{m^2}{M^2} + \frac{n^2}{N^2}} \tag{2.33}$$

where the sum in equation (2.32) denotes the summation for those (m, n) wavenumbers that correspond to the same k^* total wavenumber and K is the number of such wavenumber pairs. In case of computing the covariance (2.32) on a single vertical level for a single variable (e.g. temperature), the $C_{k^*}(T, q)$ covariance becomes rather a $V_{k^*}(T)$ variance, which depends only on the total wavenumber k^*. As mentioned earlier, the total wavenumber k^* is in correspondence with horizontal spatial scales in the physical space through the Fourier decomposition (small wavenumbers belong to large scales while large wavenumbers to small scales). Thus the V_{k^*} and C_{k^*} spectral variances and covariances corresponding to a given total wavenumber k^* will imply horizontal spatial covariances in the physical space between points with separation distances corresponding to the given k^*.

When discussing horizontal structure functions, one has to mention that there is an ongoing research in order to relax the assumptions of homogeneity and isotropy in the ALADIN model. The goal of this research is to represent more realistic horizontal structures through the involvement of the Wavelet and grid-point representations of background error covariances ([21] *Deckmyn and Berre* 2005). This research area is however beyond the subject of the thesis, therefore the Fourier spectral representation will be used and discussed all along the presented results.

2.4.3 The multivariate adjustment in the background constraint

The ALADIN background constraint is designed for a multivariate analysis, that is to enable the adjustment of the different meteorological variables to each other in the process of analysis. This also implies that an observation of a given variable (e.g. wind) will propagate into analysis increments of other variables (e.g. temperature or humidity), in the way shown in Section 2.2. The multivariate propagation is ensured by cross-covariances of background errors between the meteorological

variables. In the ALADIN model the background errors and analysis increments are assumed to be composed from an unbalanced and from a balanced part. The unbalanced part stands for the part that changes independently from all the other variables, while the balanced part is the one adjusting to the changes of an other variable. The model of increment adjustment is given by the following set of linear regression equations:

$$\begin{aligned} \zeta &= \zeta & (2.34)\\ \eta &= \eta_b + \eta_u = \mathbf{M}\mathcal{H}\zeta + \eta_u & (2.35)\\ (T, P_s) &= (T, P_s)_b + (T, P_s)_u = \mathbf{N}\mathcal{H}\zeta + \mathbf{P}\eta_u + (T, P_s)_u & (2.36)\\ q &= q_b + q_u = \mathbf{Q}\mathcal{H}\zeta + \mathbf{R}\eta_u + \mathbf{S}(T, P_s)_u + q_u & (2.37) \end{aligned}$$

The notations ζ, η, T, P_s, q stand for vorticity, divergence, temperature, surface pressure and specific humidity increments with the subscripts $_b$ and $_u$ standing for the balanced and unbalanced parts. Temperature and surface pressure are treated together as a mass variable. The operator $\mathcal{H}$ is called the horizontal balance operator that transforms vorticity into its part corresponding to the geostrophic wind. This is realized through a linear regression between geopotential and vorticity in spectral space: $\phi_{k^*} = \beta_{k^*}\zeta_{k^*}$, which represents the geostrophic balance equation $\Delta\phi = f_o\zeta$ in the physical space. Thus, the operator $\mathcal{H}$ is a diagonal matrix composed by the regression coefficients β_{k^*} that are in fact the spectral cross-correlations between geopotential and vorticity. The matrices $\mathbf{M}, \mathbf{N}, \mathbf{P}, \mathbf{Q}, \mathbf{S}$ are called vertical balance operators and they consist of the vertical cross-covariances between the variables in play (e.g. $\mathbf{P}$ contains the vertical cross-covariances between temperature and unbalanced divergence).

2.4.4 The control vector space

Let us recall the J_b term of the cost function (2.6) and write it up in the incremental form with the notation $\mathbf{x} - \mathbf{x_b} = \delta\mathbf{x}$:

$$J_b(\mathbf{x}) = \delta\mathbf{x}^T\mathbf{B}^{-1}\delta\mathbf{x} \tag{2.38}$$

The so called control vector space of the ALADIN model is defined as $\chi = L\delta\mathbf{x}$ with L such that:

$$J_b(\chi) = \chi^T\chi \tag{2.39}$$

which implies that $L = \mathbf{B}^{-1/2}$ or $L^TL = \mathbf{B}^{-1}$. The operator L and L^{-1} are applied as a sequence of matrix multiplications:

$$L = \mathcal{H}FHV \qquad L^{-1} = \mathcal{H}^{-1}F^{-1}H^{-1}V^{-1} \tag{2.40}$$

each of the matrices being responsible for a specific step for satisfying the background constraint, that is for filtering and propagating the innovations into analysis increments on the model grid:

- $\mathcal{H}$: apply the horizontal balance through the normalization by the horizontal balance coefficients (β_{k^*})
- F: apply the filtering step through the normalization by standard deviations (V_{k^*})
- H: apply the horizontal propagation step through normalization by horizontal correlations
- V: apply the vertical and multivariate propagation step through the normalization by multivariate vertical covariances ($\mathbf{M}, \mathbf{N}, \mathbf{P}, \mathbf{Q}, \mathbf{S}$)

The iterative minimization algorithm for the J cost function is applied in the χ control vector space, where J_b becomes as simple as defined by equation (2.39). This design makes possible to avoid the explicit inversion of the matrix $\mathbf{B}$, which significantly reduces the computational cost.

Chapter 3

Background error simulation in a limited area model

Early data assimilation methods used prescribed background error covariance matrices of which the spatial structures were intuitively defined based on knowledge of dynamical meteorology and vague observations about the atmosphere ([18] *Czelnai et al.* (1976), [19] *Daley* (1991)). An advanced approach compared to prescribing explicitly the spatial structure functions of $\mathbf{B}$ is to design appropriate techniques for the simulation of background errors and to compute the covariance matrix of the simulated errors:

$$\mathbf{B} = E[\boldsymbol{\epsilon}_b \boldsymbol{\epsilon}_b^T] \tag{3.1}$$

where E stands for the statistical expectation and $\boldsymbol{\epsilon}_b$ is the simulated background error sample (a vector with a dimension of 10^7) aiming to represent the real background errors:

$$\mathbf{e}_b = \mathbf{x}_b - \mathbf{x}_t \tag{3.2}$$

As $\mathbf{x}_t$ is never known, it is a fundamental aspect and an obvious difficulty in background error modeling, to design a good $\boldsymbol{\epsilon}_b$ sample, which represents well the real background errors $\mathbf{e}_b$. This area of data assimilation is often called error simulation or sampling and it has been developed continuously since the 1980's.

In this chapter a proposal is given to simulate background errors in a LAM framework. As described in section 2.3, background errors generally can be understood as the sum of propagated analysis errors and model errors (equation (2.21)). Both of these uncertainties will be accounted for in the proposed simulation techniques, moreover it is shown that besides these two general uncertainties a third one appears in case of a limited area model, namely the uncertainty of the lateral boundary coupling (which enables information exchange between the limited area and its surrounding).

To help the reader to orientate in the subject, first an overview of the most used past and present

background error simulation techniques is given, including the corresponding mathematical formulation. The overview is followed by the description and diagnosis of the error simulation techniques proposed for the LAM case. Analysis, lateral boundary and model uncertainties are accounted for in this order. Also an extension of the general formulation is proposed for the background error simulation, given the LAM framework.

3.1 Overview and general formulation of background error simulation techniques

The first widely used error simulation technique was introduced by Hollingsworth and Lönnberg ([36] *Hollingsworth and Lönnberg* 1986; [48] *Lönnberg and Hollingsworth* 1986) and is often referred to as the "innovation method". As the name also suggests, the innovation method estimates the sum of the observation and background errors with the innovations ($\boldsymbol{\epsilon}_b + \boldsymbol{\epsilon}_o \approx \mathbf{y} - H\mathbf{x}_b$) and consequently the background and observation error covariance matrices by the covariance of the innovations:

$$\mathbf{HBH}^T + \mathbf{R} = E((\mathbf{y} - H\mathbf{x}_b)(\mathbf{y} - H\mathbf{x}_b)^T) \tag{3.3}$$

A known weakness of the innovation method is that the errors are simulated in the observation space, that is, the represented covariance length-scales are determined by the horizontal density of the observing network. This feature becomes problematic once the resolution of the model goes under 100 km (the average resolution of the radiosonde network) and becomes crucial in nowadays high resolution meso scale models (10 - 1 km resolution). Another difficulty in the practical application of the innovation method is to separate the background and observation error variances (see [36] *Hollingsworth and Lönnberg* 1986; [48] *Lönnberg and Hollingsworth* 1986 or [19] *Daley* 1991).

The NMC [1] method was proposed by [51] *Parrish and Derber* (1992). The assumption of this method is that background errors are proportional to differences of model forecasts, which started from different initial conditions and are valid at the same time:

$$\boldsymbol{\epsilon}_b = \mathbf{x}_{b,1} - \mathbf{x}_{b,2} = M\mathbf{x}_{a,1} - M\mathbf{x}_{a,2} \tag{3.4}$$

where M denotes the operator of the forecast model, which propagates the $\mathbf{x}_{a,1}$ and $\mathbf{x}_{a,2}$ initial conditions in time, to end up in the $\mathbf{x}_{b,1}$ and $\mathbf{x}_{b,2}$ forecasts respectively. The initial conditions for the forecast pairs (i.e. $\mathbf{x}_{a,1}$ and $\mathbf{x}_{a,2}$) are taken from different analyzes of the operational assimilation cycle. This also implies that the lead-times of the two forecasts in play are different. For instance a typical NMC sample of the 00 UTC background error for the day D can be written as:

$$\boldsymbol{\epsilon}_b^{(D,00UTC)} = M^{+36h}\mathbf{x}_a^{(D-2,12UTC)} - M^{+12h}\mathbf{x}_a^{(D-1,12UTC)} \tag{3.5}$$

[1] NMC: National Meteorological Center - today's NCEP: National Center for Environmental Prediction

where the first term of the right hand side denotes a 36 hour forecast of the model M started from the 12 UTC analysis of the day $D-2$ and the second term denotes a 12 hour forecast of the same model started from the 12 UTC analysis of the day $D-1$. A clear advantage of the NMC method over the innovation method is that the simulated errors are provided in the model space, which enables the representation of all spatial scales described by the forecast model. However, a weakness of the method is that the NMC forecast differences are not expected to represent the error growth in the background forecast exactly, but they are only supposed to be proportional to it. Namely, the NMC method might exaggerate the analysis uncertainty (i.e. the difference in the initial conditions $\mathbf{x}_a^{(D-2,12UTC)}$ and $\mathbf{x}_a^{(D-1,12UTC)}$) as it is cumulated through 4 consecutive analyzes and background forecasts in case of a 6-hourly assimilation cycle. The overestimated analysis uncertainty is then supposed to lead to overestimated background uncertainties too. Moreover, the time propagation of the analysis uncertainty into background uncertainty itself is furthermore overestimated given the fact that it is realized via forecasts of 12 hour lead-time, instead of 6 hour lead-times, which corresponds to the real background forecasts. All this implies that background error statistics based on NMC samples may overestimate real background errors. This problem is usually solved by reducing the background error variances in an "a posteriori" manner ([60] *Talagrand* 1998, [23] *Désroziers and Ivanov* 2001, [16] *Chapnik et al.* 2004, [56] *Sadiki and Fischer* 2005, [26] *Fischer et al.* 2005, [22] *Désroziers et al.* 2006). More on the application of "a posteriori" diagnosis and tuning can be read in see chapter 5.

Ensemble methods are similar to the NMC method in the sense that background errors are simulated as forecast differences, i.e. all the spatial scales of the model are accounted for. On the other hand, in the Ensemble methods, analysis uncertainties are provided by ensembles of analyzes valid at the same time. These analysis ensembles are generated by a set of direct perturbations accounting for the representation of the analysis uncertainty in the assimilation system. It is obvious that analysis perturbations then imply perturbations in the background forecasts too, which represent the growth of the analysis error in the background forecast, i.e. the background errors. Of course a lot depends on how the analyzes are perturbed in the ensemble. Several techniques exist to generate analysis perturbations being the most widely used the Ensemble Data Assimilation (EDA) ([28] *Fisher* 2003, [15] *Buhner* 2005, [3] *Belo Pereira and Berre* 2006) and the Ensemble Transform (ET) ([4] *Bishop et al.* 2001). Although at OMSZ, experiments have been done with the ET method as well ([1] *Adamcsek et.al* 2010), the thesis focuses on the EDA technique, where the analysis perturbations are implied by an explicit perturbation of observations and an implicit perturbation of the background. Namely, input observations are randomly perturbed with a Gaussian distribution with a zero mean and with a standard deviation equal to the estimated observation error standard deviation. These perturbations are projected to the analysis through the assimilation scheme and then to the background through the model forecast. For the ensemble members k and l, this can be formulated with the following

equation:

$$\begin{aligned}
\boldsymbol{\epsilon}_b^{(i)} &= \mathbf{x}_{b,k}^{(i)} - \mathbf{x}_{b,l}^{(i)} && (3.6)\\
&= M\mathbf{x}_{a,k}^{(i-1)} - M\mathbf{x}_{a,l}^{(i-1)} && (3.7)\\
&= M(\mathbf{x}_{b,k}^{(i-1)} + \mathbf{K}(\mathbf{y}_k^{(i-1)} - H\mathbf{x}_{b,k}^{(i-1)}) && (3.8)\\
&- M(\mathbf{x}_{b,l}^{(i-1)} + \mathbf{K}(\mathbf{y}_l^{(i-1)} - H\mathbf{x}_{b,l}^{(i-1)}) && (3.9)
\end{aligned}$$

where the index i stands for the sequence of assimilation steps in the cycling. The analyzes $\mathbf{x}_{a,k}, \mathbf{x}_{a,l}$ are expressed according to the (2.9) analysis equation, showing well the dependence on the $\mathbf{y}_k^{(i-1)}, \mathbf{y}_l^{(i-1)}$ perturbed observation sets, on the $\mathbf{x}_{b,k}^{(i-1)}, \mathbf{x}_{b,l}^{(i-1)}$ perturbed background states and on the $\mathbf{K}$ Kalman gain, i.e. on the assimilation system. Note that the analysis uncertainty is introduced in a more realistic way compared to the NMC method, given the fact that no multiple consecutive analyzes and background forecasts are involved in the initial differences. Also the error growth in the background forecast is sampled from forecasts of correct lead-times (i.e. the same lead-times as has the background forecast itself). A detailed and comprehensive comparison of the NMC and EDA methods is given by [12] *Berre et al.* (2006) both formally and through an extensive diagnostic study.

In a linear framework, which is mostly valid for small initial perturbations and short range background forecasts, the equation (3.9) can be rewritten as:

$$\begin{aligned}
\boldsymbol{\epsilon}_b^{(i)} &= M\mathbf{x}_{a,k}^{(i-1)} - M\mathbf{x}_{a,l}^{(i-1)} && (3.10)\\
&= M(\mathbf{x}_{a,k}^{(i-1)} - \mathbf{x}_{a,l}^{(i-1)}) && (3.11)\\
&= M\boldsymbol{\epsilon}_a^{(i-1)} && (3.12)\\
&= M(\boldsymbol{\epsilon}_b^{(i-1)} + \mathbf{K}(\boldsymbol{\epsilon}_o^{(i-1)} - H\boldsymbol{\epsilon}_b^{(i-1)})) && (3.13)
\end{aligned}$$

with $\boldsymbol{\epsilon}_o^{(i-1)} = \mathbf{y}_k^{(i-1)} - \mathbf{y}_l^{(i-1)}$ being the simulated observation error, that is, the difference between two perturbed observation sets. Equation (3.13) shows that the form of the (2.9) analysis equation also applies to the simulated errors just like to the model state itself (see [12] *Berre et al.* 2006 for instance). It also reflects how the background error is reduced in the analysis step to an analysis error (at $t = i - 1$), and how this analysis error is evolved in time into a simulated background error again (at $t = i$).

It is important to see, that compared to the general formulation of background errors (described in section 2.3), the above sampling techniques lack the explicit simulation of the $\mathbf{e}_M$ model error. It is the most conspicuous when recalling the formulation of the EDA technique:

$$\mathbf{e}_b^{(i)} \approx \boldsymbol{\epsilon}_b^{(i)} \approx M\boldsymbol{\epsilon}_a^{(i-1)} \approx M\mathbf{x}_{a,k}^{(i-1)} - M\mathbf{x}_{a,l}^{(i-1)} \qquad (3.14)$$

Expressing differently, the above simulation can be seen as a perfect model framework where only the analysis uncertainty $\mathbf{e}_a$ and its evolution to background uncertainty ($\mathbf{e}_b$) is accounted for by taking the difference of two model forecasts started from slightly different initial conditions. The point to be

considered is that the two model forecasts are generated by the same model M, which means that their difference solely comes from the initial differences. A rather new area of forecast error simulation tackles the estimation of model error ([40] *Houtekamer et al.* 2009, [46] *Li et al.* 2009, [63] *Zupanski and Zupanski* 2006). Note that the presented thesis also includes a simulation of the LAM model error in section 3.4 and for its representation in the LAM background error estimation.

3.2 Simulation of background errors using the Ensemble Data Assimilation technique in a limited area model

Given the fact that LAM models need lateral boundary forcing, a new source of uncertainty contributes to the background errors, representing the error of lateral boundary coupling. This is shown hereafter within the EDA formulation applied for a LAM. After introducing the formulation, the simulation of analysis and lateral boundary uncertainties using an ALADIN LAM EDA system are presented within a perfect model framework (neglecting model error). More exactly, besides the lateral boundary uncertainty, two different techniques for the simulation of analysis uncertainty are compared.

3.2.1 Formulation of the Ensemble Data Assimilation technique in a LAM framework

The EDA error simulation technique discussed in the previous section was first developed in a global model framework. In a global model the background forecast is provided purely by the time propagation of the initial conditions given the forecast model:

$$\mathbf{x}_b^{G(i)} = M^G \mathbf{x}_a^{G(i-1)} \tag{3.15}$$

where the superscript ^{G} stands for the global model and state vector. In the LAM case, beside the initial conditions also lateral boundary conditions (LBC) are essential to provide the time propagation of the initial state, as explained in section 2.4.1. Let us assume that the background forecast of the LAM, which is coupled to the global system above, can be decomposed to two components as follows:

$$\mathbf{x}_b^{L(i)} = M^L \mathbf{x}_a^{L(i-1)} \tag{3.16}$$

$$= M^I \mathbf{x}_a^{L(i-1)} + \mathcal{CP} M^G \mathbf{x}_a^{G(i-1)} \tag{3.17}$$

where the superscript ^{L} stands for the LAM state and model operators. The operator M^I ($M^I \subset M^L$) denotes the LAM model operator without lateral boundary forcing (i.e. M^L with constant zero LBCs). Thus, the term $M^I \mathbf{x}_a^{L(i-1)}$ corresponds to the time propagation of the LAM initial conditions without

the effect of LBCs and the term $\mathcal{CP}M^G\mathbf{x}_a^{G(i-1)}$ corresponds to the contribution of the LBCs to the LAM background forecast. The operator $\mathcal{P}$ represents the interpolation of the global background forecast $M^G\mathbf{x}_a^{G(i-1)}$ to the LAM grid and $\mathcal{C}$ stands for the coupling operator, which determines the weight of the LBC contribution. Note, that the formula (3.17) is highly simplified and it does not represent the mechanism of lateral boundary coupling in the real LAM forecast. It is rather used here to interpret the final contribution of the driving global model to the LAM at the end of the background forecast through the LBCs. Based on the above assumption, the EDA background error simulation in case of a LAM can be written as:

$$\boldsymbol{\epsilon}_b^{L(i)} = (M^I\mathbf{x}_{a,k}^{L(i-1)} + \mathcal{CP}M^G\mathbf{x}_{a,k}^{G(i-1)}) - (M^I\mathbf{x}_{a,l}^{L(i-1)} + \mathcal{CP}M^G\mathbf{x}_{a,l}^{G(i-1)}) \tag{3.18}$$

$$= (M^I\mathbf{x}_{a,k}^{L(i-1)} - M^I\mathbf{x}_{a,l}^{L(i-1)}) + (\mathcal{CP}M^G\mathbf{x}_{a,k}^{G(i-1)} - \mathcal{CP}M^G\mathbf{x}_{a,l}^{G(i-1)}) \tag{3.19}$$

$$= M^I(\mathbf{x}_{a,k}^{L(i-1)} - \mathbf{x}_{a,l}^{L(i-1)}) + \mathcal{CP}M^G(\mathbf{x}_{a,k}^{G(i-1)} - \mathbf{x}_{a,l}^{G(i-1)}) \tag{3.20}$$

$$= M^I\boldsymbol{\epsilon}_a^{L(i-1)} + \mathcal{CP}M^G\boldsymbol{\epsilon}_a^{G(i-1)} \tag{3.21}$$

where k and l are two arbitrary members of both the global and LAM systems. The first term on the right hand side represents the LAM background error due to the LAM analysis uncertainty grown by the LAM forecast model without the effect of LBCs. The second term on the right hand side represents the LAM background error due to the uncertainties in the LBCs purely, which can be further decomposed to the background uncertainty of the global model ($M^G\boldsymbol{\epsilon}_a^{G(i-1)}$) and to the error of the LBC coupling procedure incorporated in the LAM ($\mathcal{CP}$). Based on equation (3.21), when designing an EDA system for the simulation of LAM background errors, one has to account both for the LAM analysis uncertainty and for the LBC uncertainty.

The LBC uncertainty $\mathcal{CP}M^G\boldsymbol{\epsilon}_a^{G(i-1)}$ is naturally given if using a global EDA system to drive the LAM members. In the experiments described in this section, the LAM members were driven by an experimental global EDA of the ECMWF/IFS[2] system. The global EDA was run for a month period (1-31/07/2007), with 20 members of 4DVAR assimilation cycles, using a 12-hour assimilation window, on $\Delta x \approx 50$ km horizontal resolution ([41] *Isaksen et al.* 2007). Note, that based on equation (3.13) the LBC uncertainty can be written as:

$$\mathcal{CP}M^G\boldsymbol{\epsilon}_a^{G(i-1)} = \mathcal{CP}M^G(\boldsymbol{\epsilon}_b^{G(i-1)} + \mathbf{K}^G(\boldsymbol{\epsilon}_o^{G(i-1)} - H\boldsymbol{\epsilon}_b^{G(i-1)})) \tag{3.22}$$

which reflects that an important part of the LBC uncertainty originates from the uncertainty of the global analysis system $\mathbf{K}^G$, through the $\boldsymbol{\epsilon}_o^{G(i-1)}$ observations errors and the $\boldsymbol{\epsilon}_b^{G(i-1)}$ background errors involved in the global assimilation cycle.

For the representation of the LAM analysis uncertainty $M^I\boldsymbol{\epsilon}_a^{L(i-1)}$, two solutions of different complexity were considered. These two solutions were tested in two LAM error simulation experiments both consisting of 5 member ensembles, resulting in 4 forecast differences (i.e. simulated error

[2]European Center For Medium-range Weather Forecasting/Integrated Forecasting System

samples) for each analysis time. The 5 LAM members were driven by 5 randomly chosen members of the global EDA system over the same period of one month. The two LAM error simulation experiments are described and evaluated in the following sections.

3.2.2 Downscaling the global analysis uncertainty with the limited area model

A simple, and widely used way to represent LAM analysis uncertainty is to interpolate the perturbed analyzes of the global EDA system to the LAM grid. In this case, the term representing the background error due the LAM analysis uncertainty (first term on the right hand side in equation (3.21)) can be approximated as follows:

$$
\begin{aligned}
M^I \boldsymbol{\epsilon}_a^{L(i-1)} &\approx M^I \mathcal{P} \mathbf{x}_{a,k}^{G(i-1)} - M^I \mathcal{P} \mathbf{x}_{a,l}^{G(i-1)} && (3.23)\\
&= M^I \mathcal{P} (\mathbf{x}_{b,k}^{G(i-1)} + \mathbf{K}^G (\mathbf{y}_k^{G(i-1)} - H \mathbf{x}_{b,k}^{G(i-1)})) && (3.24)\\
&- M^I \mathcal{P} (\mathbf{x}_{b,l}^{G(i-1)} + \mathbf{K}^G (\mathbf{y}_l^{G(i-1)} - H \mathbf{x}_{b,l}^{G(i-1)})) && (3.25)\\
&= M^I \mathcal{P} (\boldsymbol{\epsilon}_b^{G(i-1)} + \mathbf{K}^G (\boldsymbol{\epsilon}_o^{G(i-1)} - H \boldsymbol{\epsilon}_b^{G(i-1)})) && (3.26)
\end{aligned}
$$

where the indices k and l stand for two arbitrary perturbed members of the global EDA system. As indicated by the above equation, in this error simulation technique, the analysis uncertainty originates mainly from the uncertainty of the global analysis system ($\boldsymbol{\epsilon}_b^{G(i-1)}, \boldsymbol{\epsilon}_o^{G(i-1)}, \mathbf{K}^G$) just like the LBC uncertainties, as described in the previous section. As a consequence, this error simulation technique is considered and referred as a downscaling of the global analysis uncertainty via the interpolation $\mathcal{P}$ and the model operator M^I. LAM experiments given the above formula have been discussed in [12] *Berre et al.* (2006), [58] *Stefanescu et al.* (2006) and [8] *Bölöni* (2006).

3.2.3 Simulation of analysis uncertainties in the limited area model itself

A more advanced way to represent LAM analysis uncertainty is to generate EDA perturbations in the LAM system itself:

$$
\begin{aligned}
M^I \boldsymbol{\epsilon}_a^{L(i-1)} &= M^I \mathbf{x}_{a,k}^{L(i-1)} - M^I \mathbf{x}_{a,l}^{L(i-1)} && (3.27)\\
&= M^I (\mathbf{x}_{b,k}^{L(i-1)} + \mathbf{K}^L (\mathbf{y}_k^{L(i-1)} - H \mathbf{x}_{b,k}^{L(i-1)})) && (3.28)\\
&- M^I (\mathbf{x}_{b,l}^{L(i-1)} + \mathbf{K}^L (\mathbf{y}_l^{L(i-1)} - H \mathbf{x}_{b,l}^{L(i-1)})) && (3.29)\\
&= M^I (\boldsymbol{\epsilon}_b^{L(i-1)} + \mathbf{K}^L (\boldsymbol{\epsilon}_o^{L(i-1)} - H \boldsymbol{\epsilon}_b^{L(i-1)})) && (3.30)
\end{aligned}
$$

where the indices k and l stand for two arbitrary members of the **LAM EDA** system. The above equation shows that in the **LAM EDA** error simulation technique the analysis uncertainty originates indeed from the LAM analysis system $\mathbf{K}^L$, through the $\boldsymbol{\epsilon}_o^{L(i-1)}$ observations errors and the $\boldsymbol{\epsilon}_b^{L(i-1)}$ background errors present in the LAM assimilation system. This implies that an ensemble of data

assimilation cycles is required to run in the LAM itself including an explicit perturbation of the used observations. To precise the actual realization of the **LAM EDA** experiment, it might be important to mention that one of the members (any of k or l) involved in the forecast differences was chosen to be the unperturbed (control) member (i.e. an assimilation cycle fed by the unperturbed observations). This was done in order to avoid the overestimation (doubling) of the simulated error variance, which comes into play if the difference of two perturbed members are used to simulate the analysis and background errors ([28] *Fisher* 2003, [12] *Berre et al.* 2006). Another important detail about the **LAM EDA** experiment is that all the observations used operationally in the ALADIN/HU model were perturbed. These observations include surface, radiosonde, aircraft and satellite measurements, for several meteorological variables (see Table 3.1). It is also to be mentioned that through the perturbation of surface observations, also the perturbation of the soil temperature and moisture analyzes was implied. Similar experiments to **LAM EDA** have been performed by [59] *Storto and Randriamampianina* (2010) and [50] *Monteiro and Berre* (2010).

Observation type	**Variable**
Surface SYNOP	temperature, relative humidity, geopotential
Surface SHIP	temperature, relative humidity, geopotential, wind
Radiosonde	temperature, specific humidity, geopotential, wind
Aircraft AMDAR	temperature, wind
Wind profiler	wind
Satellite MSG/GEOWIND	wind
Satellite MSG/SEVIRI	radiance
Satellite NOAA/ATOVS/AMSU-A,B,MHS	radiance
Satellite METOP/ATOVS/AMSU-A,MHS	radiance

Table 3.1: Observations used in the operational in ALADIN/HU data assimilation system (3DVAR for the atmospheric and OI for the soil variables). The same observations have been perturbed in the **LAM EDA** experiment.

3.2.4 Diagnostic comparison of different analysis uncertainty representations

As described above, the **DSC EDA** error simulation technique is much simpler compared to the **LAM EDA** technique, both conceptually and from the point of view of technical implementation. The simplicity of **DSC EDA** is given the fact that there is no need for running local data assimilation and its perturbations in the LAM itself. Thus, the application of **DSC EDA** technique means a save of resources. On the other hand, as shown before, the weakness of this approach is that the simulated LAM analysis uncertainty originate from the global analysis uncertainty (see equation (3.26)). The global analysis, and the error simulation based on its perturbation do not include detailed information

on the meso scale analysis error relevant for the LAM, due to the lower spatial resolution of the global EDA system both in terms of grid distance (global EDA: $\Delta x \approx 50$ km, ALADIN/HU: $\Delta x \approx 8$ km) and the input observing network. On the contrary, the application of the **LAM EDA** technique is somewhat more resource consuming, but on return, it will lead to the representation of the actual analysis uncertainty of the LAM itself corresponding to its nominal resolution both in terms of grid distance and input observations.

The importance of the observing network's spatial resolution can be demonstrated by comparing the input observations in case of a global model (ARPEGE) and the ALADIN/HU LAM (Fig.3.1). According to the figure the perturbation of the two observing networks might lead to very different spatial structures in the analysis perturbations, namely including more meso scale structures if the high resolution network of ALADIN/HU is used.

The importance of the model resolution can be demonstrated, for instance, by plotting the

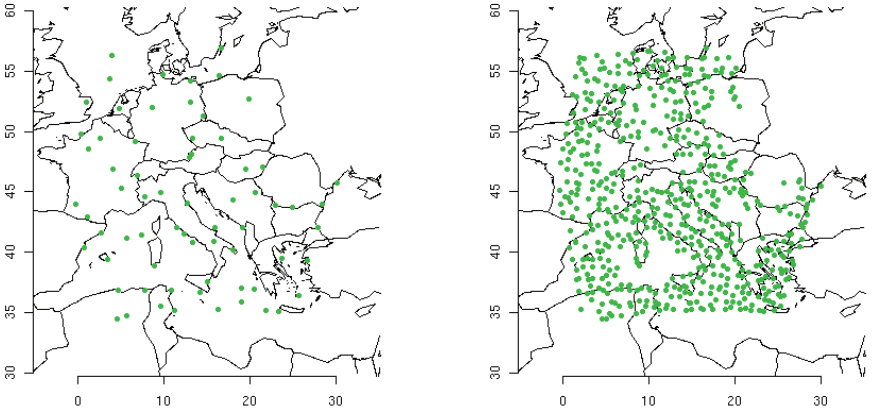

Figure 3.1: An example of NOAA-18 ATOVS/MHS satellite data data density assimilated observations in the ARPEGE global model (left) and in the ALADIN LAM (right) at an arbitrary chosen date (06 UTC on the 16/11/2009). The average distance between radiance pixels was ≈ 280 km in the ARPEGE global model and ≈ 80 km in the ALADIN/HU model at this analysis time.

wind energy spectra of the LAM analysis and the global analysis interpolated to the LAM grid. The low and wavy energy pattern in Fig.3.2 shows, that the $\mathcal{P}\mathbf{x}_a^G$ interpolated global analysis does not hold physical information below a certain resolution (above wavenumber 40 of the LAM), but rather noise, which is due to the interpolation. On the contrary, the wind energy in the $\mathbf{x}_a^L$ LAM analysis is relatively high and its distribution is realistic. It is to be mentioned here, that a digital filtering

([49] *Lynch and Huang* 1992) might be performed after applying the $\mathcal{P}$ interpolation on the $\mathbf{x}_a^G$ global analysis, in order to smooth the interpolation noise. As shown on Fig.3.2, the wind energy after the filtering becomes much less noisy on the small scales, however it is still somewhat lower than that of the LAM analysis. It is important to notice that in spite of the successful removal of the noise, the small scale spectrum introduced by the filtering is mostly mathematical, thus not much corresponding to the information contained in the high resolution observations assimilated in the LAM.

All these considerations suggest that the **LAM EDA** technique might simulate the analysis uncertainties in a more realistic way than the **DSC EDA** technique. Whether this intuition is true, it will be studied through diagnostics in this section. All the diagnostics were computed on simulated errors valid at 12 UTC of each day during the above-mentioned test period.

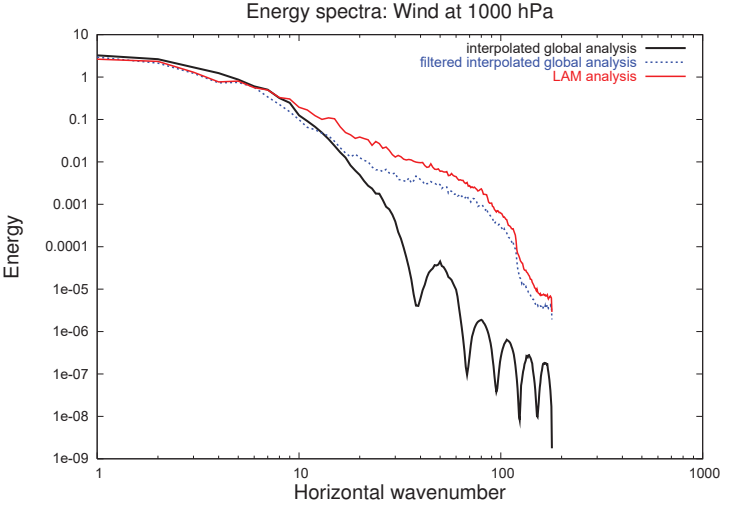

Figure 3.2: Wind energy spectra ($kg\ m^2 s^{-2}$) at 1000 hPa for the $\mathbf{x}_a^L$ LAM analysis (red), for the $\mathcal{P}\mathbf{x}_a^G$ interpolated global analysis (black) and for the latter after digital filtering (blue).

Spectral variances

The spectral variance of background errors is computed as defined by equation (2.32), but for a single variable. This spectral diagnostic is the function of the k_* total wavenumber, which, as explained in section 2.4, is in correspondence with the horizontal scales in physical space (i.e. small wavenumbers correspond to large scales and large wavenumbers correspond to small scales). As a consequence, the spectral variance holds information about horizontal correlations in physical space. For instance large spectral variance for large (small) wavenumbers stands for large correlations for large (short)

distances.

In Fig.3.3 and 3.4, the spectral error variances of the four main analysis variables (vorticity, divergence, temperature and specific humidity) are plotted for the experiments **DSC EDA** and **LAM EDA** at 500 and 850 hPa respectively. In the free atmosphere (at 500 hPa), the background error variance obtained with the **LAM EDA** technique is increased on a large range of spatial scales (from wavenumber 4 to 100, i.e. from 500 to 30 km) compared to those obtained with the **DSC EDA** technique. The increased variance by **LAM EDA** shows that the explicit perturbation of the LAM analysis system (through the perturbation of the corresponding observations) introduces additional uncertainty to the simulated background errors. In the planetary boundary layer (PBL) (at 850 hPa) an increase of variance by **LAM EDA** in the same range of scales can be observed but in a smaller extent. Although, on the very large scales (below wavenumber 4) a decrease of variance is also implied by **LAM EDA** compared to **DSC EDA**. The reason might be due to the differences between the setup of the global ECMWF/IFS and the ALADIN/HU EDA systems. One of the possible differences can be that the global EDA contains some observation components that are not directly used in **LAM EDA** (e.g. GPS, scatterometers and certain satellite observations). Then, the lack of perturbations for such observation sets missing from **LAM EDA** might cause a decrease of variance too. Another potential decrease of variance can come from the fact that the global EDA system was perturbed by a spectral backscattering scheme on the top of the random perturbation of observations ([41] *Isaksen et al.* 2007). These perturbations might penetrate to both LAM error simulation experiments through the LBCs, but only to **DSC EDA** through the initial conditions. It might have been happened thus, that the large scale initial perturbations in the global EDA and in **DSC EDA**, which were caused by the combination of the perturbation of observations and the spectral backscattering scheme, were somewhat decreased in **LAM EDA**, where only the observations were perturbed. Another interesting aspect of the spectral variances is that the maximum variance is somewhat shifted towards the small scales in **LAM EDA** compared to **DSC EDA** for most of the variables. This implies that the small scales of the background forecast will be penalized more in the variational assimilation if the **LAM EDA** simulation technique is used, which also means that the small scale information subtracted from the observations will have a larger contribution to the analysis. It is hard to judge whether this property of the **LAM EDA** simulation technique is advantageous or not for short range forecasting but other diagnostics will be of great help in sorting it out.

Standard deviation

Background error standard deviations for a given vertical level were computed as follows:

$$\sigma(l) = \sqrt{\sum_{k_*=0}^{N} V_{k^*}(l)} \tag{3.31}$$

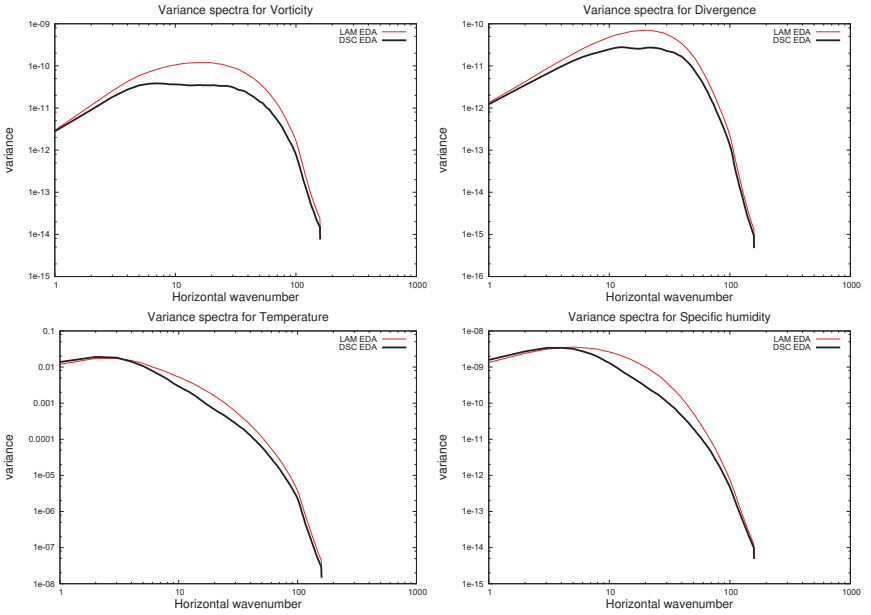

Figure 3.3: Spectral variance computed based on experiments **DSC EDA** (black) and **LAM EDA** (red) at model level 22 ($\approx$ 500 hPa). Top left: vorticity (s^{-2}), Top right: divergence (s^{-2}), Bottom left: temperature (K^2), Bottom right: specific humidity ($g^2\ kg^{-2}$)

where l stands for the model level and V_{k^*} denotes the spectral variance defined in section 2.4.2. Vertical profiles of such standard deviations are plotted in Fig.3.5. Generally, standard deviations deduced from **LAM EDA** are larger than those computed from **DSC EDA**, although an exception is temperature around model level 36 ($\approx$850 hPa) and specific humidity on low levels. Increased **LAM EDA** standard deviations compared to **DSC EDA** match well the intuition that local analysis perturbations might increase the background uncertainty. Decreased standard deviations of **LAM EDA** may be explained similarly as decreased variances in the previous section. It is also interesting to plot the standard deviation in the function of both the horizontal scale (total wavenumber k_*) and the height. Such plot can be seen in Fig.3.6 for divergence on level 22 ($\approx$ 500 hPa). A maximum of standard deviation can be seen in the low troposphere for both experiments, however being stronger and shifted towards smaller scales in the experiment **LAM EDA**. These maximas locate spatial scales and heights in the atmosphere where the prediction of divergent (convergent) systems is the most uncertain. The shift of maxima towards the smaller scales with the **LAM EDA** technique can be interpreted as an ability to represent the error of smaller scale divergent (convergent) systems than with the **DSC EDA** technique.

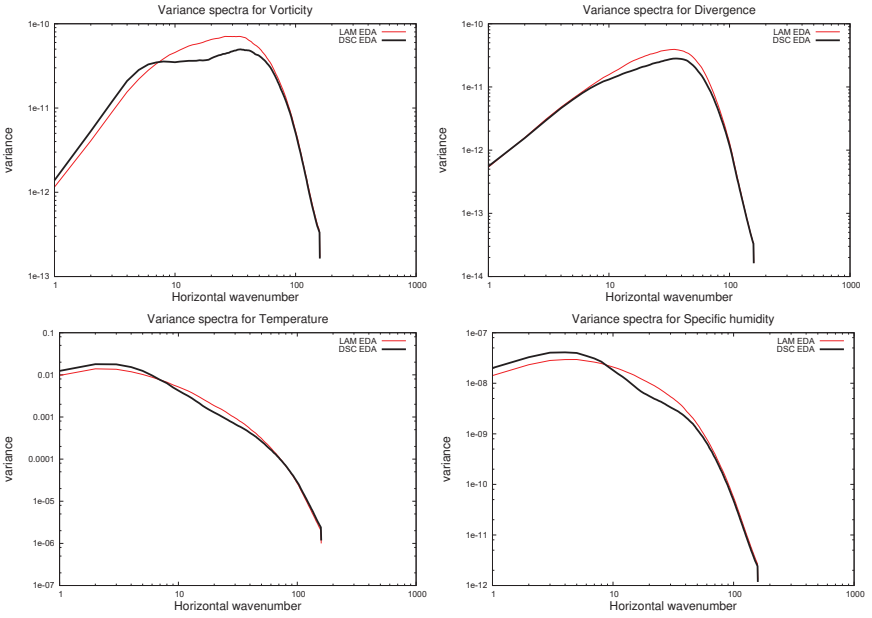

Figure 3.4: Spectral variance computed based on experiments **DSC EDA** (black) and **LAM EDA** (red) at model level 36 ($\approx$ 850 hPa). Top left: vorticity (s^{-2}), Top right: divergence (s^{-2}), Bottom left: temperature (K^2), Bottom right: specific humidity ($g^2\ kg^{-2}$)

Correlation length-scales

Correlation length-scales diagnose the distance on which horizontal background error correlations decay from 1 to 0, or with other words, they show what is the distance on which assimilated observations impact their surrounding. They can be computed in physical space as ([19] *Daley* 1991):

$$\mathcal{L} = \sqrt{-\frac{2\rho}{\Delta\rho}\Big|_0} \tag{3.32}$$

with ρ being the correlation function (decreasing from 1 to 0 away from the origin point). It is shown in [10] *Berre* (2000), that in spectral space the length-scale computation can be written as (for temperature for instance):

$$\mathcal{L} = \frac{N}{2\pi}\sqrt{\frac{2\sum_{m=0}^{M}\sum_{n=0}^{N}\overline{T^z_{m,n}T^{z*}_{m,n}}}{\sum_{m=0}^{M}\sum_{n=0}^{N}k_*^2\overline{T^z_{m,n}T^{z*}_{m,n}}}} \tag{3.33}$$

In Fig.3.7, the correlation length-scales computed for the experiment **DSC EDA** and **LAM EDA** are shown. Generally, correlation length-scales are increasing with height for both experiments. This

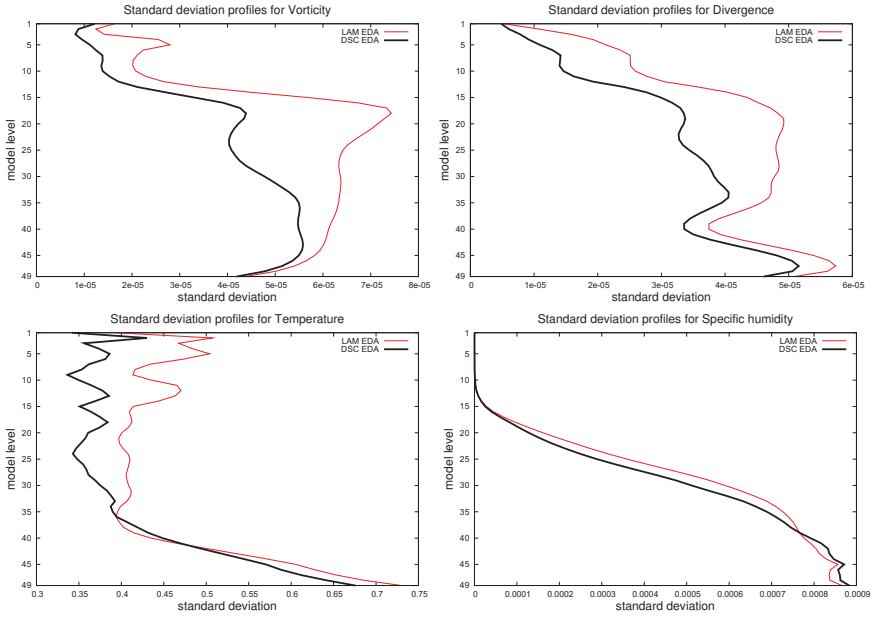

Figure 3.5: Standard deviation profiles deduced from experiment **DSC EDA** (black) and **LAM EDA** (red). Top left: vorticity (s^{-1}), Top right: divergence (s^{-1}), Bottom left: temperature (K), Bottom right: specific humidity ($g\ kg^{-1}$)

is rather sensible, as atmospheric fields become smoother and thus more connected on large scales with an increasing distance from the surface, of which the properties are very much variable in space. Concerning the comparison of the two experiments, temperature and humidity length-scales of the **LAM EDA** technique are shorter than those of **DSC EDA**, divergence length-scales are rather similar in the two experiments, while vorticity length-scales are larger in the lower troposphere and shorter in the upper troposphere in case of **LAM EDA**. The shorter length-scales of **LAM EDA** are probably due to the presence of more small scale structure in the analysis uncertainty through the local analysis perturbations. Larger length-scales of **LAM EDA** for vorticity are not explained yet. It is interesting to notice that length-scales near the surface are the same or very similar between the two experiments. It may reflect an effect of the digital filter, which is the most active near surface and, which may filter out the same shortest scales from **DSC EDA** and **LAM EDA**.

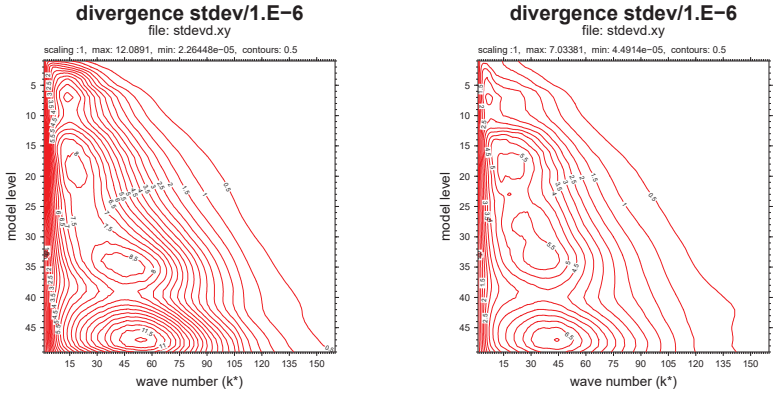

Figure 3.6: Standard deviation of divergence ($s^{-1} * 10^6$) as a function of the vertical level and the horizontal wavenumber, Left: experiment **LAM EDA**, Right: **DSC EDA**

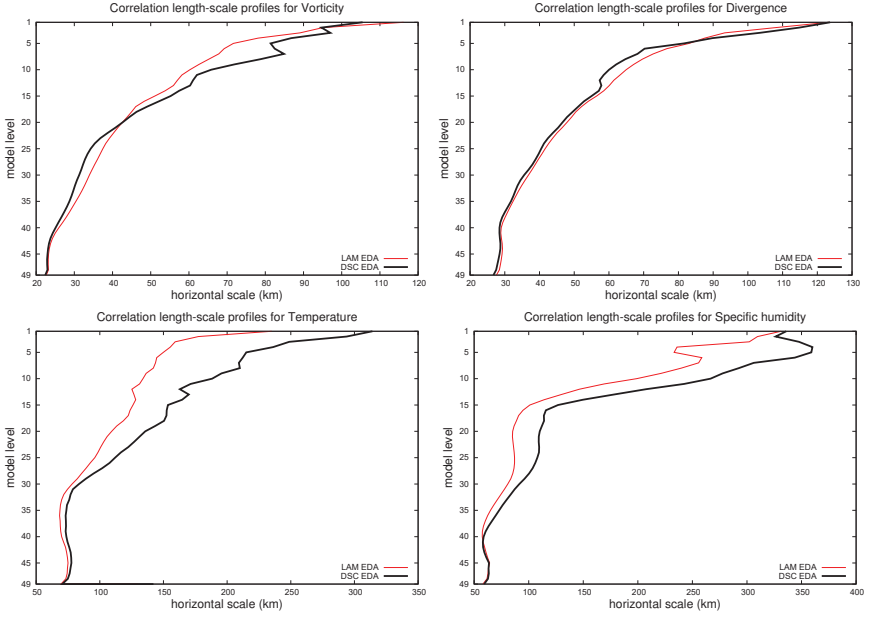

Figure 3.7: Correlation length-scale profiles deduced from the experiments **DSC EDA** and **LAM EDA**. Top left: vorticity, Top right: divergence, Bottom left: temperature, Bottom right: specific humidity.

Spread-skill diagnostics in spectral space

Spread-skill is a well known diagnostic to measure whether the spread of an ensemble prediction system (EPS) is appropriate to capture the forecast error. In an ideal EPS system the spread and the root-mean-square (RMSE) of the forecast error are close to each other, which means that the dispersion in the ensemble members represents well the forecast uncertainty in a statistical sense. If the spread is smaller (larger) than the RMSE, the EPS system is often called as under-dispersive (over-dispersive). In order to account for the ensemble of background forecasts, the spread and the RMSE components of this diagnostic were computed as follows:

$$SPREAD = \sqrt{\frac{1}{T}\sum_{i=1}^{T}(\frac{1}{J}\sum_{j=1}^{J}(x_b^{i,j} - \overline{x_b^i})^2)} \qquad RMSE = \sqrt{\frac{1}{T}\sum_{i=1}^{T}(x_a^{verif,i} - \overline{x_b^i})^2} \quad (3.34)$$

where j is the index for the ensemble members, i is the index for the time realizations, and the over-bar denotes the average over the ensemble members. The notation x_a^{verif} stands for verification analysis, which is meant to represent an atmospheric state close to the truth x_t. In our case, the verification analysis was chosen to be an ALADIN/HU VARPACK diagnostic analysis. This analysis is provided by the 3DVAR minimization of the ALADIN/HU model but with increased background error standard deviations, so that the analysis is close to the observations. Usually the (3.34) diagnostic is computed for a certain grid-point or with a spatial averaging over all the grid-points. However, to get the distribution according to the spatial scales, the spread-skill has been computed in spectral space, i.e. through a similar spectral averaging that has been done for the variances and standard deviations:

$$SPREAD_{k_*} = \sqrt{\frac{1}{T}\sum_{i=1}^{T}(\frac{1}{J}\sum_{j=1}^{J}(\frac{1}{K}\sum_{m,n\leftrightarrow k_*}(x_{bm,n}^{i,j} - \overline{x_{bm,n}^i})^2))} \quad (3.35)$$

$$RMSE_{k_*} = \sqrt{\frac{1}{T}\sum_{i=1}^{T}(\frac{1}{K}\sum_{m,n\leftrightarrow k_*}(x_{am,n}^{verif,i} - \overline{x_{bm,n}^i})^2)} \quad (3.36)$$

The spectral spread-skill will indicate, thus, the ability of the background ensemble (perturbations) to represent background errors of a given spatial scale. Spectral spread and RMSE plots are shown in Fig.3.8 for the experiments **DSC EDA** and **LAM EDA** at 850 hPa (model level 36). It is rather obvious from the figures, that experiment **LAM EDA** outperforms **DSC EDA** especially for the small scales. This comes partly from the increase of the spread, which is probably due to the LAM analysis perturbations. The increase in the spread is more emphasized on the small scales, which proves that **LAM EDA** perturbations have the capability to add small scale information to the representation of initial uncertainty. It is interesting to notice that on the very large scales (under wavenumber 5 or for larger systems than $\approx$ 500 km) there is no additional spread due to the LAM analysis perturbations (except divergence in a small extent). This might be an indication that large scale background uncertainties are mostly determined by LBCs and not very much by the LAM initial perturbations.

Besides the increase of the spread, another improvement by **LAM EDA** lies in decreasing the RMSE. This feature is probably due to the fact that **LAM EDA** initial conditions lead to background forecasts with more realistic spatial details (corresponding better to the verification analyzes x_a^{verif}) than **DSC EDA** initial conditions, which lack physical information in the small scale part of the spectrum (Fig.3.2). This explanation is supported by the fact that the decrease in the RMSE is more characteristic on the small scales. It can be mentioned here that according to this diagnostic, both experiments are under-dispersive on the large scales. On the small scales experiment **LAM EDA** becomes very appropriate, with almost identical spread and RMSE. Spread-skill diagnostics for the other variables (vorticity, temperature and specific humidity) and other levels show rather similar features as observed in Fig.3.8 (not shown). Profiles of spread and RMSE diagnostics averaged over the total wavenumber k_* are shown in Fig.3.9. A clear conclusion based on this figure that horizontally averaged spread-skill diagnostics show a better performance of the **LAM EDA** technique compared to **DSC EDA**. This is again due to both the increase of spread and the decrease of RMSE by **LAM EDA** error simulation, as explained for Fig.3.8. It is also well seen on the profiles that background ensembles from both error simulation techniques are under-dispersive, but **LAM EDA** much smaller extent.

Besides the findings relevant for background error modeling, the comparison of **DSC EDA** and **LAM EDA** simulation techniques also implies important conclusions on short range LAM ensemble prediction (LAM EPS). Namely, the improved spread-skill scores of **LAM EDA** compared to **DSC EDA** proves that short range LAM EPS forecasts including local (LAM) initial perturbations tend to be more successful compared to those consisting of a pure downscaling of global EPS systems, especially on the meso scales.

Perturbation versus Error Amplitude Correlation Analysis (PEACA) in spectral space

Perturbation versus Error Correlation Analysis (PECA) was proposed by [64] *Wei and Tóth* (2003) as a diagnostic to measure EPS performance. Applying its definition to an ensemble of background forecasts one writes:

$$PECA = corr(\boldsymbol{\epsilon}_b, \mathbf{e}_b) \tag{3.37}$$

where $\boldsymbol{\epsilon}_b$ is the simulated background error (for instance by **DSC EDA** or by **LAM EDA**) and $\mathbf{e}_b$ is supposed to be the real background error. PECA scores of global EPS systems (ECMWF and NCEP) were computed by [64] *Wei and Tóth* (2003) for various forecast ranges in grid-point space with a horizontal averaging. One problem with the proposed PECA diagnostic is that the simulated and "real" forecast errors are taken into account with their full sign. This implies that the PECA correlations will not measure the correspondence between simulated and real error amplitudes but mostly it will indicate the systematic errors of the ensemble, given the fact that random errors of opposite sign will cancel each other on a large enough sample. With a slightly modified diagnostic (Perturbation versus

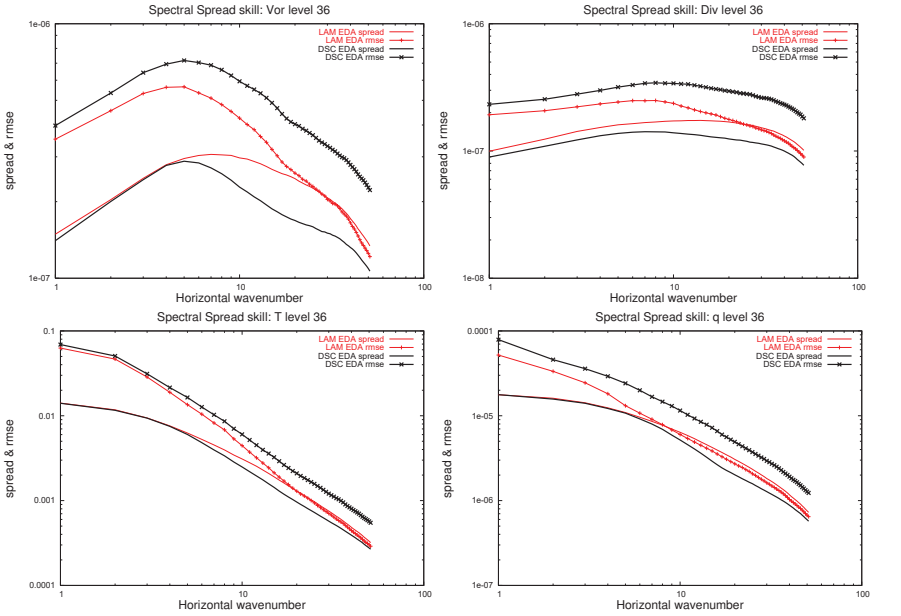

Figure 3.8: Spectral spread-skill score for level 36 (≈ 850 hPa) deduced from the experiments **DSC EDA** and **LAM EDA**. Top left: vorticity (s^{-1}), Top right: divergence (s^{-1}), Bottom left: temperature (K), Bottom right: specific humidity ($g\ kg^{-1}$)

Error Amplitude Correlation Analysis: PEACA) one can account for the correspondence between simulated and real error amplitudes by considering the absolute values of errors:

$$PEACA = corr(|\boldsymbol{\epsilon}_b|, |\mathbf{e}_b|) \tag{3.38}$$

In our case, the $\mathbf{e}_b$ "real" background error was chosen to be as follows:

$$\mathbf{e}_b \approx \mathbf{x}_a^{verif} - \overline{\mathbf{x}_b} \tag{3.39}$$

where the over-bar denotes the average over the ensemble members and $\mathbf{x}_a^{verif}$ is the same VARPACK diagnostic analysis as already introduced in the definition of the spectral spread-skill. To be able to study the distribution according to spatial scales, the PEACA correlations were computed in spectral space (as a function of the total wavenumber k_*). Using the definition of spectral covariances by [10] *Berre* (2000) the spectral PEACA correlation can be written as:

$$PEACA_{k_*} = \frac{\frac{1}{K}\sum_{m,n\leftrightarrow k_*} \overline{|\boldsymbol{\epsilon}_{bm,n}||\mathbf{e}^*_{bm,n}|}}{\sqrt{\frac{1}{K}\sum_{m,n\leftrightarrow k_*} \overline{|\boldsymbol{\epsilon}_{bm,n}||\boldsymbol{\epsilon}^*_{bm,n}|}}\sqrt{\frac{1}{K}\sum_{m,n\leftrightarrow k_*} \overline{|\mathbf{e}_{bm,n}||\mathbf{e}^*_{bm,n}|}}} \tag{3.40}$$

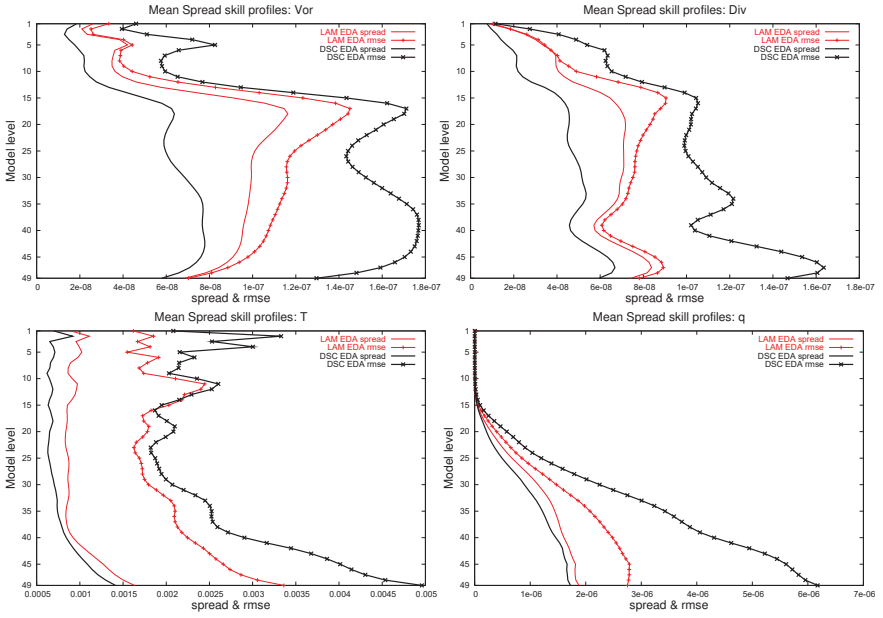

Figure 3.9: Vertical profiles of horizontally averaged spread-skill deduced from the experiments **DSC EDA** and **LAM EDA**. Top left: vorticity (s^{-1}), Top right: divergence (s^{-1}), Bottom left: temperature (K), Bottom right: specific humidity ($g\ kg^{-1}$)

where $\boldsymbol{\epsilon}_{bm,n}$ and $\mathbf{e}_{bm,n}$ are model state differences in spectral space corresponding to the simulated and "real" background errors respectively as defined by the **DSC EDA** and **LAM EDA** error simulation techniques and equation (3.39). Thus, spectral PEACA correlations show the correspondence of simulated and "real" error amplitudes as a function of spatial scales. Such diagnostics are plotted for the **DSC EDA** and **LAM EDA** simulation techniques at $\approx$ 850 hPa (model level 36) in Fig.3.10. An interesting feature is that PEACA for **DSC EDA** tend to decrease, while for **LAM EDA** clearly increase when going from large to small scales. This implies slightly higher PEACA correlations for **DSC EDA** on the large scales and significantly higher PEACA for **LAM EDA** on the small scales. All these findings might prove that the application of direct LAM initial perturbations (**LAM EDA**) improve efficiently the representation of small scale background errors. The slightly lower PEACA values of **LAM EDA** at large scales might be explained similarly as the lower **LAM EDA** variances (lack of the spectral backscattering and possibly some observation components in the ALADIN/HU runs). The wavenumber where the PEACA for **LAM EDA** becomes higher might correspond to the horizontal scale where the LAM initial perturbations become active. Vertical profiles of PEACA correlations are shown in Fig.3.11 averaged over the horizontal scales. These plots show that the

simulated background error amplitudes from experiment **LAM EDA** are matching better "real" background error amplitudes on all vertical levels in terms of horizontal average.

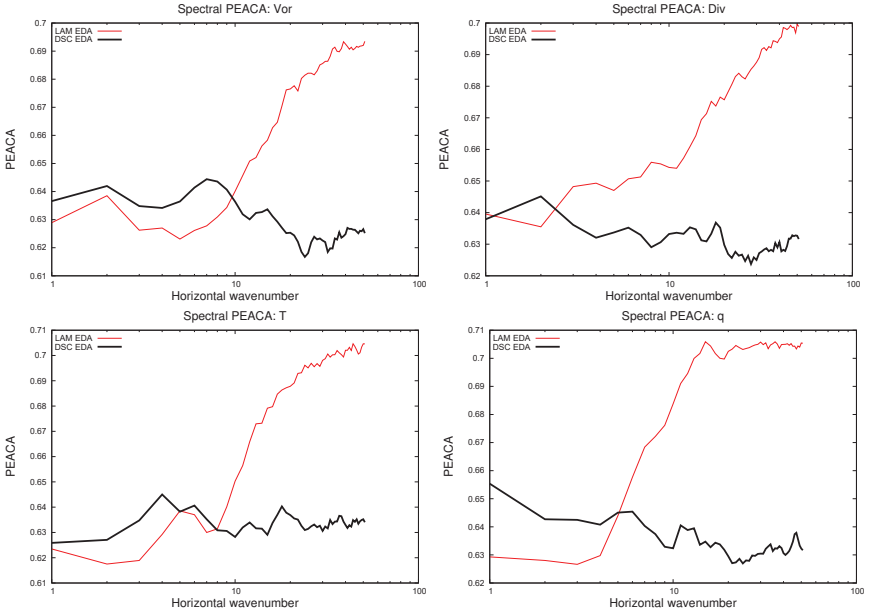

Figure 3.10: PEACA correlation in the function of the logarithm of the wavenumber at level 36 ($\approx$ 850 hPa) deduced from the experiments **DSC EDA** and **LAM EDA**. Top left: vorticity, Top right: divergence, Bottom left: temperature, Bottom right: specific humidity.

Diagnosis of the multivariate aspects

Diagnostics shown so far were concentrating only on the univariate aspects of simulated background errors. It might be however important to see, how the different error simulation techniques act on the multivariate balances included in the background error covariance matrix. To this end, the squared correlation between vorticity and geopotential (implied by the balance operator $\mathcal{H}$) is shown in Fig.3.12, where a lower value for the **LAM EDA** experiment can be found for all horizontal scales. As the balance operator $\mathcal{H}$ represents the geostrophic balance, the lower ratio means that the degree of geostrophy is lower, or with other words less of the geopotential errors (changes) is imposed by vorticity errors (changes). The lower degree of geostrophy using the **LAM EDA** error simulation technique might come from additional meso scale background error structures due to the LAM initial perturbations, which might be less determined by the geostrophic adjustment. Further multivariate

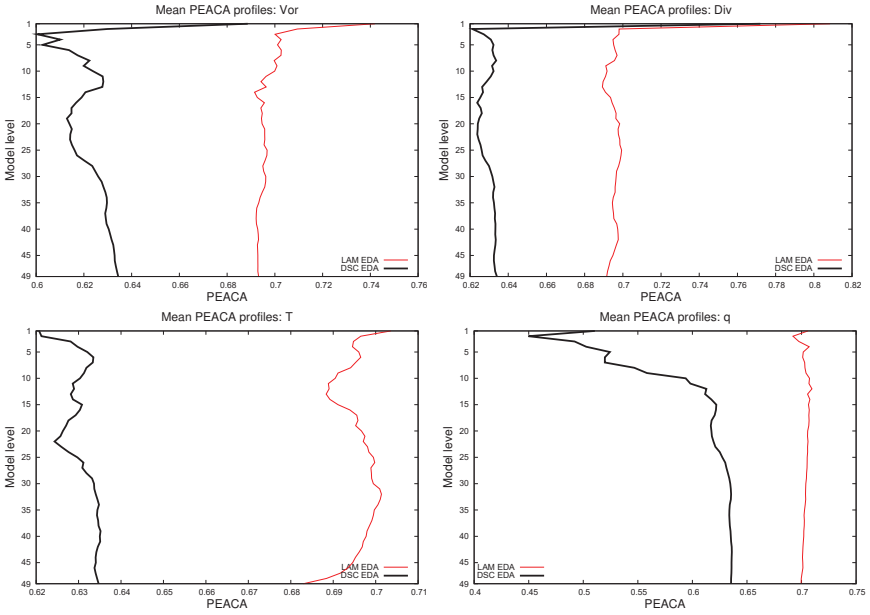

Figure 3.11: Vertical profiles of horizontally averaged PEACA correlations deduced from the experiments **DSC EDA** and **LAM EDA**. Top left: vorticity, Top right: divergence, Bottom left: temperature, Bottom right: specific humidity.

balances are studied through the ratio of explained variance of a given variable by another one (e.g the ratio of total temperature background error variance and that explained by unbalanced divergence):

$$R_{k_*} = \frac{V_{k_*}(T)_{\eta_u}}{V_{k_*}(T)} \tag{3.41}$$

where $V_{k_*}(T)_{\eta_u}$ denotes the temperature error variance explained by unbalanced divergence and $V_{k_*}(T)$ stands for the total background error variance of temperature. The ratios of the explained variance are determined by the balance operators $\mathbf{M}, \mathbf{N}, \mathbf{P}, \mathbf{Q}, \mathbf{R}, \mathbf{S}$ briefly presented in section 2.4. The (horizontally averaged) vertical profiles of explained variance ratios are shown in Fig.3.13 for temperature. The plots indicate that the temperature variance explained by the vorticity-balanced geopotential is clearly larger in case of the **DSC EDA** experiment, while the temperature variance explained by the unbalanced divergence gets higher for the **LAM EDA** experiment near the surface. These findings get an interesting meaning while referring to the physical interpretation of the balance operators relevant to temperature ($\mathbf{N}$ and $\mathbf{P}$ in equation (2.37)), which is given in detail by [53] *Rabier et al.* (1998), [10] *Berre* (2000) or [6] *Bölöni* (2001). Namely, the balance between temperature and vorticity-balanced geopotential (balance operator $\mathbf{N}$) typically concerns synoptic scales, corre-

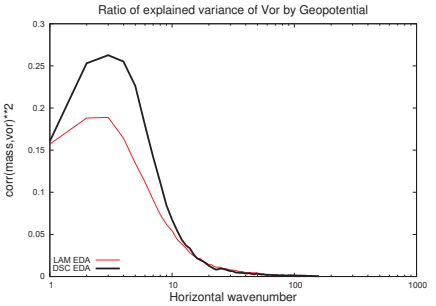

Figure 3.12: Ratio of explained variance of Vorticity by Geopotential

sponding to the temperature errors (changes) induced by mass and wind errors (changes) in cyclonic and anti-cyclonic situations. On the other hand, the balance between temperature and unbalanced divergence (balance operator $\mathbf{P}$) is active mostly on meso scales, corresponding to the temperature errors (changes) induced by convergence (negative divergence) errors (changes) near the surface and by divergence errors (changes) at the top of the PBL, which are implied by convection.

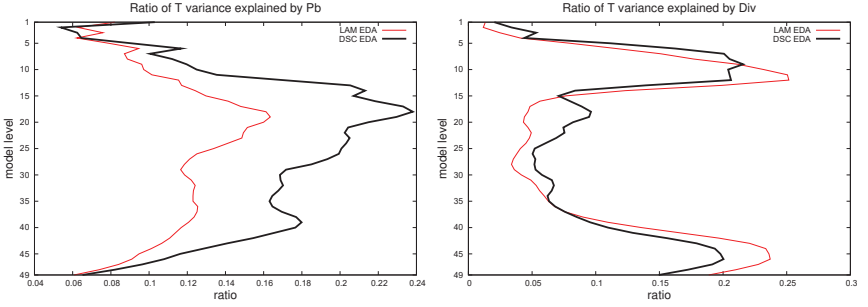

Figure 3.13: Explained variance of temperature by vorticity-balanced geopotential (left) and by unbalanced divergence (right). **DSC EDA**: black, **LAM EDA**: red

In this context, Fig.3.13 shows that the **LAM EDA** error simulation strengthens the meso scale, while it weakens the synoptic scale multivariate balances compared to the **DSC EDA** error simulation, which also proves the presence of additional meso scale information induced by the direct LAM initial perturbations. Similar plots of explained variance ratios for the balances involving specific humidity are shown in Fig.3.14, which are determined by the balance operators $\mathbf{Q}, \mathbf{R}, \mathbf{S}$. Physical interpretations and scale dependence of the humidity balances can be found in [10] *Berre* (2000) or [6] *Bölöni*, 2001. Namely, the balance between humidity and vorticity-balanced geopotential (balance

operator $\mathbf{Q}$) is active on synoptic scales reflecting how large scale low (high) pressure systems moisten (dry) the troposphere by humidity convergence and vertical advection. The balance between humidity and unbalanced divergence (balance operator $\mathbf{R}$) is more relevant for meso scales and it represents the moistening due to convection. Finally, the balance between humidity and unbalanced temperature (balance operator $\mathbf{S}$) corresponds to rather small scale processes of latent heating due to phase changes in clouds. As shown in Fig.3.14, humidity balances relevant for synoptic scales are weakened, while those relevant for meso scales are mostly strengthened by the **LAM EDA** error simulation similarly as in the case of temperature balances. Multivariate balances are thus sensitive to the error simulation technique: **LAM EDA** enhances meso scale balances, while **DSC EDA** puts the emphasis on the synoptic scale balances.

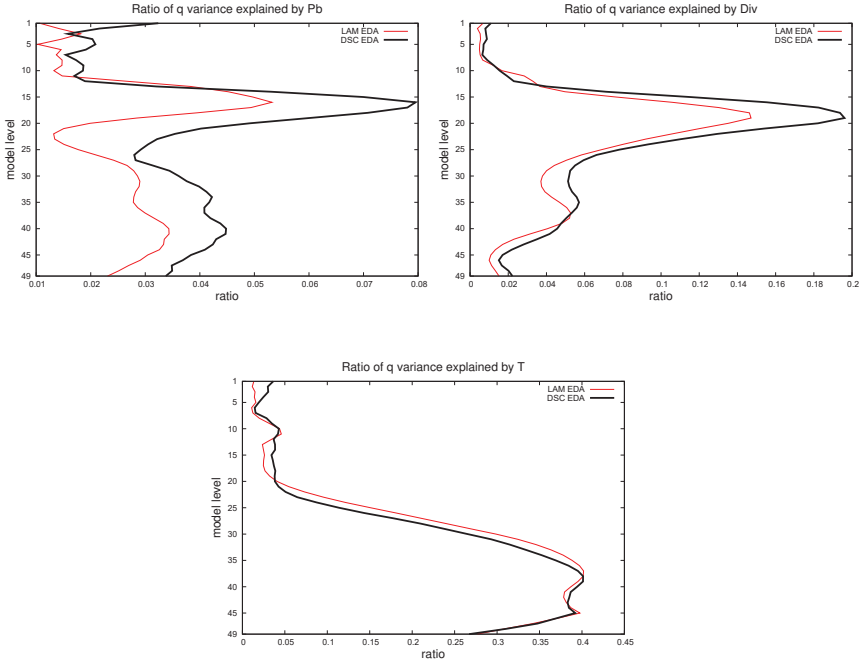

Figure 3.14: Explained variance of specific humidity by vorticity-balanced geopotential (top left), by unbalanced divergence (top right) and by unbalanced temperature (bottom middle). **DSC EDA**: black, **LAM EDA**: red

3.2.5 Impact of different analysis uncertainty representations in background error modeling: comparison in real assimilation and forecast experiments

Beside the diagnostic comparison of background error structure functions simulated by the **DSC EDA** and **LAM EDA** techniques, a very important aspect is to evaluate the impact of these techniques on the analysis and the short range forecast quality. To do this, two data assimilation cycles have been run using two different background error covariance matrices but otherwise both using the ALADIN/HU operational data assimilation settings. Namely, experiment **BT00** was using a background error covariance matrix based on the **DSC EDA** error simulation technique, while experiment **BT01** was using a background error covariance matrix based on the **LAM EDA** error simulation technique. From both assimilation cycles, 2 days production forecasts were run. The period of these impact studies was chosen to be the same as the error simulation period (July 2007), so that the time (weather) dependence of background error covariances does not play a role but uniquely the error simulation technique itself. Note that the time variability of background errors will be discussed in chapter 4.

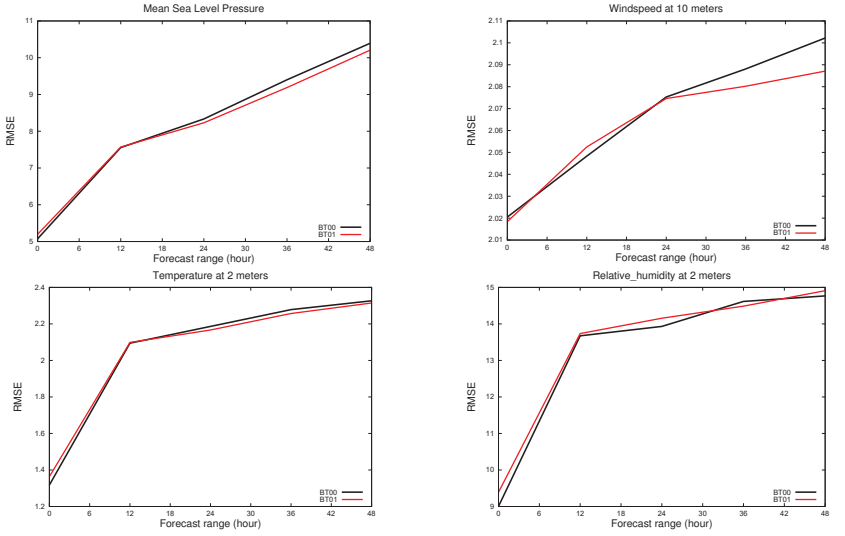

Figure 3.15: Screen level RMSE scores of experiments **BT00** (black) and **BT01** (red) for the 00 and 12 UTC runs together. Top left: mean sea level pressure (hPa), Top right: wind speed at 10m ($m\ s^{-1}$), Bottom left: temperature at 2m (K), Bottom right: relative humidity at 2m (%). The scores are computed against surface and radiosonde observations. Period: July 2007

The 2 days forecast of experiments **BT00** and **BT01** have been verified against surface and radiosonde observations and also against their own analyzes. The advantage of verifying against surface and radiosonde observations is that these informations are of relatively high accuracy, giving thus a good reference against the forecast information. On the other hand the spatial resolution of these observations is low compared to the model grid resolution, which leads to a poor representation of forecasted spatial structures. This is why also verification against gridded analyzes is performed, which can provide a reference in each forecasted grid-point including the information from observations as well. First the scores computed against observations are presented, which will be followed by the discussion of scores computed against gridded analyzes. Screen level (2m and 10m) RMSE scores computed

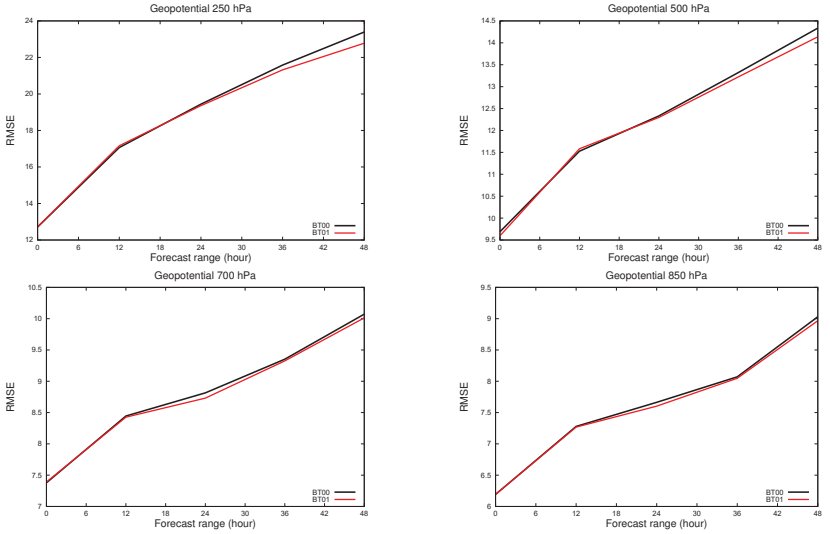

Figure 3.16: Geopotential RMSE scores ($m^2\ s^{-2}$) of experiments **BT00** (black) and **BT01** (red) for the 00 and 12 UTC runs together. The scores are computed against surface and radiosonde observations. Period: July 2007

against observations for the main prognostic variables are shown in Fig.3.15. An improvement by the **BT01** experiment for mean sea level pressure, wind speed and temperature can be observed, especially for the second day of the forecasts, while the impact on relative humidity is rather mixed depending on the forecast range. Upper air RMSE scores of geopotential are shown in Fig.3.16, where a clear improvement by **BT01** can be found for all vertical levels presented, mostly for the second forecasted day too. Similar conclusions can be drawn for wind speed (Fig.3.17) and temperature

(Fig.3.18). Relative humidity RMSE scores are also improved in experiment **BT01** above 850 hPa but are rather neutral below (Fig.3.19). Systematic errors (BIAS) for certain vertical levels are also plotted in Fig.3.20, where a mixed impact can be seen comparing experiments **BT00** and **BT01**. The BIAS of temperature at 850 hPa and relative humidity at 700 hPa is improved in experiment **BT01**. The 500 hPa geopotential BIAS is degraded in experiment **BT01** at the beginning of the forecast, while it improved for the forecast of the second day. The wind speed BIAS at 500 hPa is improved by experiment **BT01** at the beginning of the forecast but it is degraded for the long forecast ranges.

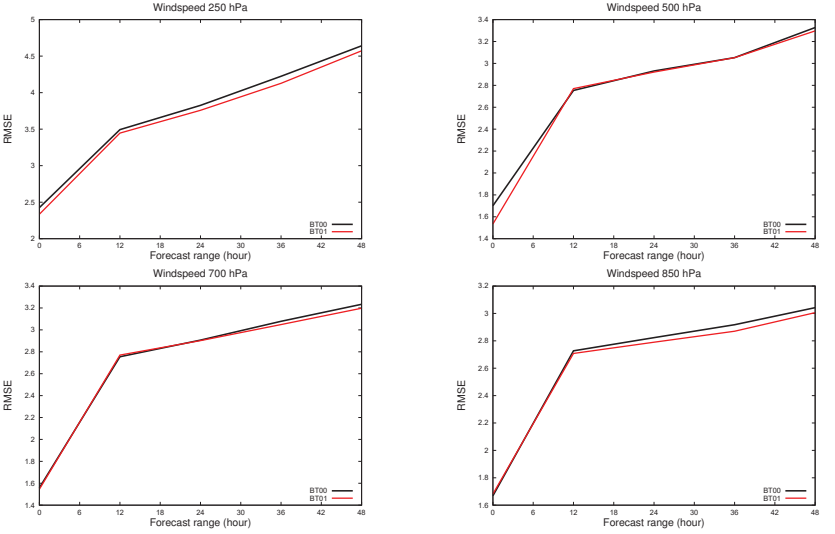

Figure 3.17: Wind speed RMSE scores ($m\ s^{-1}$) of experiments **BT00** (black) and **BT01** (red) for the 00 and 12 UTC runs together. The scores are computed against surface and radiosonde observations. Period: July 2007

The feature that **BT01** RMSE scores are slightly bit higher at the beginning and clearly lower for the second day forecast may come from the fact that the difference in the initial conditions (implied by the different background error covariance matrices used in **BT00** and **BT01**) is mostly in the small scales at the beginning of the forecast, which is not measurable by the surface and radiosonde observations due to their low spatial resolution. Later, during the forecast these small scale initial differences might also interact with (improve) larger scales, which become visible in the RMSE scores of longer ranges computed against observations.

The hypothesis above is somewhat supported by the verification scores computed against gridded analyzes, which are plotted in Fig.3.22 for the 00 UTC runs (12 UTC runs are not shown due to their similarity to the 00 UTC run scores). Namely, RMSE is lower for experiment **BT01** already at analysis time, probably due to the fact that in the gridded reference analysis also small scales are represented (unlike in the surface and radiosonde observing network). The improvement in experiment **BT01** compared to **BT00** is valid for all forecast ranges below 500 hPa roughly. A small degradation is found above 500 hPa in geopotential wind and temperature. Note that Fig.3.22 shows RMSE differences (**BT00**-**BT01**), which are positive if the RMSE of experiment **BT01** is lower (indicated by reddish colors in the figure). The small circles in the figures indicate those pressure levels and forecast ranges where the RMSE difference significantly differs from zero according to the T-probe with a 90% confidence.

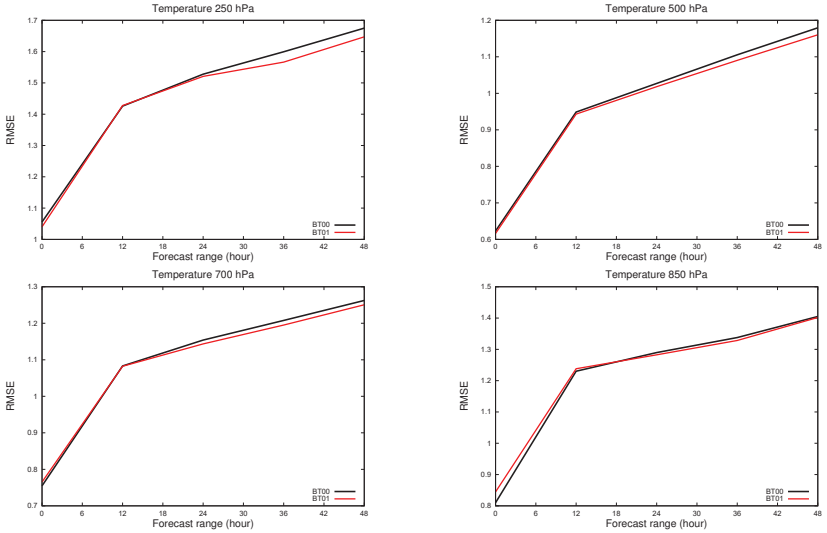

Figure 3.18: Temperature RMSE scores (K) of experiments **BT00** (black) and **BT01** (red) for the 00 and 12 UTC runs together. The scores are computed against surface and radiosonde observations. Period: July 2007

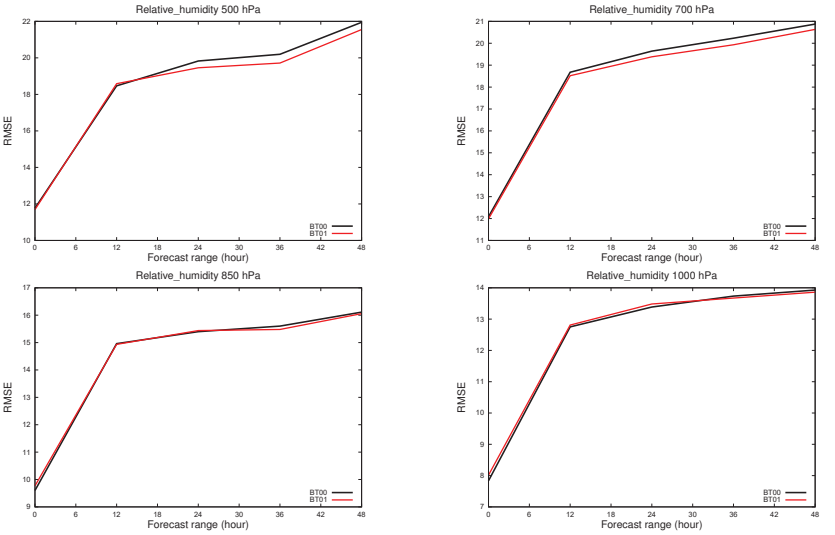

Figure 3.19: Relative humidity RMSE scores (%) of experiments **BT00** (black) and **BT01** (red) for the 00 and 12 UTC runs together. The scores are computed against surface and radiosonde observations. Period: July 2007

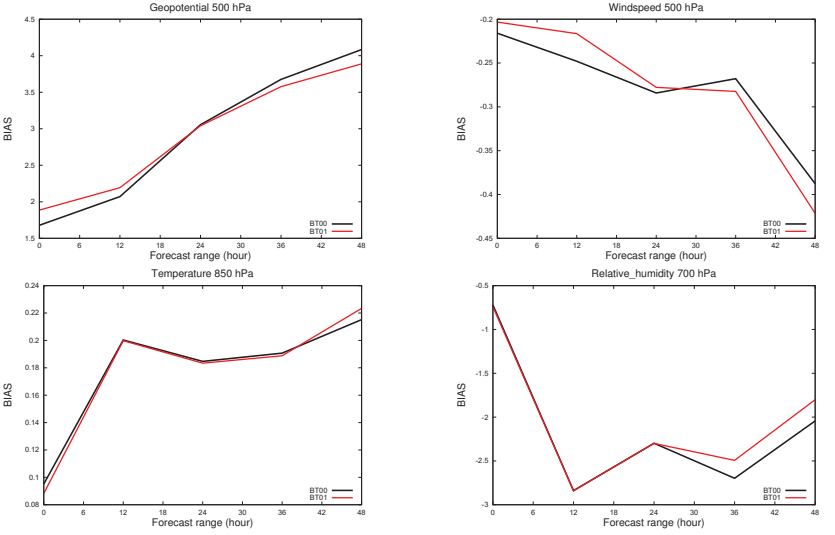

Figure 3.20: Upper air BIAS scores of experiments **BT00** (black) and **BT01** (red) for the 00 and 12 UTC runs together (see figures 3.16 - 3.19 for units and specifications).

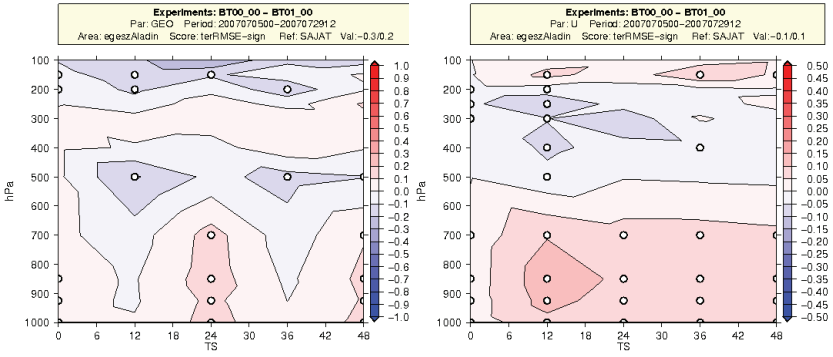

Figure 3.21: RMSE differences between experiments **BT00** and **BT01** for the 00 UTC runs. Left: geopotential ($m^2\ s^{-2}$), Right: wind u component ($m\ s^{-1}$). The scores are computed against the analysis of the same experiment. Period: July 2007

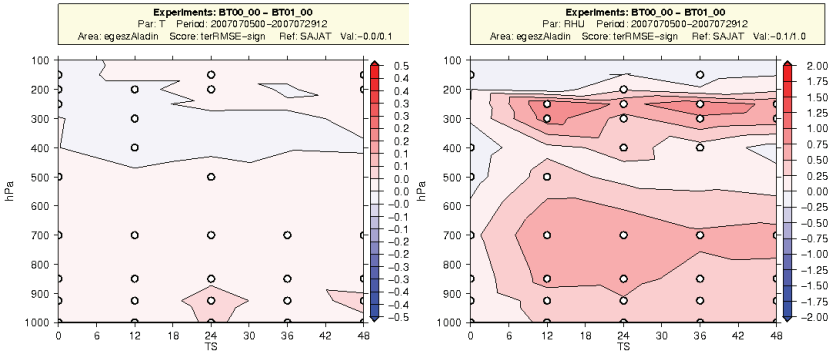

Figure 3.22: RMSE differences between experiments **BT00** and **BT01** for the 00 UTC runs. Left: temperature (K), Right: relative humidity ($\%$). The scores are computed against the analysis of the same experiment. Period: July 2007

3.3 Decomposition of LAM background errors to analysis and lateral boundary uncertainties

As stated before, for a successful LAM background error simulation, both analysis and lateral boundary uncertainties are to be accounted for, just like in experiment **LAM EDA** of section 3.2. For a better understanding the importance of these two components of background uncertainty, they are diagnosed separately in this section. Analysis uncertainty is diagnosed in a perfect LBC framework, while LBC uncertainty is diagnosed in a perfect initial condition framework. The diagnostics will also imply conclusions on the necessity of LAM data assimilation in itself through the exploration of relative importance of initial and lateral boundary conditions in short range LAM forecasts. Note that similarly to the previous section, the diagnostics are provided still in a perfect model framework.

3.3.1 The effect of analysis uncertainty: perfect LBC framework

The analysis uncertainty in a LAM can be diagnosed in a perfect LBC framework (on the top of the perfect model framework), i.e. when the error of the lateral boundary coupling is considered to be zero ($\mathcal{CP}M^G\boldsymbol{\epsilon}_a^{G(i-1)} = 0$). In this case, equation (3.21) simplifies to:

$$\boldsymbol{\epsilon}_b^{L(i)} = M^I\boldsymbol{\epsilon}_a^{L(i-1)} \tag{3.42}$$

In practice, such perfect LBC setup was constructed by running an ALADIN/HU LAM EDA system with local perturbation of the observations, but forcing all members of the ensemble data assimilation system to the same lateral boundary conditions (namely to the control member of the ECMWF EDA system) while running the background forecasts. Let us call this diagnostic experiment **PLBC** further on. As a result of this setup, the difference between the ensemble of background forecasts comes purely from the differences in the initial conditions, so such forecast differences will represent solely the analysis uncertainty.

3.3.2 The effect of uncertainties in the lateral boundary forcing: perfect initial condition framework

The LBC uncertainty can be diagnosed in a perfect initial condition (IC) framework (on the top of the perfect model framework), i.e. when the error of the initial conditions (analysis) is considered to be zero ($M^I\boldsymbol{\epsilon}_a^{L(i-1)} = 0$). In this case, equation (3.21) simplifies to:

$$\boldsymbol{\epsilon}_b^{L(i)} = \mathcal{CP}M^G\boldsymbol{\epsilon}_a^{G(i-1)} \tag{3.43}$$

Practically, such a perfect initial condition setup was achieved by running ensembles of ALADIN/HU forecasts starting from the same initial conditions (namely from the initial conditions of the **LAM**

EDA control member) but coupled to the different members of the ECMWF EDA system on the lateral boundaries. Let us call this diagnostic experiment **PIC** further on. As a result of this setup, the difference between the ensemble of background forecasts comes purely from the differences in the lateral boundary conditions, which means that the resulting forecast differences will represent solely the LBC uncertainty.

3.3.3 Diagnostic comparison of analysis- and lateral boundary condition uncertainties

In order to see the contribution of analysis and lateral boundary uncertainties to the full LAM background error uncertainty, the spectra of variances, correlation length-scales and PEACA diagnostics are discussed in this section for the three experiments **PLBC**, **PIC** and **LAM EDA** together.

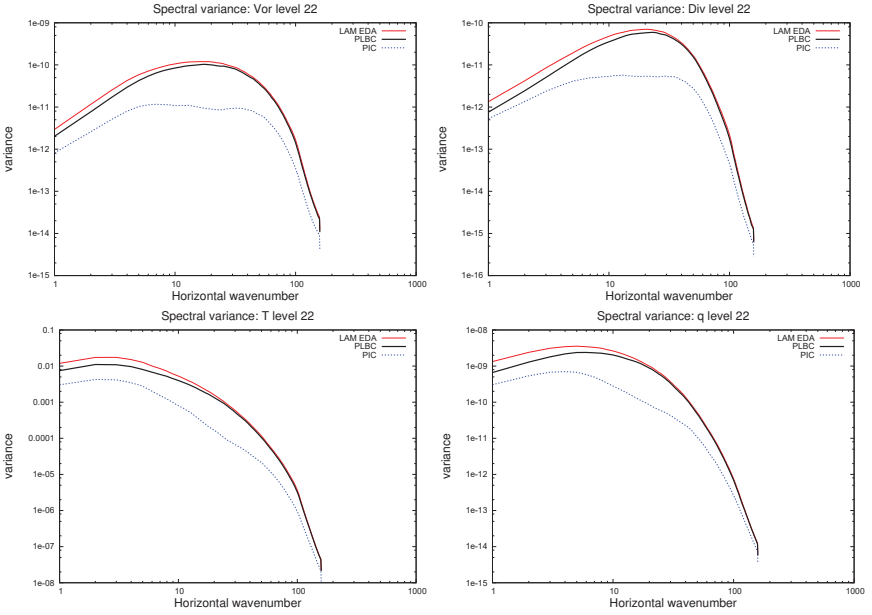

Figure 3.23: Variance spectra at ≈ 500 hPa (model level 22) comparing experiments **LAM EDA**, **PLBC** and **PIC**. Top left: vorticity (s^{-2}), Top right: divergence (s^{-2}), Bottom left: temperature (K^2), Bottom right: specific humidity ($g^2\ kg^{-2}$)

In Fig.3.23 the spectra of variances are plotted at ≈ 500 hPa (model level 22) for the three above-mentioned experiments. There is a clear decrease of variance on the large scales in experiment **PLBC** compared to **LAM EDA** for all the four variables. This shows that in case of discarding lateral boundary uncertainty (and keeping only the analysis uncertainty), the error variance is reduced (probably underrepresented) on the large scales (2600-250 km). This finding shows that the lateral boundary uncertainty affects more the large scale processes, which is a proof of the intuition that the coupling to a low resolution global model influences mostly the synoptic scales in short LAM forecasts. Looking at the variance spectra of experiment **PIC**, a clear decrease appears compared to **LAM EDA** both on large and small scales. It shows that suppressing the analysis uncertainty, the LAM background uncertainty is seriously underestimated both on large and small scales. The underestimation of error variance without taking into account the analysis uncertainty is even more expressed in the PBL (Fig.3.24) where the error variance at scales between 250 and 150 km is rather unrealistically reduced. Thus, based on variance spectra diagnostics, in short range forecasts (such as background

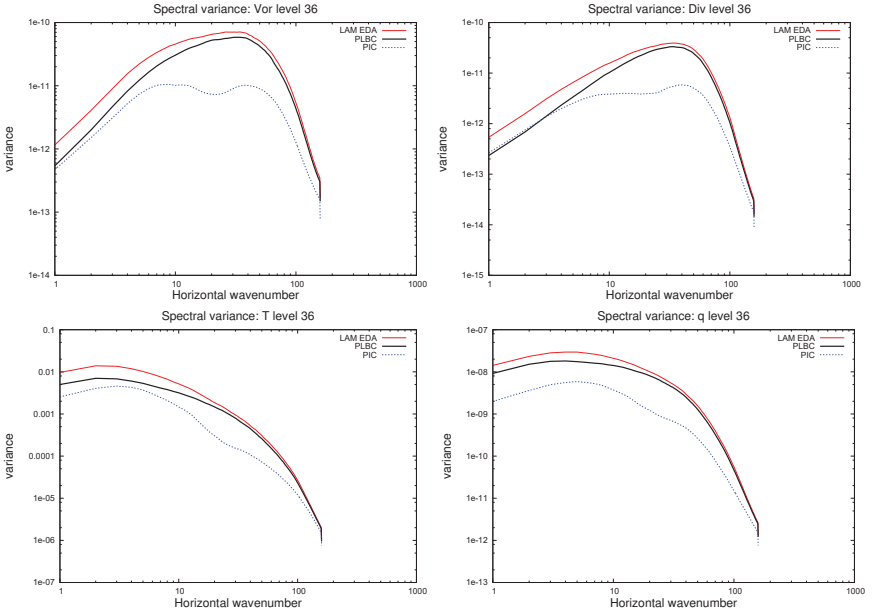

Figure 3.24: Variance spectra at ≈ 850 hPa (model level 36) comparing experiments **LAM EDA**, **PLBC** and **PIC**. Top left: vorticity (s^{-2}), Top right: divergence (s^{-2}), Bottom left: temperature (K^2), Bottom right: specific humidity ($g^2\ kg^{-2}$)

forecasts) the analysis uncertainty dominates over lateral boundary uncertainty both on synoptic and meso scales.

Besides the spectra of variances also correlation length-scale profiles were computed and plotted for the experiments **PLBC** and **PIC** and were compared to experiment **LAM EDA** (Fig.3.25). The correlation length-scales of temperature appear to be as it is expected intuitively. Namely, length-scales are the largest for experiment **PLBC**, followed by **LAM EDA** and finally by **PIC** being the smallest. The intuitive expectation for this order can be explained as follows. Large scale (large distance) background error correlations are due to the LBC uncertainty (coming from the low resolution coupling model forcing), which is suppressed in experiment **PLBC** resulting in small correlation length-scales compared to **LAM EDA**. On the other hand, small scale (small distance) background

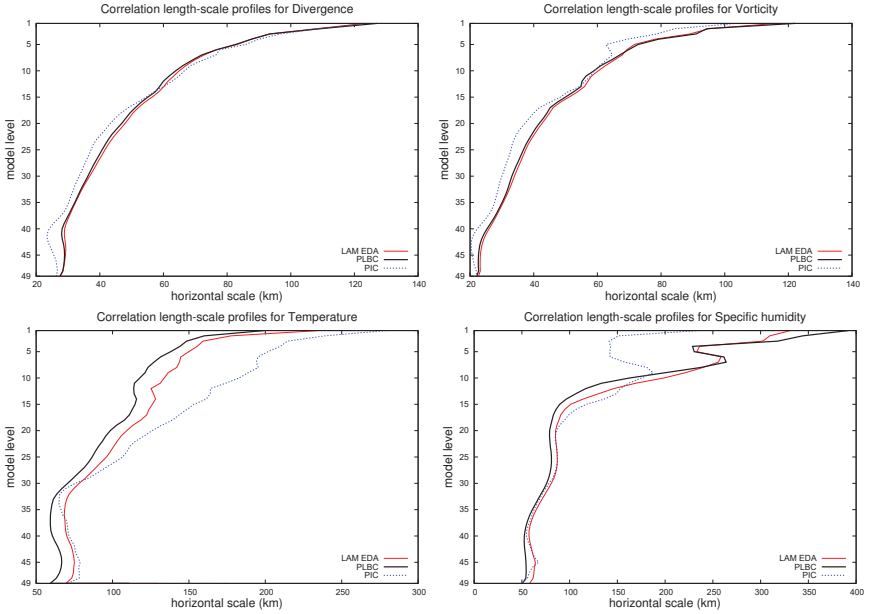

Figure 3.25: Correlation length-scale profiles deduced from the experiments **LAM EDA**, **PLBC** and **PIC**. Top left: vorticity, Top right: divergence, Bottom left: temperature, Bottom right: specific humidity.

error correlations are due to the analysis uncertainty (coming from small scale analysis structures introduced by the high resolution initial conditions), which is suppressed in experiment **PIC** resulting in larger correlation length-scales compared to **LAM EDA**. This classical interpretation is not valid for the wind (vorticity and divergence), where the lack of analysis uncertainty (experiment **PIC**) further decreases the correlation length-scales compared to experiment **PLBC** and **LAM EDA**, which are rather close to each other. This picture suggests that in the wind field, the analysis uncertainty implies

large scale (large distance) correlations instead of small scales, and these large scale correlations are more important than those implied by the LBC uncertainty.

PEACA diagnostics comparing experiments **LAM EDA PLBC** and **PIC** are also plotted in Fig.3.26. These figures clearly show that suppressing any of the two sources of uncertainty (analysis or LBC), implies an underestimation of background error uncertainty. The lack of representing the analysis uncertainty (experiment **PIC**) affects mostly the small, while the lack of LBC uncertainty (experiment **PLBC**) affects mostly the large scales.

As proved by the above diagnostics, a consequence of under-representing the analysis uncertainty will result in misrepresentation of the background errors, especially on the small scales. This is what also gave motivation for the work discussed in the previous section, namely, to introduce local (LAM) analysis uncertainty to the error simulation techniques instead of simply downscaling the global model analysis uncertainty.

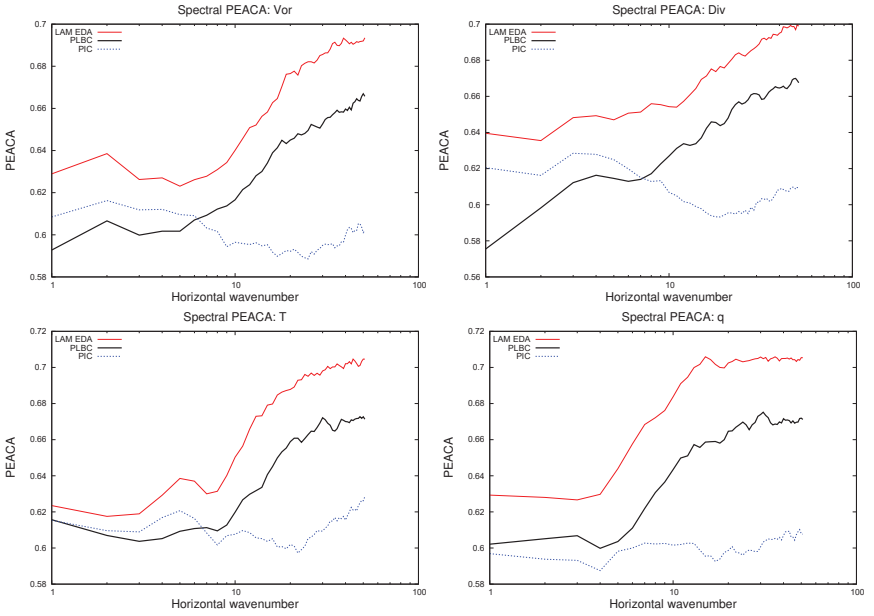

Figure 3.26: PEACA correlation in the function of the logarithm of the wavenumber at level 36 (≈ 850 hPa) deduced from the experiments **LAM EDA**, **PLBC** and **PIC**. Top left: vorticity, Top right: divergence, Bottom left: temperature, Bottom right: specific humidity.

3.4 Simulation of model uncertainty within a LAM Ensemble Data Assimilation framework

So far, all along chapter 3, a perfect model approach was applied neglecting the model error $\mathbf{e}_M$ and its covariance matrix $\mathbf{Q}$ introduced in section 2.3 (equations 2.19 and 2.25) and only the analysis and LBC uncertainties were accounted for. As explained earlier, the LBC uncertainty comes into play only in a LAM framework. The perfect model approach in a LAM can be written as:

$$\boldsymbol{\epsilon}^{L\,(i)}_{M} \;=\; \mathbf{x}_t^{(i)} - M^L \mathbf{x}_t^{(i-1)} = 0 \rightarrow E(\boldsymbol{\epsilon}^L{}_M \boldsymbol{\epsilon}^{L\,T}_{M}) = \mathbf{Q}^L = 0 \tag{3.44}$$

Perfect model framework has been a rather commonly used simplification in background error simulation up to recent years. Today the simulation of the matrix $\mathbf{Q}$ is one of the important challenges in the research field of data assimilation ([40] *Houtekamer et al.* 2009, [46] *Li et al.* 2009, [63] *Zupanski and Zupanski* 2006).

3.4.1 Perturbation of physical parametrizations for the representation of model error

In this section also an attempt to simulate model error is presented, with the goal of a more complete representation of the ALADIN/HU background errors (besides the analysis and LBC errors). The idea we applied to represent model error, is based on the multi-physics approach. In this context we assume that an important part of the model error originate from the physical parametrizations (besides the time and space discretisation errors and other possible conceptual errors of the model). Within this approach, the model error can be represented by forecast differences corresponding to runs starting from the same initial conditions but using different physical parametrization settings:

$$\boldsymbol{\epsilon}^{L\,(i)}_{M} \approx M_1^L \mathbf{x}_a^{(i-1)} - M_2^L \mathbf{x}_a^{(i-1)} \tag{3.45}$$

where M_1^L stands for the ALADIN forecast model (version[3] cy33t1) using the ALADIN/HU operational physics package[4] and M_2^L stands for the ALADIN forecast model (version cy35t1) using a more advanced physics package, so called ALARO physics. These two physical parametrization setups differ mostly in the parametrization of convection and micro-physical processes, but also the turbulence and horizontal diffusion schemes differ in a reasonable extent. Namely, the operational ALADIN/HU (M_1^L) is run with a deep convection scheme by [13] *Bougeault* (1985), with a shallow convection scheme by [30] *Geleyn* (1987) and with a simple diagnostic scheme for precipitation parametrization

[3] The versioning number corresponds to the code version of the ARPEGE/ALADIN/AROME software phased together with the ECMWF/IFS code, which has been done since the 1970's

[4] In the meantime M_1^L has been changed to M_2^L for the operational ALADIN/HU runs, due to its better performance

([45] *Kessler* 1995). On the other hand, the more advanced ALARO physics (M_2^L) are based on a new multi-scale scheme for convection parametrization with a full prognostic micro-physical package ([32] *Gerard* 2007, [31] *Geleyn et al.* 2008, [33] *Gerard et al.* 2009). The dynamics of M_1^L and M_2^L also differ considerably. Namely the first one uses a spectral horizontal diffusion scheme for the representation of energy loss by wind-shear, while the latter involves the so called Semi-Lagrangian Horizontal Diffusion (SLHD) scheme ([62] *Vana et al.* 2008), which is more physical given the fact that the diffusion is proportional to the horizontal space derivatives of wind (i.e. the wind-shear), taken from the Semi-Lagrangian interpolation step.

In the context of the LAM decomposition of background errors (equation (3.21)), the above model error representation can be written as:

$$\begin{aligned}
\boldsymbol{\epsilon}_M^{L(i)} &\approx (M_1^I \mathbf{x}_a^{(i-1)} + \mathcal{CP}M^G \mathbf{x}_a^{G(i-1)}) - (M_2^I \mathbf{x}_a^{(i-1)} + \mathcal{CP}M^G \mathbf{x}_a^{G(i-1)}) && (3.46)\\
&= M_1^I \mathbf{x}_a^{(i-1)} - M_2^I \mathbf{x}_a^{(i-1)} && (3.47)\\
&= \boldsymbol{\epsilon}_M^{I(i)} && (3.48)
\end{aligned}$$

if the lateral boundary conditions ($\mathcal{CP}M^G \mathbf{x}_a^{G(i-1)}$) are the same in both runs. In practice the above model error representation was implemented by rerunning only the unperturbed member of the LAM ensemble assimilation system with the ALARO physics setup (M_2^I) and making the forecast differences between this member and the original perturbed members run with the ALADIN/HU operational physics. This means that in this experiment, the model error (equation (3.48)) was represented as an additional source of uncertainty, besides those coming from the analysis and the LBCs, when simulating the background error. Using the subscript k for the new control member, the following formulation describes the experiment done:

$$\begin{aligned}
\boldsymbol{\epsilon}_b^{L(i)} &= (M_1^I \mathbf{x}_{a,k}^{L(i-1)} + \mathcal{CP}M^G \mathbf{x}_{a,k}^{G(i-1)}) - (M_2^I \mathbf{x}_{a,l}^{L(i-1)} + \mathcal{CP}M^G \mathbf{x}_{a,l}^{G(i-1)}) && (3.49)\\
&= M_1^I \mathbf{x}_{a,k}^{L(i-1)} - M_2^I \mathbf{x}_{a,l}^{L(i-1)} + \mathcal{CP}M^G \boldsymbol{\epsilon}_a^{G(i-1)} && (3.50)\\
&= M_1^I \mathbf{x}_{a,k}^{L(i-1)} - M_2^I \mathbf{x}_{a,l}^{L(i-1)} - M_1^I \mathbf{x}_{a,l}^{L(i-1)} + M_1^I \mathbf{x}_{a,l}^{L(i-1)} + \mathcal{CP}M^G \boldsymbol{\epsilon}_a^{G(i-1)} && (3.51)\\
&= (M_1^I \mathbf{x}_{a,k}^{L(i-1)} - M_1^I \mathbf{x}_{a,l}^{L(i-1)}) + \mathcal{CP}M^G \boldsymbol{\epsilon}_a^{G(i-1)} + (M_1^I \mathbf{x}_{a,l}^{L(i-1)} - M_2^I \mathbf{x}_{a,l}^{L(i-1)}) && (3.52)\\
&= M_1^I \boldsymbol{\epsilon}_a^{L(i-1)} + \mathcal{CP}M^G \boldsymbol{\epsilon}_a^{G(i-1)} + \boldsymbol{\epsilon}_M^{I(i)} && (3.53)
\end{aligned}$$

Thus, within this simulation experiment all the three sources of LAM background uncertainty are accounted for, namely those coming from analysis ($M_1^I \boldsymbol{\epsilon}_a^{L(i-1)}$), LBC ($\mathcal{CP}M^G \boldsymbol{\epsilon}_a^{G(i-1)}$) and model errors ($\boldsymbol{\epsilon}_M^{I(i)}$). The simulation experiment (which will be referred as **LAM EDA+Q** further on) was run for the same period as all the previous experiments. This makes possible a comparison with the **LAM EDA** experiment showing the pure impact of the additional model error representation on the previously presented diagnostics and on the ALADIN/HU analyzes and model forecasts.

3.4.2 Diagnosing the effect of model error representation

Figures 3.27 and 3.28 show the spectra of simulated background error variance for all the previous error simulation experiments (**DSC EDA**, **PLBC**, **PIC**, **LAM EDA** and **LAM EDA+Q**) at $\approx$ 500 (model level 22) and $\approx$ 850 hPa (model level 36). Comparing the experiments **LAM EDA** and **LAM EDA+Q** shows that in the free atmosphere the representation of model error does not modify the error variance very much, only in a small extent and especially on the large scales. On the other hand, lower in the PBL, the representation of model error increases the simulated background error variance in a larger extent, especially at small scales (30-60 km). This seems to be a reasonable behavior,

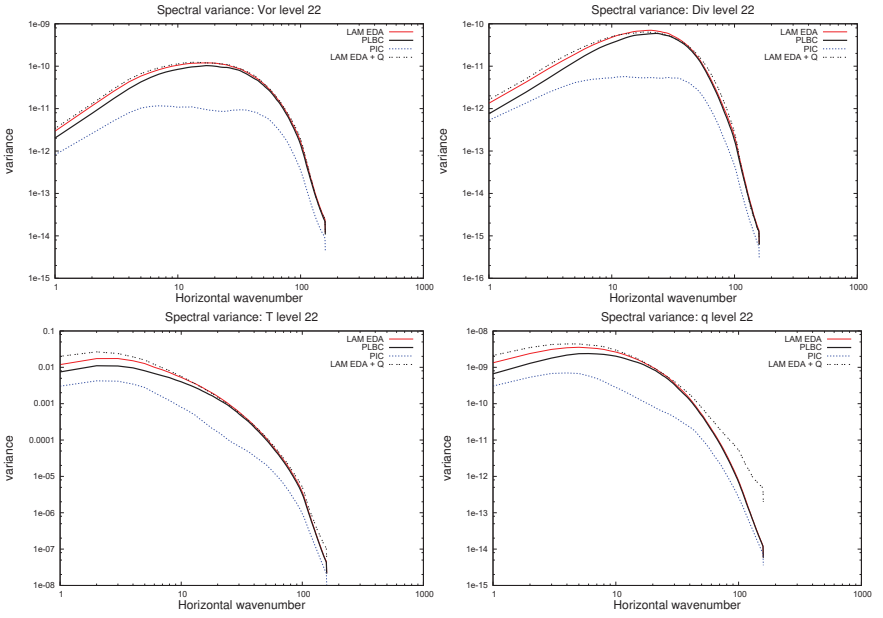

Figure 3.27: Variance spectra at $\approx$ 500 hPa (model level 22) comparing experiments **LAM EDA+Q**, **LAM EDA**, **PLBC** and **PIC**. Top left: vorticity (s^{-2}), Top right: divergence (s^{-2}), Bottom left: temperature (K^2), Bottom right: specific humidity ($g^2\ kg^{-2}$)

given the fact that in the applied experiments the model error is represented by differences in the physical parametrization of convection and the related micro-physics, which is most relevant for the PBL and mostly for the meso scales. PEACA diagnostics are plotted in Fig.3.29 and 3.30 for $\approx$ 500

hPa (model level 22) and ≈ 850 hPa (model level 36) respectively, which show a better representation (higher correlation) of background errors by experiment **LAM EDA+Q** compared to **LAM EDA** generally. At 500 hPa, this is true only for the large scales (mostly for divergence and humidity), while in the PBL (850 hPa) the improvement by experiment **LAM EDA+Q** is more expressed, and with an emphasis on the small scales. This again might reflect the way of model error representation in experiment **LAM EDA+Q**, namely the difference between the convection parametrization schemes in M_1^I and M_2^I.

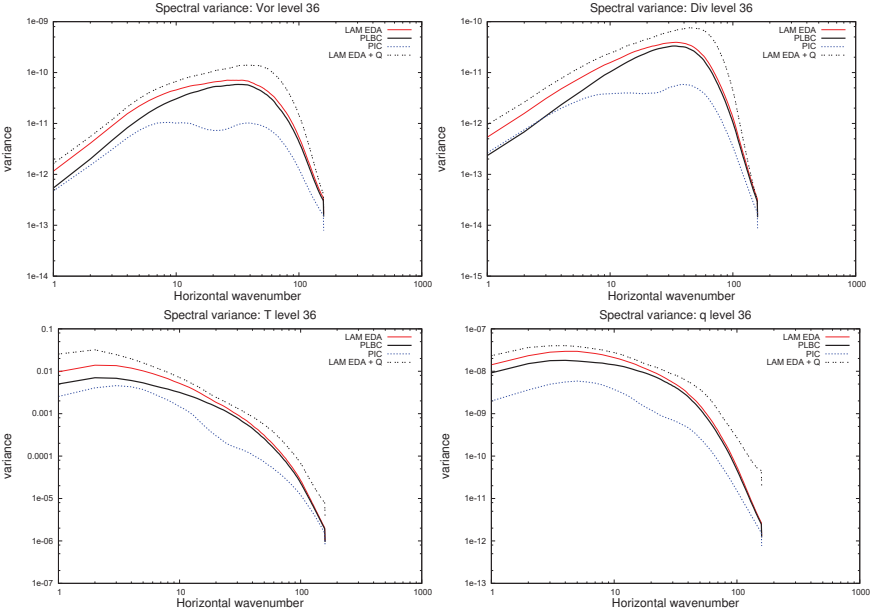

Figure 3.28: Variance spectra at ≈ 850 hPa (model level 36) comparing experiments **LAM EDA+Q**, **LAM EDA**, **PLBC** and **PIC**. Top left: vorticity (s^{-2}), Top right: divergence (s^{-2}), Bottom left: temperature (K^2), Bottom right: specific humidity ($g^2\ kg^{-2}$)

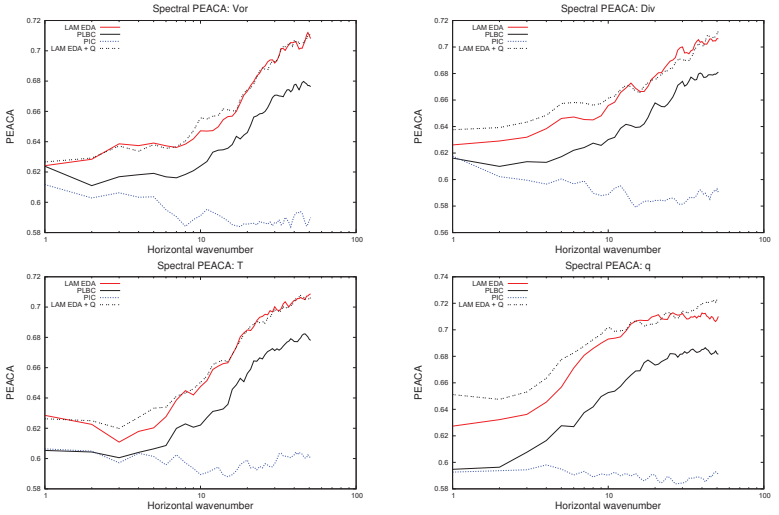

Figure 3.29: PEACA correlation in the function of the logarithm of the wavenumber at level 22 (≈ 500 hPa) deduced from the experiments **LAM EDA+Q**, **LAM EDA**, **PLBC** and **PIC**. Top left: vorticity, Top right: divergence, Bottom left: temperature, Bottom right: specific humidity.

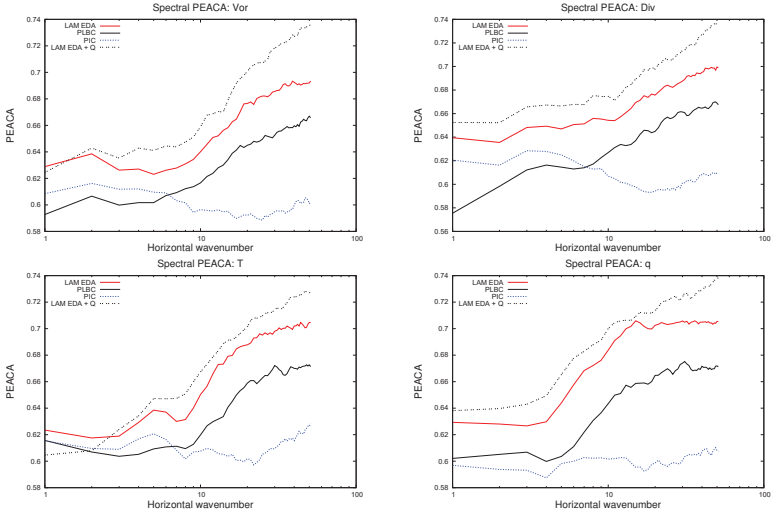

Figure 3.30: Same as Fig.3.29 but for level 36 (≈ 850 hPa)

3.4.3 Impact of model error representation

Given that the representation of model error made an effect on the diagnostics shown, an assimilation and forecast impact study was also performed, assessing how the background error covariance matrix involving simulated model errors (represented by experiment **LAM EDA+Q**) affects the quality of ALADIN/HU analyzes and 2 days forecasts. The experiment using the background error covariance matrix sampled by experiment **LAM EDA+Q** is referred as **BT06** further on. The selected period was the same as for the impact studies comparing **BT00** and **BT01** (i.e. July 2007, which is the same as the sampling period). The RMSE and BIAS scores against surface and radiosonde observations for experiments **BT01** and **BT06** are shown in Fig.3.31-3.34. A considerable improvement by

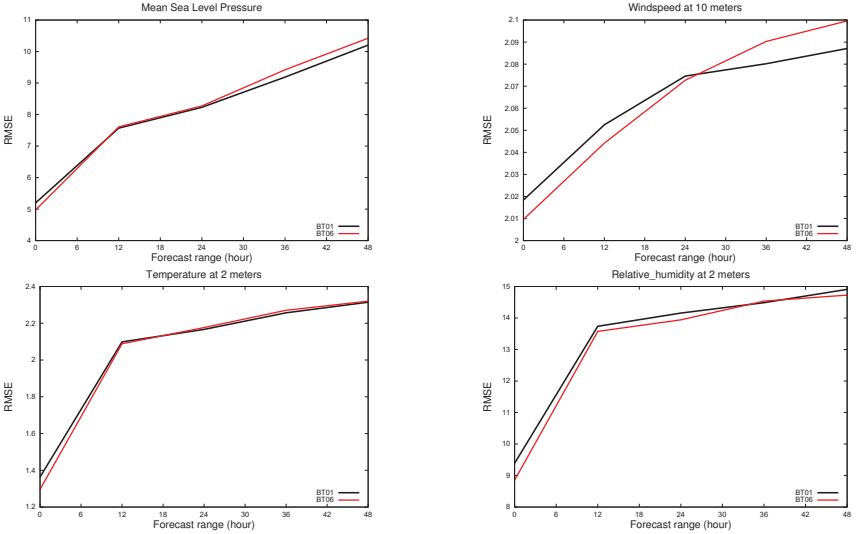

Figure 3.31: Screen level RMSE scores of experiments **BT01** (black) and **BT06** (red) for the 00 and 12 UTC runs together. Top left: mean sea level pressure (hPa), Top right: wind speed at 10m ($m\ s^{-1}$), Bottom left: temperature at 2m (K), Bottom right: relative humidity at 2m ($\%$). The scores are computed against surface and radiosonde observations. Period: July 2007

experiment **BT06** was found for 2 meters temperature and relative humidity RMSE (Fig.3.31) and BIAS (Fig.3.32), while the impact is rather mixed for sea-level pressure and 10 meters wind. The changes in screen level scores implied by experiment **BT06** are especially interesting because these

are the levels, which were not affected by the introduction of the better representation of analysis uncertainty of **LAM EDA** in comparison to **DSC EDA**. Thus, in this sense, the representation of model errors (by experiment **LAM EDA+Q**) is complementary to the representation of LAM analysis uncertainty (by experiment **LAM EDA**). Scores computed for the free atmosphere show a rather mixed impact, which means that the representation of model error does not imply a clear improvement of forecast quality there in terms of fit to observations. Looking at verification scores against analyzes (Fig.3.36), experiment **BT06** outperforms **BT01** on high vertical levels but degrades the PBL forecast of temperature and geopotential. All this implies that there is a potential in the multi-physics approach for the representation of model uncertainty in background error simulation, but one has to be careful when defining the physics perturbation in order to assess an appropriate response in the background error covariance matrix and though in the provided analyzes and forecasts.

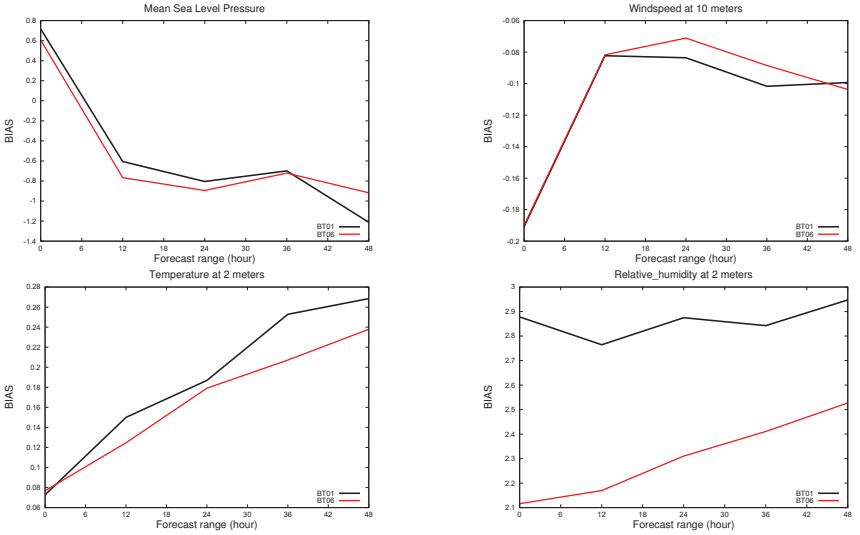

Figure 3.32: Screen level BIAS scores of experiments **BT01** (black) and **BT06** (red) for the 00 and 12 UTC runs together. Top left: mean sea level pressure (hPa), Top right: wind speed at 10m ($m\ s^{-1}$), Bottom left: temperature at 2m (K), Bottom right: relative humidity at 2m ($\%$). The scores are computed against surface and radiosonde observations. Period: July 2007

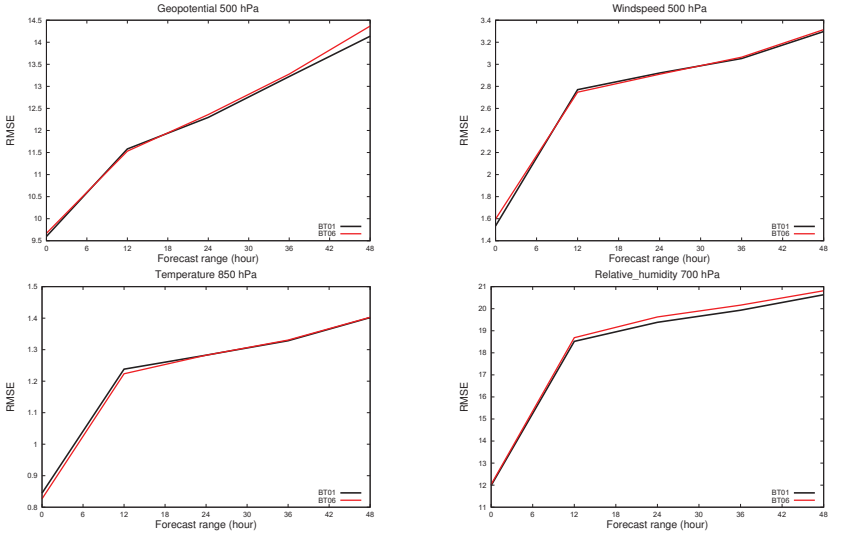

Figure 3.33: Upper air RMSE scores of experiments **BT01** (black) and **BT06** (red) for the 00 and 12 UTC runs together. The scores are computed against surface and radiosonde observations. Period: July 2007 (see figures 3.31 - 3.32 for units).

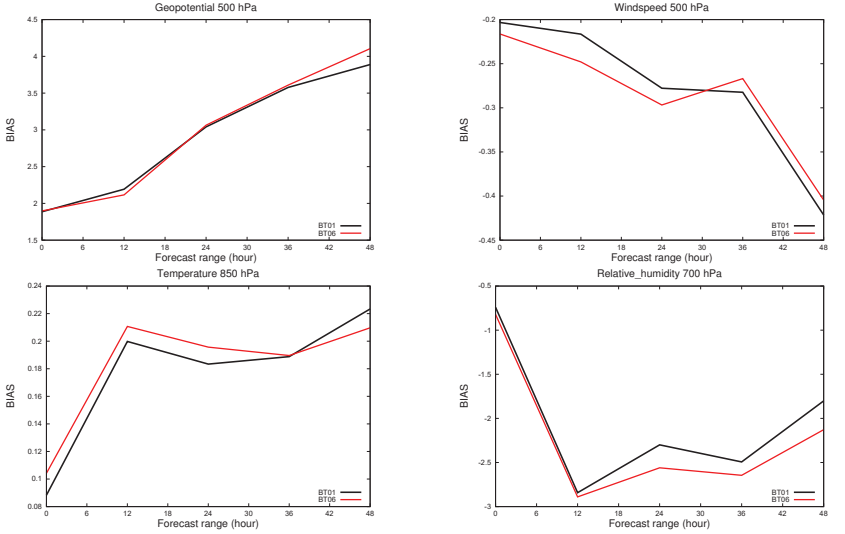

Figure 3.34: Same as Fig.3.33 but for BIAS.

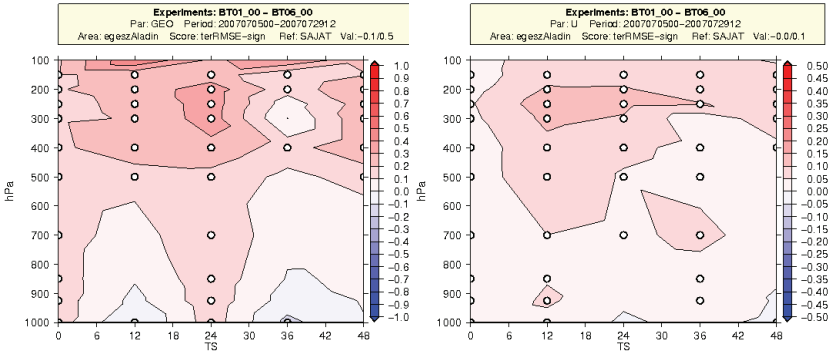

Figure 3.35: RMSE differences between experiments **BT01** and **BT06** for the 00 UTC runs. Left: geopotential ($m^2\ s^{-2}$), Right: wind u component ($m\ s^{-1}$). The scores are computed against the analysis of the same experiment. Period: July 2007

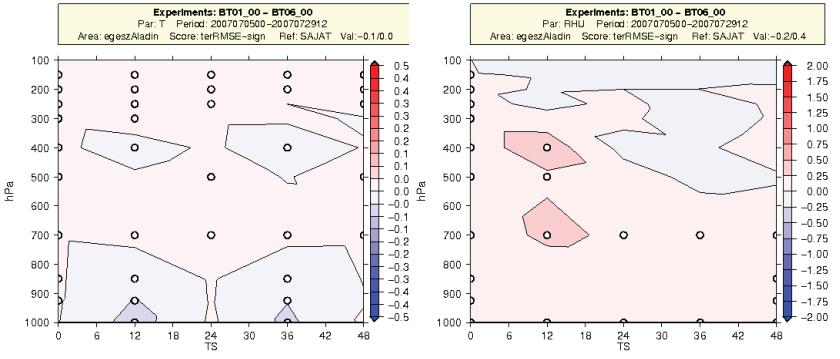

Figure 3.36: RMSE differences between experiments **BT01** and **BT06** for the 00 UTC runs. Left: temperature(K), Right: relative humidity ($\%$). The scores are computed against the analysis of the same experiment. Period: July 2007

3.5 Discussion

Applying the definition of covariance matrix to the most general form of the simulated LAM background error $\boldsymbol{\epsilon}^{L_b^{(i)}}$ (equation (3.53)), and assuming that LAM and global analysis errors are uncorrelated, as well as analysis and model errors (i.e. $E(\boldsymbol{\epsilon}^{L}{}_{a}\boldsymbol{\epsilon}^{G}{}_{a}{}^{T}) = E(\boldsymbol{\epsilon}^{L}{}_{a}\boldsymbol{\epsilon}^{I}{}_{M}{}^{T}) = E(\boldsymbol{\epsilon}^{G}{}_{a}\boldsymbol{\epsilon}^{I}{}_{M}{}^{T}) = 0$), one gets:

$$
\begin{aligned}
E(\boldsymbol{\epsilon}^{L_b^{(i)}}\boldsymbol{\epsilon}^{L_b^{(i)^T}}) &= M^I E(\boldsymbol{\epsilon}^{L_a^{(i-1)}}\boldsymbol{\epsilon}^{L_a^{(i-1)^T}}) M^{I^T} && (3.54)\\
&+ \mathcal{C}\mathcal{P}M^G E(\boldsymbol{\epsilon}^{G_a^{(i-1)}}\boldsymbol{\epsilon}^{G_a^{(i-1)^T}}) M^{G^T}\mathcal{P}^T\mathcal{C}^T && (3.55)\\
&+ E(\boldsymbol{\epsilon}^{I_M^{(i)}}\boldsymbol{\epsilon}^{I_M^{(i)^T}}) && (3.56)
\end{aligned}
$$

That is:

$$
\mathbf{B}^{L^{(i)}} = M^I \mathbf{A}^{L^{(i-1)}} M^{I^T} + \mathcal{C}\mathcal{P}M^G \mathbf{A}^{G^{(i-1)}} M^{G^T}\mathcal{P}^T\mathcal{C}^T + \mathbf{Q}^{I^{(i)}} \quad (3.57)
$$

This formula shows again the three different sources of errors that are composed in the LAM background error covariance matrix but this time in a matrix form. The first term of the right hand side corresponds to the background error that originates from the time evolution of the pure LAM analysis error, i.e. to the LAM analysis uncertainty. The second term corresponds to the background error that originates from the LBC uncertainty (i.e. the time evolution of the coupling model's analysis uncertainty plus the uncertainty of the interpolation and the coupling procedure). The third term corresponds to the background error that originates from the LAM model errors (in our case from the uncertainty in the physical parametrizations). The first term does not exist in a perfect initial condition framework, the second term is zero in a perfect LBC framework and the third term disappears in a perfect model framework. The contribution of these elements to the full LAM background error covariance matrix (i.e. their relative importance) can be estimated if looking at Figures 3.27-3.30 again, where perfect initial (**PIC**), perfect LBC (**PLBC**) and perfect model (**LAM EDA**) framework diagnostics are all shown (spectrum of estimated error variance and PEACA) together with the diagnostics of full background error representation (**LAM EDA+Q**). Based on these figures, all of the three uncertainty sources has an important role in background error representation, although their relative importance varies depending on the horizontal scale, on the height and on the diagnostic type.

Contribution of the LAM analysis uncertainty ($M^I\mathbf{A}^L M^{I^T}$): Both the spectra of estimated error variance and the PEACA diagnostics show that the representation of analysis uncertainty is the most important among the three (low variance and PEACA of experiment **PIC**). According to the PEACA diagnostics the lack of analysis uncertainty representation is especially detrimental on the small horizontal scales. This might mean that pure LBC uncertainty need more than 6 hours to penetrate towards small spatial scales. The comparison of the **DSC EDA** and **LAM EDA** analysis error representations, shows that a direct error simulation of the LAM analysis uncertainty is more efficient than the downscaling of the analysis uncertainty from global assimilation systems.

Contribution of the LBC uncertainty ($\mathcal{C}\mathcal{P}M^G\mathbf{A}^G M^{G^T}\mathcal{P}^T\mathcal{C}^T$): Based on the spectrum of error variance, the uncertainty in the LBCs is mostly important on large horizontal scales (somewhat lower variances in experiment **PLBC**), while in the PEACA diagnostics it proves to be rather important also on small scales. This means that the LAM analysis uncertainty can't provide the full background uncertainty alone, especially concerning the large scales, which might come from the fact that the maximum length-scales analyzed (and so perturbed) in the LAM are bound to the domain size. This might lead to the underrepresentation of some planetary scale uncertainties, which are included only in the LBC uncertainty.

Contribution of the model uncertainty ($\mathbf{Q}^I$): Model uncertainty is important in low levels mostly and especially at small horizontal scales. As explained earlier this might come from the way of model error representation applied, i.e. from the uncertainty of physical parametrizations of convection and micro-physics primarily.

As far as the impact of different background error simulation techniques on the forecast quality is concerned, it was found that the direct simulation of LAM analysis uncertainty (**LAM EDA**) implies better 2 days forecasts than the downscaling of the analysis uncertainty (**DSC EDA**). The representation of model uncertainty in the error simulation technique (**LAM EDA + Q**) has the ability to further improve the forecast of certain parameters compared to the case when the **LAM EDA** technique is applied, although in some other parameters the latter technique leads to better forecasts.

The above findings are especially interesting, as their understanding leads beyond the context of background error modeling. Namely, the knowledge on the uncertainty sources in forecast errors helps to point out the weaknesses of forecast models, and consequently, might provide useful guidelines for effective corrections in short range NWP systems. The presented results suggest that for the very short range (6 hours), the forecasts are the most sensitive to the initial conditions. This implies that for the very short range NWP systems, data assimilation is a key issue. Besides the sensitivity to the initial conditions, the sensitivity to physical parametrizations is also very important and especially for the meso scales. This indicates that room for improvement is also left in the field of model physics development. Finally, the sensitivity to the lateral boundary conditions is also remarkable, however it seems to be less of importance compared to the previous two sensitivities for the very short range.

It is important to mention, that the above results are not necessarily valid for forecast ranges longer than 6 hours, where gradually, the sensitivity to the lateral boundary conditions might increase with the forecast range. The operational practice of short range numerical weather prediction (up to 2-3 days) shows an important sensitivity to all the three uncertainty sources discussed (initial conditions, lateral boundary conditions, physical parametrizations).

Chapter 4

Weather dependence of background errors

Background errors vary in time due to the different predictability limits of NWP models in different weather situations. The time evolution of the background error covariance matrix is described by the Kalman Filter equations (2.25), which are yet far too much expensive to solve for large dimension systems such as NWP. Simplifications of the Kalman Filter theory aim to reduce the large dimension of the problem, while still keeping the most important components of the evolving background error covariances. Such schemes are the Ensemble Kalman Filter ([24] *Evensen* 1994), the Ensemble Transform Kalman Filter ([4] *Bishop et al.* 2001) or the Reduced-rank Kalman Filter ([27] *Fisher* 1998). This chapter of the thesis is also dedicated to assess the weather dependence of background error covariances. In this aspect we do not go as far as accounting for the flow-dependent regular update of the background error covariance matrix as enabled by the above cited methods. Instead, the variability of background errors to the seasonal and diurnal weather changes is studied, based on climatological aggregates of ALADIN forecast differences. To assess the seasonal variability, the aggregates were provided by the downscaling of the global Ensemble Assimilation system of the ARPEGE French global model (EnVar). In practice, these forecast differences are created exactly like in experiment **DSC EDA** of the previous chapter, i.e. the initial conditions were provided by interpolation from the global systems. To elaborate the diurnal variability, the forecast differences were provided by running LAM Ensemble Assimilation experiments (as experiment **LAM EDA** explained in the previous chapter) coupled the ECMWF EDA system. Note that a similar diagnostic study using a LAM Ensemble Assimilation system is discussed by [50] *Monteiro and Berre* (2010).

4.1 Seasonal variability

The seasonal variability of background errors was accounted for by comparing background error statistics coming from two error simulation experiments based on summer and on winter forecast

differences. Both simulation experiments were based on the downscaling of the ARPEGE EnVar system. The summer experiment was run for the period 1 - 31 July 2008 and will be referred to as experiment **SUMMER**, while the winter experiment was run for the period 1 - 31 January 2009 and will be referred to as experiment **WINTER**. The beginning of the summer period was mainly characterized by fronts passing Central Europe, while the second half included mostly light pressure gradients, thus mostly characterized by isolated convection events. The winter period contained both front passing events, as well as high pressure situations with low cloudiness and inversion.

4.1.1 Diagnostic comparison of summer and winter background error statistics

The spectra of background error variance is compared for the experiments **SUMMER** and **WINTER** in Fig.4.1-4.2. The comparison shows that the background error variance is increased for the summer period at least on the small scales. This is somewhat more emphasized in the PBL (≈850 hPa). For

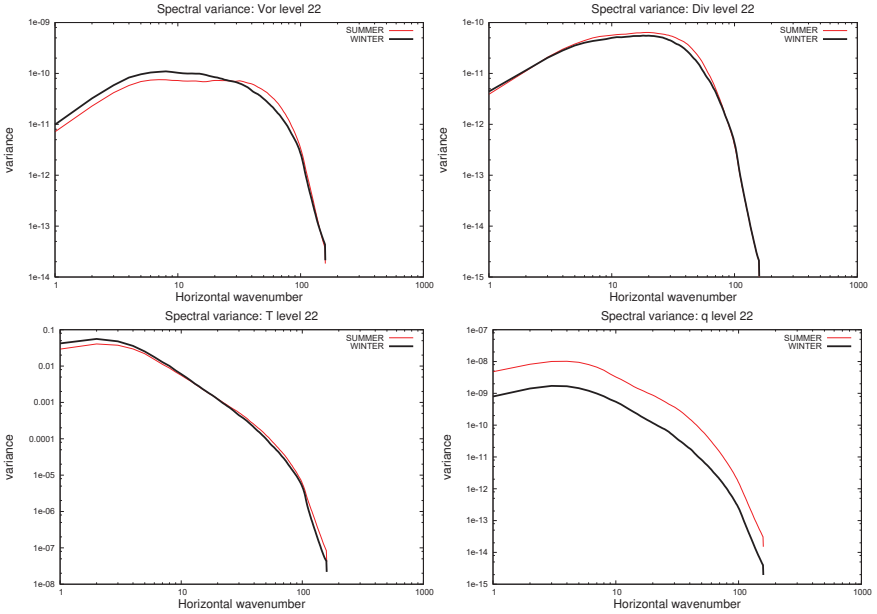

Figure 4.1: Variance spectra at ≈ 500 hPa (model level 22) comparing experiments **SUMMER** and **WINTER**. Top left: vorticity (s^{-2}), Top right: divergence (s^{-2}), Bottom left: temperature (K^2), Bottom right: specific humidity ($g^2\ kg^{-2}$)

vorticity and temperature there is a small decrease of variance for the sumer period in the large spatial scales. A physical explanation for the increased small scale error variance in summer can be, that the increased convective activity in this season might increase the background forecast uncertainty on the small spatial scales. It is not straightforward to explain the reduced large scale error variance of vorticity and temperature for the summer period, however it suggests that large scale processes with the size of anticyclones, cyclones and fronts might be forecasted more certainly in summer.

Horizontally averaged background error standard deviation profiles are plotted in Fig.4.3.

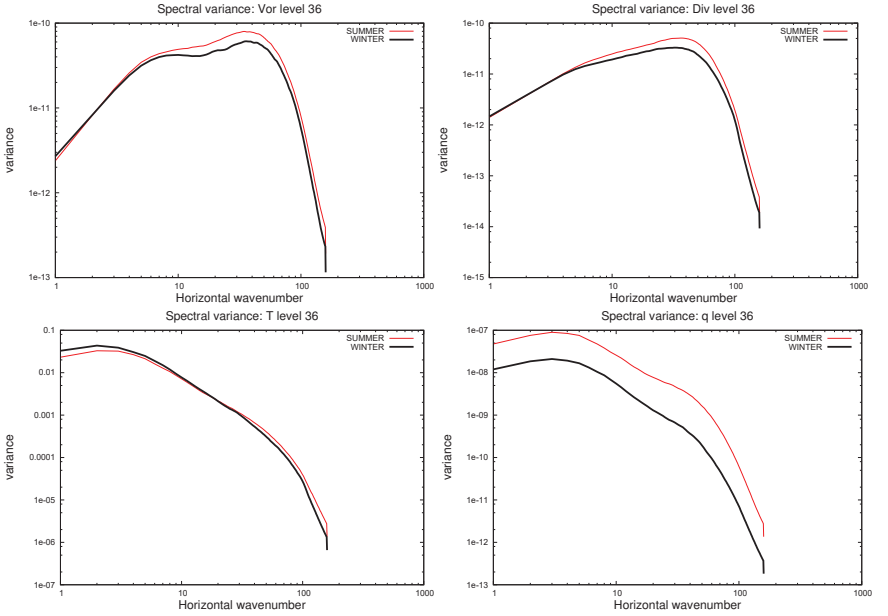

Figure 4.2: Variance spectra at ≈ 850 hPa (model level 36) comparing experiments **SUMMER** and **WINTER**. Top left: vorticity (s^{-2}), Top right: divergence (s^{-2}), Bottom left: temperature (K^2), Bottom right: specific humidity ($g^2\ kg^{-2}$)

They show, that the background forecast uncertainty is increased in summer compared to winter for all the variables and almost all heights. This is probably due to the increased occurrence of small scale processes (such as convection) in summer, which are less predictable by the model.

Vertical profiles of background error correlation length-scales are plotted in Fig.4.4. It appears that error correlation length-scales of the summer period are smaller for all the variables and for almost all heights. With other words, horizontal correlations are sharper for the summer period. This finding can be probably explained again by the convective activity in summer, which clearly implies more small scale structures in horizontal compared to the usual winter weather regime. It is interesting to see that background error correlations of temperature in the PBL (below level 42) are more widespread in summer than in winter. It is a rather surprising finding, and it might demonstrate that low level cloud situations, which would imply large temperature error correlation length-scales in the PBL, are not reflected in the winter statistics. This may come from the fact that the ALADIN model could not predict well low level inversions reinforced by low level clouds in any members of the forecasts downscaling the EnVar system.

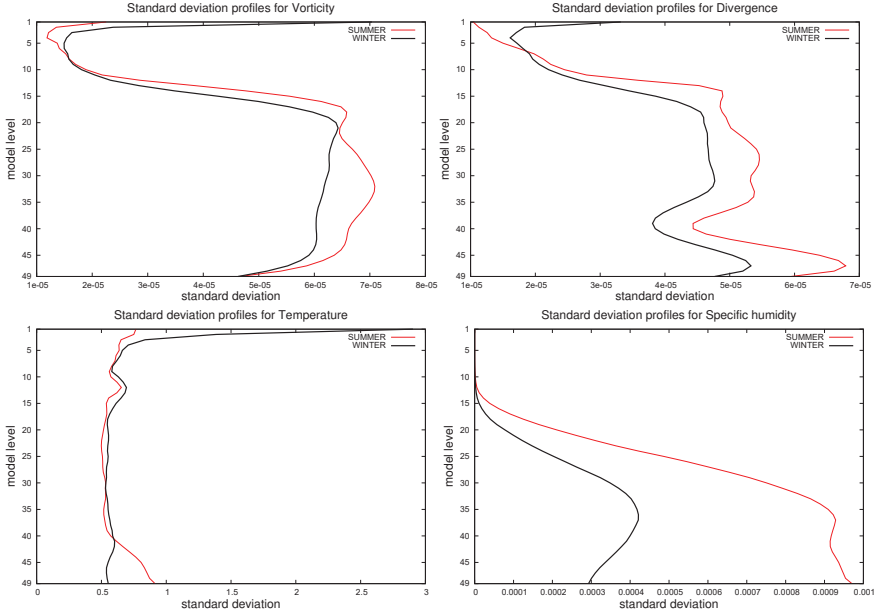

Figure 4.3: Standard deviation profiles deduced from experiment **WINTER** (black) and **SUMMER** (red). Top left: vorticity (s^{-1}), Top right: divergence (s^{-1}), Bottom left: temperature (K), Bottom right: specific humidity ($g\ kg^{-1}$)

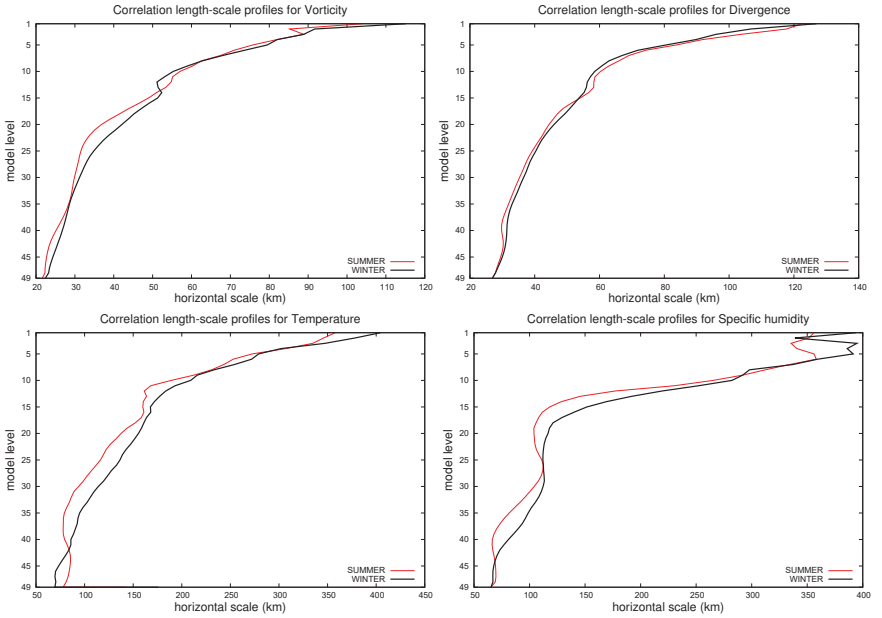

Figure 4.4: Correlation length-scale profiles deduced from the experiments **SUMMER** and **WINTER**. Top left: vorticity, Top right: divergence, Bottom left: temperature, Bottom right: specific humidity.

4.1.2 Impact of representing seasonal variability in the background errors

To assess, how much the representation of seasonal variability of background errors influence the quality of the analysis and the short range forecasts, two assimilation and forecast experiments were compared for the period of July 2007. Experiment **BT08** included an assimilation cycle using a background error covariance matrix based on experiment **SUMMER** (sampling over July 2008), while experiment **BT09** consisted of an assimilation cycle using background error covariances based on experiment **WINTER** (sampling over January 2009) period. Upon both assimilation cycles, series of 2 day forecasts were run and verified against surface and radiosonde observations. Screen level RMSE and BIAS scores are plotted in Fig.4.5-4.6. For the RMSE scores, a strong impact at analysis time can be seen pulling the analysis closer to the observations for experiment **BT08**, i.e. when the intuitively more appropriate summer statistics are used. However, for the 12 hour forecast range and above it, the impact is more or less lost or even turns into negative for experiment **BT08**. The BIAS scores at screen level show rather clear improvement for experiment **BT08**, except for 10m wind speed for the second day. In the upper air, RMSE scores are rather neutral between the two experiments, except

for relative humidity at 700 hPa, where the analysis of experiment **BT08** fits better the observations but longer forecast ranges show a degradation compared to experiment **BT09** (Fig.4.7). This feature of good fit to observations at analysis time but degradation for longer forecast ranges (also found at screen level) is probably due to the increased standard deviations in the **SUMMER** background errors, namely by giving more trust to observations in the analysis compared to the **WINTER** background errors. The fact that the fit to observation for longer forecast ranges is gone, may show, that the initial fit might be too strong, harming some balance properties, which deteriorate the forecast. The upper air BIAS scores show a mixed impact for the use of summer or winter statistics (Fig.4.8). Namely, geopotential at 500 hPa and temperature at 850 hPa is improved, while wind speed at 500 hPa and relative humidity at 700 hPa is degraded if using the summer background error statistics.

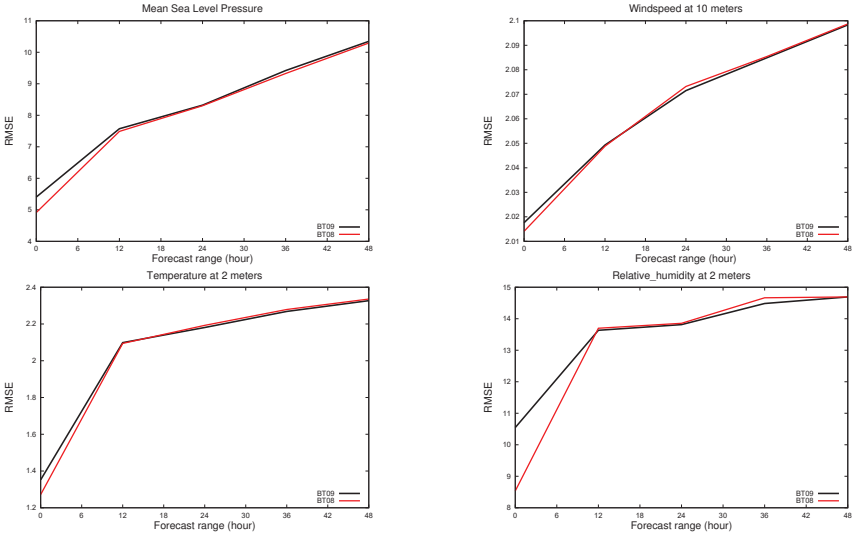

Figure 4.5: Screen level RMSE scores of experiments **BT09** (black) and **BT08** (red) for the 00 and 12 UTC runs together. Top left: mean sea level pressure (hPa), Top right: wind speed at 10m ($m\ s^{-1}$), Bottom left: temperature at 2m (K), Bottom right: relative humidity at 2m ($\%$). The scores are computed a against surface and radiosonde observations. Period: July 2007

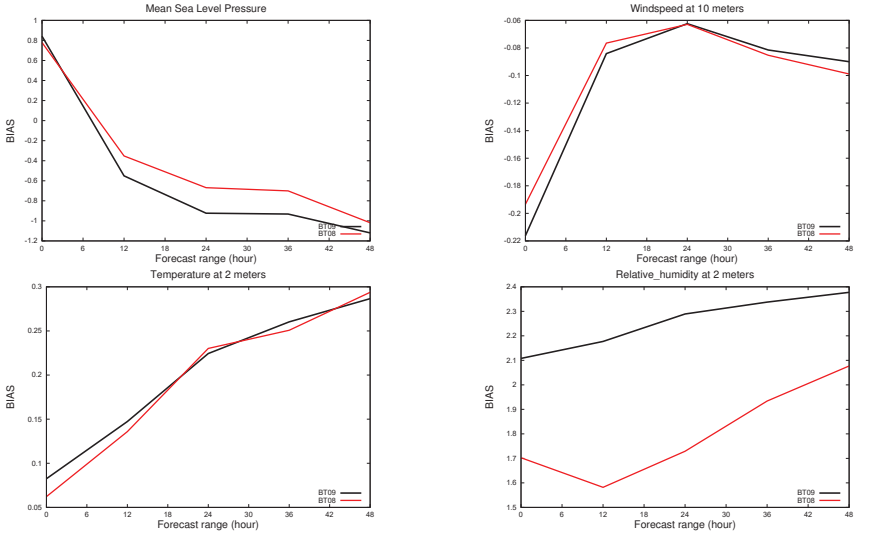

Figure 4.6: Same as Fig.4.5 but for BIAS.

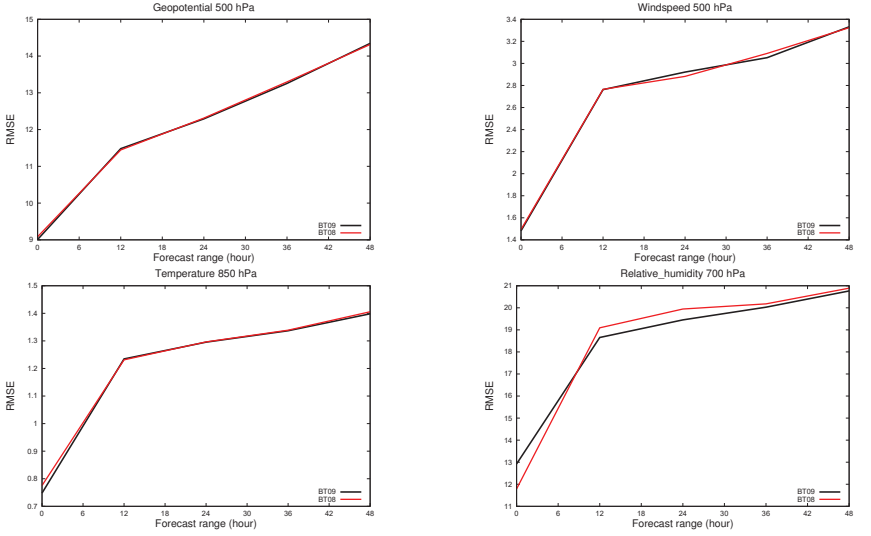

Figure 4.7: Upper air RMSE scores of experiments **BT09** (black) and **BT08** (red) for the 00 and 12 UTC runs together. The scores are computed against surface and radiosonde observations. Period: July 2007 (see figures 3.31 - 3.32 for units).

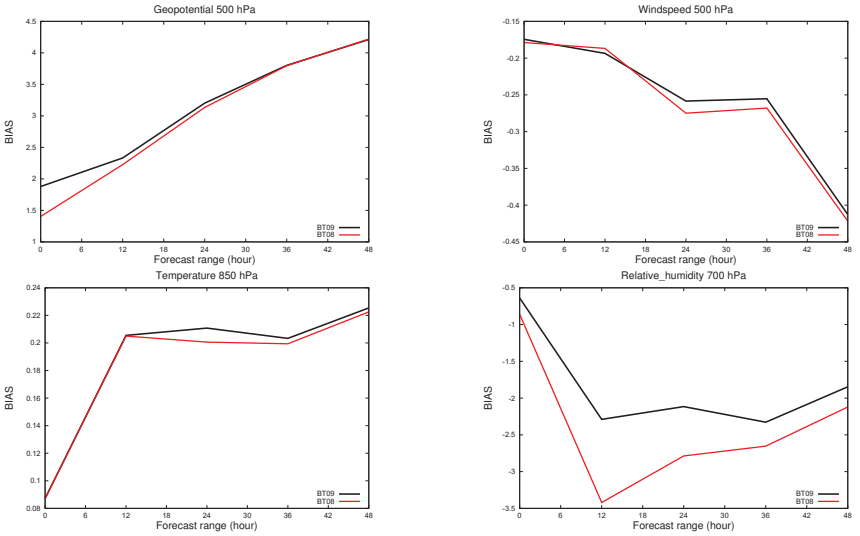

Figure 4.8: Upper air BIAS scores of experiments **BT09** (black) and **BT08** (red) for the 00 and 12 UTC runs together. The scores are computed against surface and radiosonde observations. Period: July 2007 (see figures 3.31 - 3.32 for units).

4.2 Diurnal variability

The diurnal variability of background errors was examined by comparing background error statistics based on forecast differences valid at night (00 UTC) and at day-time (12 UTC). Both simulation experiments were based on the LAM Ensemble Assimilation technique with local perturbations (i.e. like experiment **LAM EDA** in the previous chapter), driven by LBCs from the ECMWF EDA system over the period of July 2007. The error simulation experiment of night-time background errors will be referred as **00UTC**, while the one for the day-time background errors will be called **12UTC**. These latter are the same background error statistics presented in the previous chapter as experiment **LAM EDA**.

4.2.1 Diagnostic comparison of night- and day-time background error statistics

Figures 4.9 and 4.10 show spectra of background error variances at 500 hPa (model level 22) and at 850 hPa (model level 36) respectively. Comparing the two figures, it is sensible that the night- and

day-time background errors differ mostly in the PBL, which is a rather logical consequence of the different radiation balances at night and day near the surface. At 850 hPa, the variance is increased on the small scales in the day-time background errors. This reflects that the unstable PBL relevant at day-time is less predictable than at night, when the boundary layer is typically more stable. Explained differently, it is again the uncertainty in the prediction of convection, which might be responsible for the increase of small scale variance in the day-time background errors.

In the profiles of horizontally averaged standard deviations (Fig.4.11) there is an increase for

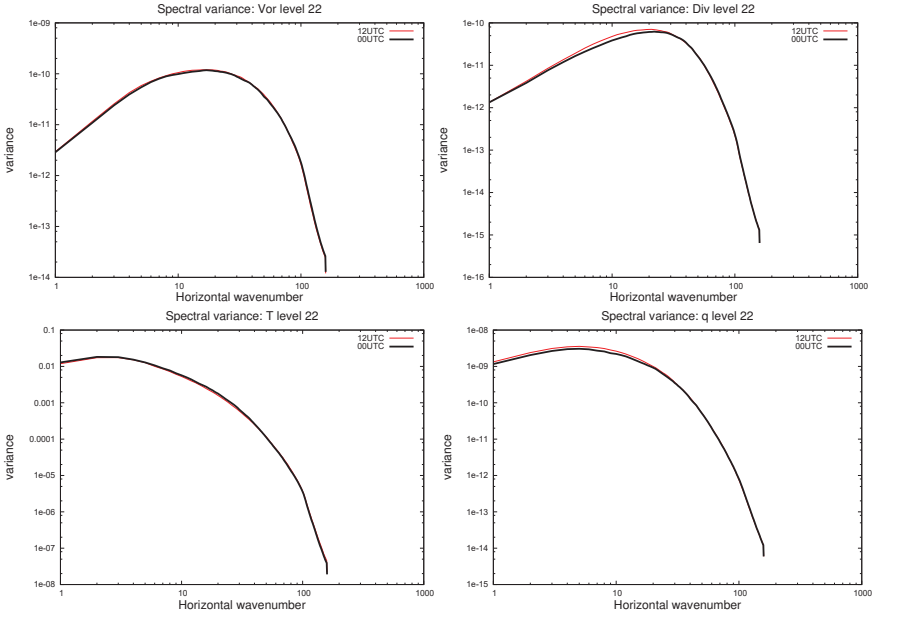

Figure 4.9: Variance spectra at ≈ 500 hPa (model level 22) comparing experiments **LAM EDA 00** and **LAM EDA 12**. Top left: vorticity (s^{-2}), Top right: divergence (s^{-2}), Bottom left: temperature (K^2), Bottom right: specific humidity ($g^2\ kg^{-2}$)

the day-time background errors for temperature and divergence compared to night-time, especially in the PBL. On the other hand, for vorticity, the standard deviation profiles are rather similar for the two experiments and for specific humidity there is a decrease of standard deviation for the day-time background errors near the surface. The increase of temperature and divergence standard deviations in the PBL supports the earlier finding that the presence of convection at day-time introduces some

uncertainty to the forecasts. This seems to be the most important difference in the background errors of night- and day-times. The decrease of humidity standard deviation near the surface at day-time compared to night-time shows that humidity forecasts valid at day-time are more certain as far as the sensitivity to the initial conditions is concerned. This is rather interesting finding and so far no physical interpretation is found for it.

Profiles of horizontal correlation length-scales are plotted in Fig.4.12. These diagnostics

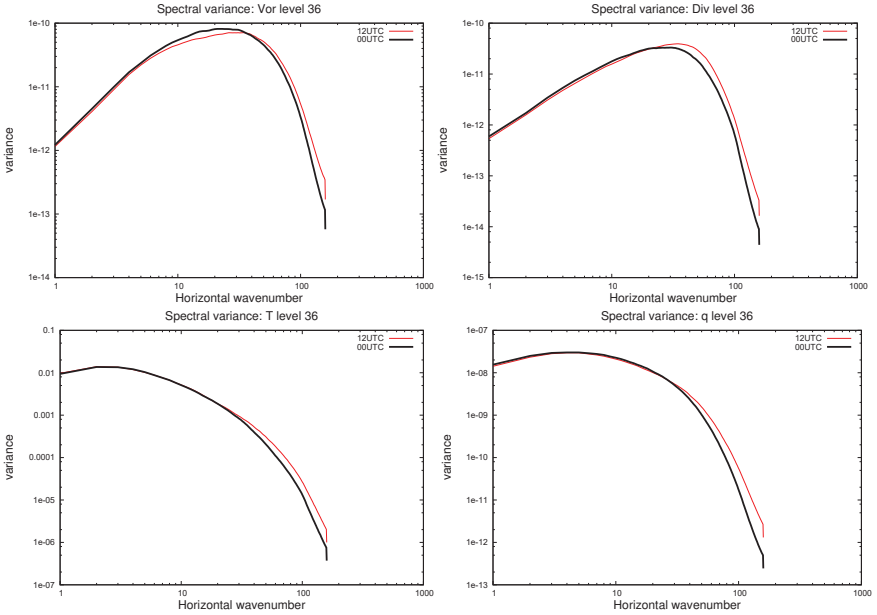

Figure 4.10: Variance spectra at ≈ 850 hPa (model level 36) comparing experiments **LAM EDA 00** and **LAM EDA 12**. Top left: vorticity (s^{-2}), Top right: divergence (s^{-2}), Bottom left: temperature (K^2), Bottom right: specific humidity ($g^2\ kg^{-2}$)

show rather clearly that horizontal background error correlation length-scales are shorter during the day, especially in the PBL (below 700 hPa). This means that meteorological processes with smaller horizontal characteristic size might be present in a higher amount during the day than during the night. This is indeed valid considering the appearance of small scale convective cells at day-time. The length-scales for temperature very near the ground however are larger at day-time than at night. More exactly, the temperature correlation length-scales at night are drastically reduced below ≈ 1000

hPa, so that they become smaller than those at day-time. A possible explanation is that, at night, the horizontal distribution of temperature very close to the surface is mainly determined by the different radiation balances of different soil surfaces (grass, forest, etc.), which might be of smaller scale than those determined by the turbulent mixing at day time.

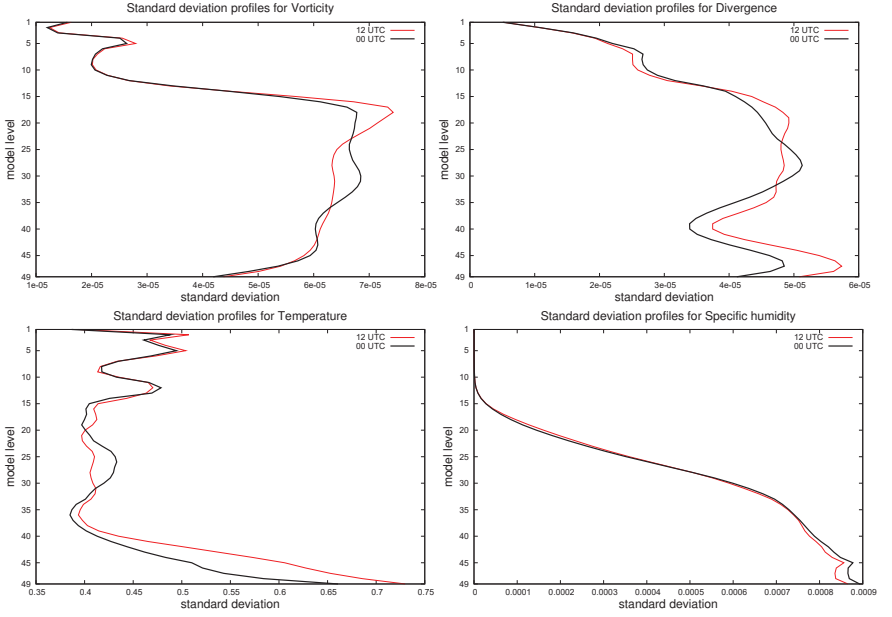

Figure 4.11: Standard deviation profiles deduced from experiment **LAM EDA 00** (black) and **LAM EDA 12** (red). Top left: vorticity (s^{-1}), Top right: divergence (s^{-1}), Bottom left: temperature (K), Bottom right: specific humidity ($g\ kg^{-1}$)

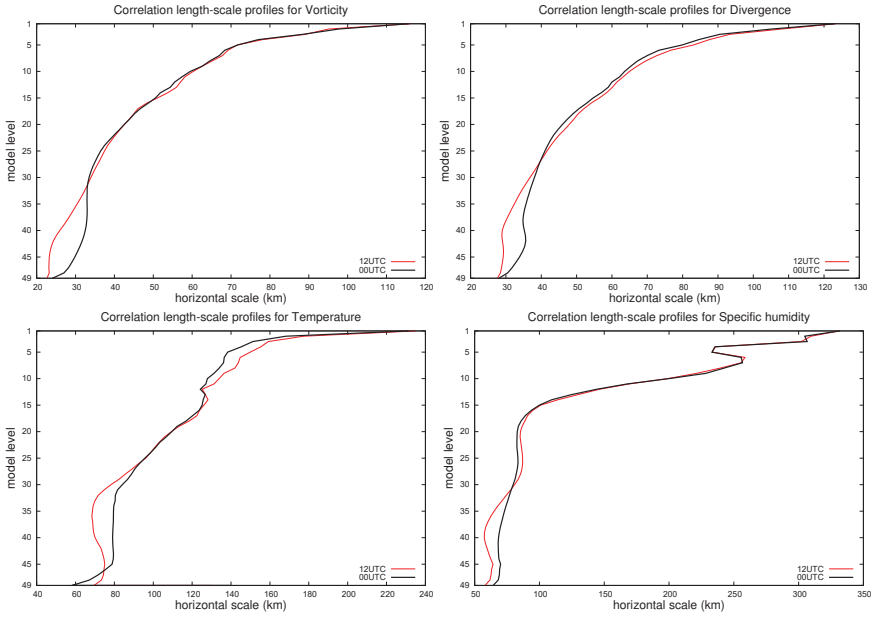

Figure 4.12: Correlation length-scale profiles deduced from the experiments **LAM EDA 00** and **LAM EDA 12**. Top left: vorticity, Top right: divergence, Bottom left: temperature, Bottom right: specific humidity.

4.2.2 Impact of representing diurnal variability in the background errors

The impact of representing the diurnal variability of background errors was assessed by running two assimilation and forecast experiments for the period of July 2007 with the following settings. In experiment **BT01** (already shown in chapter 3 in comparison with experiment **BT00**), the **00UTC** background error covariance matrix was used at 00 and 06 UTC analysis times and the **12UTC** background error covariance matrix was used at 12 and 18 UTC analysis times. On the other hand, in experiment **BT07** the **00UTC** background error covariances were used at all analysis times (00, 06, 12, 18 UTC). The goal with this experiment setup was to see what impact it makes in terms of scores if suppressing the diurnal differentiation in background errors used in the assimilation. Note, that given the fact that a summer test period was chosen, 00 and 06 UTC analysis times were considered to include "night-time PBL" properties, while 12 and 18 UTC analysis times were considered to be relevant for "day-time PBL". Figures 4.13-4.14 show screen level RMSE and BIAS scores respec-

tively comparing experiments **BT01** and **BT07**. The screen level RMSE scores show an improvement for experiment **BT01** for the second day forecast for mean sea level pressure, wind and temperature, while scores for the first day are rather neutral. A slight degradation in the 2m relative humidity RMSE scores of experiment **BT01** compared to **BT07** is also found. Screen level BIAS scores are

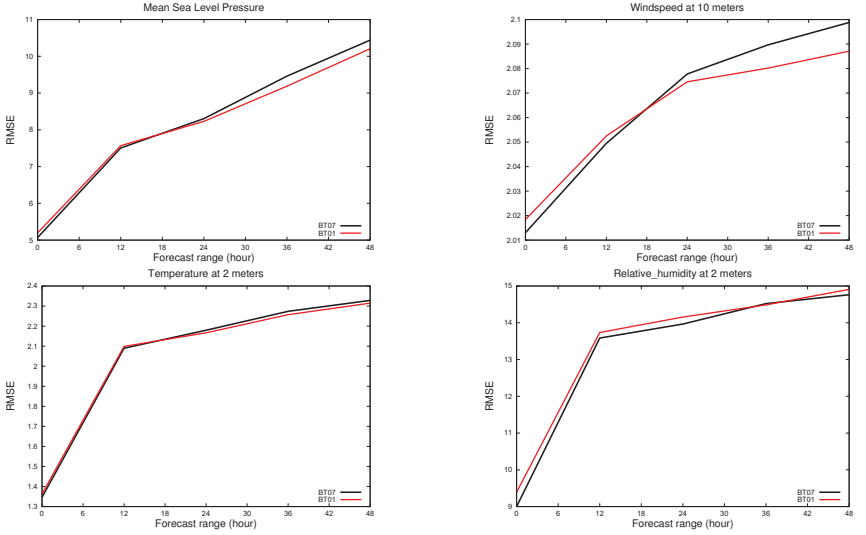

Figure 4.13: Screen level RMSE scores of experiments **BT07** (black) and **BT01** (red) for the 00 and 12 UTC runs together. Top left: mean sea level pressure (hPa), Top right: wind speed at 10m ($m\ s^{-1}$), Bottom left: temperature at 2m (K), Bottom right: relative humidity at 2m ($\%$). The scores are computed against surface and radiosonde observations. Period: July 2007

better for experiment **BT07**. This proves that the improvements of experiment **BT01** in RMSE for the second day are mainly due to the reduction in standard deviation, but not due to the reduction of systematic errors. The upper air RMSE scores are rather neutral, however a small improvement for the second day for experiment **BT01** can be noticed especially for geopotential at 500 hPa and relative humidity at 700 hPa (Fig.4.15). For these two parameters, the BIAS scores are also improved (Fig.4.16). Upper air wind BIAS (at 500 hPa) is better for experiment **BT07**, while temperature at 850 hPa is rather neutral.

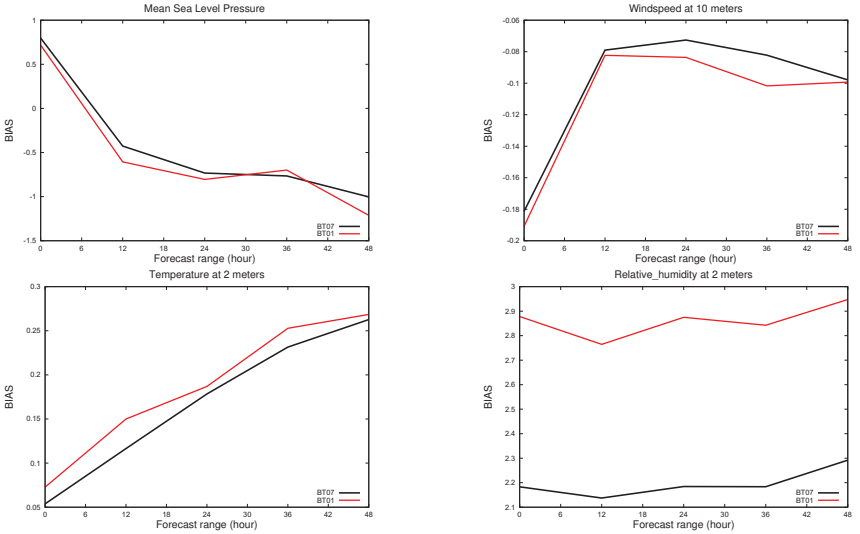

Figure 4.14: Same as Fig.4.13 but for BIAS.

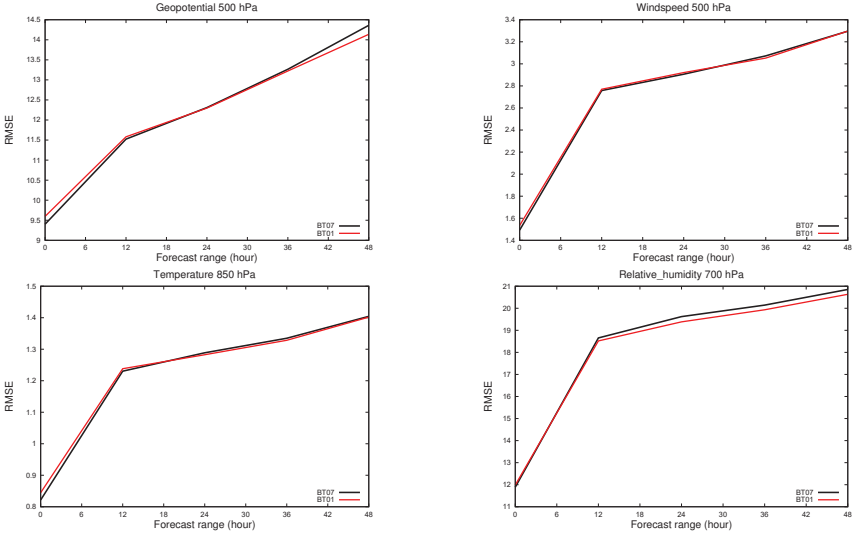

Figure 4.15: Upper air RMSE scores of experiments **BT07** (black) and **BT01** (red) for the 00 and 12 UTC runs together. The scores are computed against surface and radiosonde observations. Period: July 2007 (see figures 3.31 - 3.32 for units).

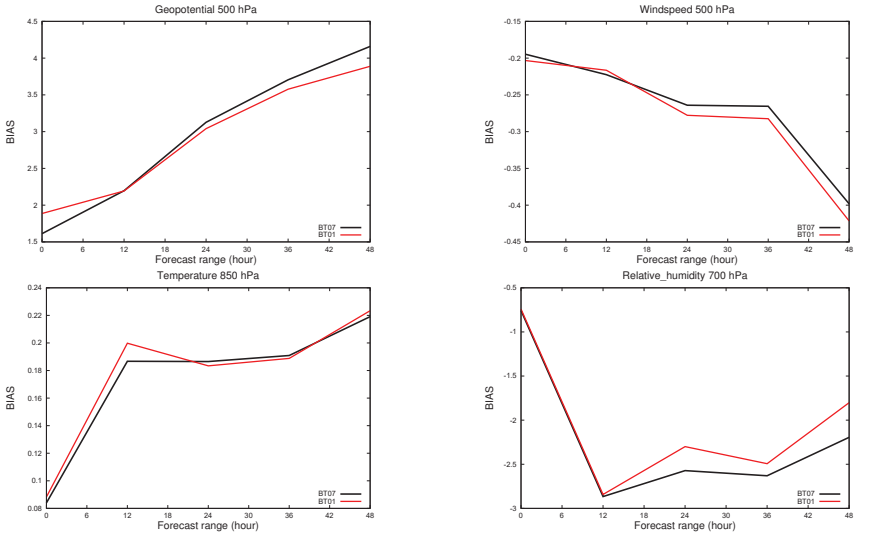

Figure 4.16: Upper air BIAS scores of experiments **BT07** (black) and **BT01** (red) for the 00 and 12 UTC runs together. Top left: Geopotential at 500 hPa ($m^2\ s^{-2}$), Top right: wind speed at 500 hPa ($m\ s^{-1}$), Bottom left: temperature at 850 hPa (K), Bottom right: relative humidity at 700 hPa ($\%$). The scores are computed against surface and radiosonde observations. Period: July 2007

4.3 Discussion

The experiments shown in this chapter indicate that both the seasonal and diurnal variabilities of background errors are important. It was found that the background uncertainty (error variances and standard deviations) is larger in summer than in winter. As far as the diurnal variability is concerned, it was shown that background errors valid at day-time are larger than those valid at night for most of the variables, which indicates a lower predictability during day-time. Horizontal background error correlation length-scales are smaller in summer than in winter, while the diurnal change shows smaller length-scales during the day than during the night. Both the seasonal and diurnal variabilities are more intense in the lower troposphere (PBL) and on small spatial scales. This spatial structure of the variability can be related to the different weather regimes in different seasons and at different times of the day. Namely, convection is the most probable process that determines both the seasonal and diurnal variabilities in the above experiments. The more intense presence of convection during summer (compared to winter) and at day-time (compared to night-time) might indeed increase the background error variance (and standard deviation) due to the lower predictability of small scale

convective events compared to situations with front passings and cyclogenesis. Also, the presence of convection might decrease the horizontal background error correlation length-scales by including processes of small horizontal size (convective cells).

As far as the impact on the forecast quality is concerned, the seasonal variability of background errors turned out to be rather neutral in terms of screen level RMSE. On the other hand, screen level BIAS is improved if a background error covariance matrix is used which is sampled for the actual season. The representation of diurnal variability of background errors makes a rather mixed impact on the forecast quality. Namely if the diurnal variability is taken into account through the used background error covariance matrix, the forecast quality slightly improves for the second day near the surface in terms of RMSE but it slightly degrades according to BIAS scores. In the upper air, the forecast of most of the parameters is neutral to the representation of diurnal background error variability, however relative humidity is remarkably improved.

Chapter 5

A posteriori diagnosis and tuning of background errors

The content of this chapter has been published in Időjárás, the quarterly journal of the Hungarian Meteorological Service ([9] *Bölöni and Horvath* 2010). The format has been slightly modified in order to fit the thesis.

A very important source of information in data assimilation is the background, which is usually a short-range forecast of the numerical weather prediction (NWP) model valid at the assimilation time. The background is corrected by the atmospheric observations providing the analysis during the process of data assimilation. Errors of the background are estimated statistically and are taken into account with the aim of giving a proper weight to the background field, as well as to the observations implicitly. Although, in theory, the background errors can be defined as the difference between the truth and the background, it is a great challenge to generate appropriate background error samples in practice for the computation of the background error statistics, because the true state is always unknown. A possible way to improve the background error representation is the development of the background sampling methods themselves (chapter 3 and 4). Another complementary approach is the "a posteriori" diagnosis or tuning of the already predefined background error statistics by a certain sampling technique. This paper presents two attempts for such a tuning within the ALADIN limited area model (LAM) and its 3DVAR assimilation system used operationally at the Hungarian Meteorological Service (HMS). The first one is based on the comparison of the predefined statistics with those expected in a statistically optimal assimilation system. The second one is inspired by single observation experiments and it addresses the improvement of the multivariate statistical balance between humidity and the other analyzed variables.

Data assimilation methods based on statistical optimality ([29] *Gandin* 1963, [47] *Lorenc* 1986, [61] *Thépaut and Courtier* 1991, [5] *Bouttier and Courtier* 1999) take into account the error of each available information type for weighting their contribution to the analysis $\mathbf{x}_a$, i.e., the initial condition

for the forecast. This is done by solving the so-called BLUE (Best Linear Unbiased Estimation) analysis equation:

$$\mathbf{x}_a = \mathbf{x}_b + \mathbf{B}\mathbf{H}^T(\mathbf{H}\mathbf{B}\mathbf{H}^T + \mathbf{R})^{-1}(\mathbf{y} - H\mathbf{x}_b) \tag{5.1}$$

Main available information are the atmospheric observations $\mathbf{y}$ and the background $\mathbf{x}_b$, which is usually a short-range forecast of the NWP model. The notation H stands for the so-called non-linear observation operator, which projects from the space of the model variables to that of the observed variables. The operator $\mathbf{H}$ is the linearized of H. The matrices $\mathbf{B} = E[\boldsymbol{\epsilon}_b, \boldsymbol{\epsilon}_b{}^T]$ and $\mathbf{R} = E[\boldsymbol{\epsilon}_o, \boldsymbol{\epsilon}_o{}^T]$ denote the background and observation error covariance matrices respectively, where E stands for the statistical expectation. The corresponding errors are defined as the difference from the true state of the atmosphere $\mathbf{x}_t$, i.e., $\boldsymbol{\epsilon}_b = \mathbf{x}_b - \mathbf{x}_t$ can be written for the background errors and $\boldsymbol{\epsilon}_o = \mathbf{y} - H\mathbf{x}_t$ for the observation errors. In the lack of $\mathbf{x}_t$ the sampling of these errors is a real challenge in the field of data assimilation. For the sampling of background errors, many ideas have been developed, like the method of innovations ([36] *Hollingsworth and Lönnberg* 1986, [48] *Lönnberg and Hollingsworth* 1986) or the NMC ([51] *Parrish and Derber* 1992) and Ensemble ([28] *Fisher* 2003, [3] *Belo Pereira and Berre* 2006, [58] *Stefanescu et al.* 2006) methods. Also attempts have been taken to characterize LAM specific background errors with the lagged-NMC approach ([57] *Siroká et al.* 2003). With the application of the above sampling techniques the representation of the background errors has been improved in some aspects indeed. In this paper, however, we would like to point out, that as $\mathbf{x}_t$ is never known, it is impossible to compute perfect B and R matrices with any method, and it is always reasonable to tune certain elements of the predefined covariance matrices "a posteriori". We will concentrate on the tuning of the B matrix statistics primarily, which was applied to the 3DVAR system of the ALADIN model ([39] *Horányi et al.* 1996) in our experiments. In Section 5.1 we describe a tuning experiment aiming to improve the background error variances based on statistical optimality criteria of analysis residuals. In Section 5.2 we show a tuning to improve the multivariate balance in the analysis based on the simplification of the analysis equation (5.1), and single observation tests.

5.1 Diagnosis and tuning based on the covariance of residuals in observation space

Based on the optimal estimation theory, several approaches exist for "a posteriori" validation and tuning. A technique applied earlier in ARPEGE/ALADIN was based on the assumption that the expected value of the variational cost function J at the minimum is proportional to the number of observations used, i.e., $E[J_{min}] = p/2$ hold, where p is the number of observations used in the

analysis ([60] *Talagrand* 1998, [23] *Désroziers and Ivanov* 2001, [16] *Chapnik et al.* 2004, [56] *Sadiki and Fischer* 2005, [26] *Fischer et al.* 2005). Another method was proposed by [22] *Désroziers et al.* (2006) later on, which is the theoretical basis for the tuning described in this chapter. It is explained in the above-mentioned paper that in a linear analysis system, where the B background and the R observation error covariance matrices are properly estimated, the following equations hold:

$$E[\mathbf{d}_b^o \mathbf{d}_b^{oT}] = \mathbf{H}\mathbf{B}\mathbf{H}^T + \mathbf{R} \tag{5.2}$$

$$E[\mathbf{d}_b^a \mathbf{d}_b^{oT}] = \mathbf{H}\mathbf{B}\mathbf{H}^T \tag{5.3}$$

$$E[\mathbf{d}_a^o \mathbf{d}_b^{oT}] = \mathbf{R} \tag{5.4}$$

$$E[\mathbf{d}_b^a \mathbf{d}_a^{oT}] = \mathbf{H}\mathbf{A}\mathbf{H}^T \tag{5.5}$$

where

$$\mathbf{d}_b^o = \mathbf{y} - H\mathbf{x}_b \tag{5.6}$$

$$\mathbf{d}_b^a = H\mathbf{x}_a - H\mathbf{x}_b \tag{5.7}$$

$$\mathbf{d}_a^o = \mathbf{y} - H\mathbf{x}_a \tag{5.8}$$

are residuals of the model and the observations provided by the assimilation system. The notation $\mathbf{A}$ in equation (5.5) stands for the analysis error covariance matrix. The optimality of the analysis system can be diagnosed if one computes the covariances of residuals on the left-hand side and substitutes the predefined error statistics to the right-hand side of equations (5.2-5.5). The residuals on the left-hand side can be easily obtained as a by-product of the assimilation system. The equations (5.3) and (5.4) can be applied for instance for the diagnosis of the background and observation error standard deviations:

$$\sigma_{bd} = \sqrt{\frac{1}{P}\sum_{i=1}^{P} d_{bi}^a d_{bi}^o} \qquad \sigma_{od} = \sqrt{\frac{1}{P}\sum_{i=1}^{P} d_{ai}^o d_{bi}^o} \tag{5.9}$$

where d_{bi}^a, d_{ai}^o and d_{bi}^o stand for the individual i realizations of the background and analysis departures ($i = 1, ..., P$). Then the misfit of the predefined standard deviations (σ_{bp} and σ_{op}) can be obtained as follows:

$$r_b = \frac{\sigma_{bd}}{\sigma_{bp}} \qquad r_o = \frac{\sigma_{od}}{\sigma_{op}} \tag{5.10}$$

These misfit ratios can be used as guidance for tuning the predefined standard deviations in the assimilation system. One has to notice, that through equation (5.1), the (5.6-5.8) residuals depend on (σ_{bp} and σ_{op}), which means that ideally the tuning with the misfit ratios and the computation of the analysis equation (5.1) should be done iteratively until r_b and r_o converge. It has also been shown by [22] *Désroziers et al.* (2006) in a simplified system, that the convergence can be reached in a few iterations.

5.1.1 Estimation of the misfit ratios in the analysis system

The above method was applied in the ALADIN 3DVAR system used at HMS ([8] *Bölöni* 2006) for the estimation of the misfit ratio for the background error standard deviations. The (5.6-5.8) residuals were taken from two assimilation cycles run over an autumn (October-November 2005) and a summer (June 2006) period. In these assimilation cycles all the available observations were included, which are used operationally in the ALADIN 3DVAR system at HMS ([55] *Randriamampianina* 2006). However, for the diagnosis of the background error standard deviations, only the residuals based on direct observations (i.e., radiosondes and aircrafts) were used. There was no iteration applied in the estimation for the sake of simplicity. In the fully spectral version of the ALADIN 3DVAR system, predefined background error standard deviations are uniform horizontally and variable in the vertical, so they are available as one value for each model level and analyzed meteorological variables (i.e., temperature (T), specific humidity (q), vorticity (ζ), divergence (η) ([10] *Berre* 2000). On the other hand, the diagnosed standard deviations can be obtained at the observation locations and for the observed quantities (T, q, and wind u, v components). In our estimation, a vertical averaging was applied both for the predefined and diagnosed values so that they became comparable independently from the height. For the comparison of predefined (ζ, η) and diagnosed (uv) wind error values, an average wind standard deviation ($\sigma_b(uv)$) was defined that can be computed as:

$$\sigma_{bd}(uv) = \sqrt{\frac{1}{2}\sigma_{bd}^2(u) + \sigma_{bd}^2(v)} \tag{5.11}$$

from the diagnosed u and v standard deviations values, and as:

$$\sigma_{bp}(uv) = \sqrt{-\frac{1}{2}\Delta^{-1}(\sigma_{bp}^2(\zeta) + \sigma_{bp}^2(\eta)} \tag{5.12}$$

from the predefined and standard deviations, where Δ denotes the Laplace operator, i.e., the second space derivative in horizontal. Table 5.1 shows the misfit ratios computed as explained above and also the predefined and diagnosed background error standard deviations both for the autumn and summer periods. Large misfit ratios for humidity suggest that the humidity background error standard

Variable	Predefined	Diagnosed (Autumn)	Misfit (Autumn)	Diagnosed (Summer)	Misfit (Summer)
q	$2.27 * 10^{-4}$	$5.34 * 10^{-4}$	2.35	$5.84 * 10^{-4}$	2.56
T	0.4917	0.7071	1.43	0.8010	1.62
Wind (u, v)	1.4840	1.9878	1.33	1.9203	1.29
Average	**0.65**	**0.89**	**1.36**	**0.9**	**1.38**

Table 5.1: Predefined and diagnosed background error standard deviations and the corresponding misfit ratios for specific humidity, temperature, wind and their average.

deviations are the less accurate as predefined by the original B matrix in our assimilation system. The misfit ratios are slightly different for the two different time periods, which suggests a possible seasonal dependence of the accuracy in the predefined background error modeling.

5.1.2 The tuning of background error standard deviations in an assimilation experiment

The analysis system can be tuned by multiplying the predefined standard deviations with the misfit ratios introduced in the previous section. In our experiments such tuning was done only for the background error standard deviations in two steps with different complexity. Experiment **ENS1** used a uniform misfit ratio for all the variables and vertical model levels. This means that the misfit ratio used was averaged over the vertical levels and over the variables q, T, and wind. Experiment **ENS2** used a variable dependent misfit ratio still averaged over the vertical levels. It is to be mentioned, that the predefined statistics were computed based on the Ensemble sampling method. Both the **ENS1** and **ENS2** tuning options were tested in real assimilation cycling experiments over the summer period. It means a 16-day assimilation cycle (64 analysis steps) using the operational observational dataset. Simulations of 48-hour production runs were started from 00:00 UTC after 2 days of warm up cycling. The impact of the tuning was measured through RMSE and BIAS score (see, e.g., [65] *Wilks* 1995) computations of the above-mentioned production forecasts against surface and radiosonde observations. The reference assimilation cycle for the tuning experiments (**ENS0**) was the same as **ENS1**

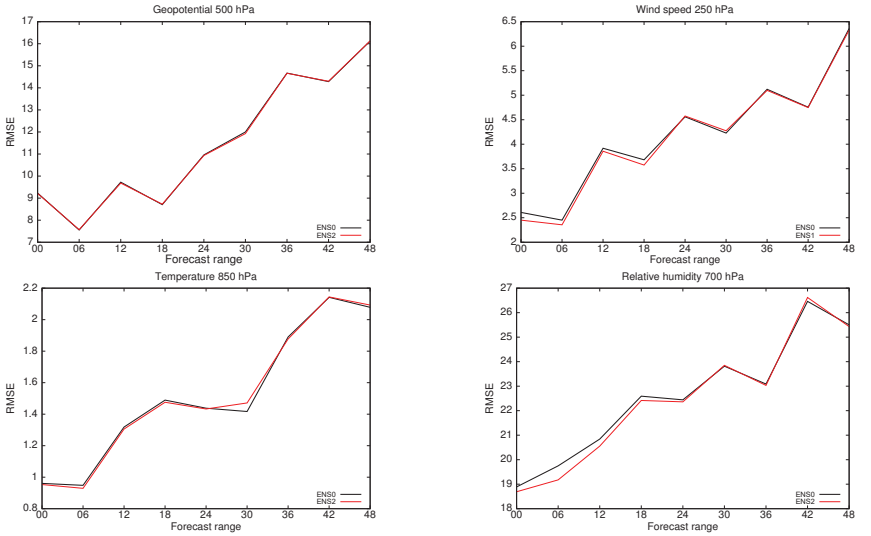

Figure 5.1: Upper air verification scores (RMSE) computed against observations over the period June 7-20, 2006. Red: experiment **ENS1**, Black: reference **ENS0**. Top left: geopotential at 500 hPa ($m^2\ s^{-2}$), Top right: wind speed at 250 hPa ($m\ s^{-1}$), Bottom left: temperature at 850 hPa (K), Bottom right: relative humidity at 700 hPa ($\%$).

and **ENS2**, except that no tuning of the background error standard deviations was applied, i.e., the predefined values were used. In experiment **ENS1**, a uniform misfit ratio, $r_b = 1.3$ was used as a multiplication factor to increase the predefined background error standard deviations. This value was chosen based on the average misfit ratios shown in Table 5.1. The verification results show that the **ENS1** tuning had no impact on the 2-meter parameters (not shown) but did improve the humidity forecasts on 700 hPa and the wind forecasts on 250 hPa (Fig.5.1). The impact on geopotential and temperature in the altitude was found to be rather neutral (Fig.5.1). In experiment **ENS2**, the misfit ratios computed from the autumn period were used. These are $r_b = 1.33$ for the wind and mass variables (vorticity, divergence, surface pressure, and geopotential), $r_b = 1.43$ for temperature, and $r_b = 2.35$ for humidity, as shown in Table 5.1. The tuning had no impact on the 2-meter fields (not shown). Results for the atmospheric variables are displayed in Fig.5.2. One can see that **ENS2** gives clearly worse results than the reference **ENS0** for temperature on 850 hPa and also somewhat for relative humidity on 700 hPa. There is a positive impact of the tuning for the wind on 250 hPa. Results show that the uniform tuning (**ENS1**) provides better results than the variable dependent one (**ENS2**), which looks curious, because in theory equations (5.9) hold for each variable separately as well.

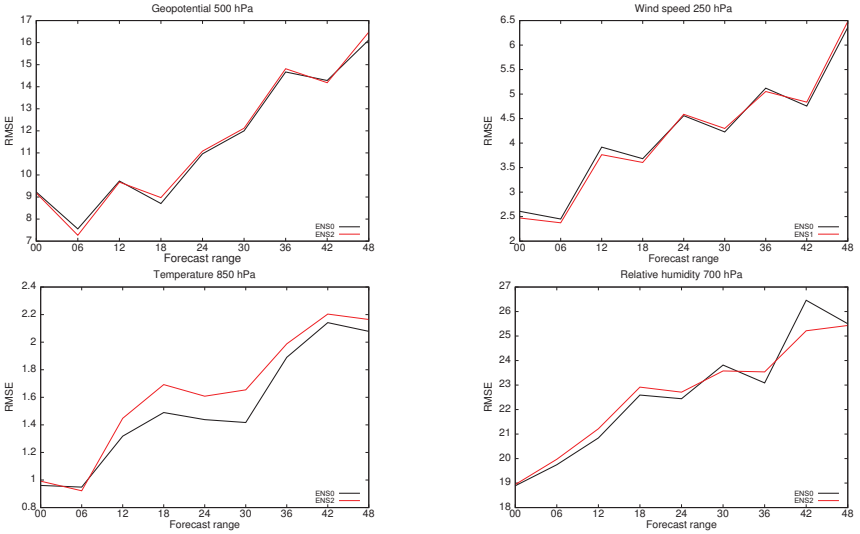

Figure 5.2: Upper air verification scores (RMSE) computed against observations over the period June 7-20, 2006. Red: experiment **ENS2**, Black: reference **ENS0**. Top left: geopotential at 500 hPa ($m^2\ s^{-2}$), Top right: wind speed at 250 hPa ($m\ s^{-1}$), Bottom left: temperature at 850 hPa (K), Bottom right: relative humidity at 700 hPa ($\%$).

In Fig.5.3 one can see the predefined and the tuned background error standard deviation profiles used in the experiments. It is obvious that the tuned profiles (**ENS1** and **ENS2**) are quite similar to each other for wind. The difference is larger for temperature, and it is the largest for humidity. This suggests that the disappointing results of experiment **ENS2** are mostly due to the large misfit ratios for humidity and temperature. A probable reason for the poorer result of the **ENS2** experiment is that the misfit is averaged in the vertical, which can lead to an exaggerated tuning on those levels where the real misfit is drastically smaller than the average.

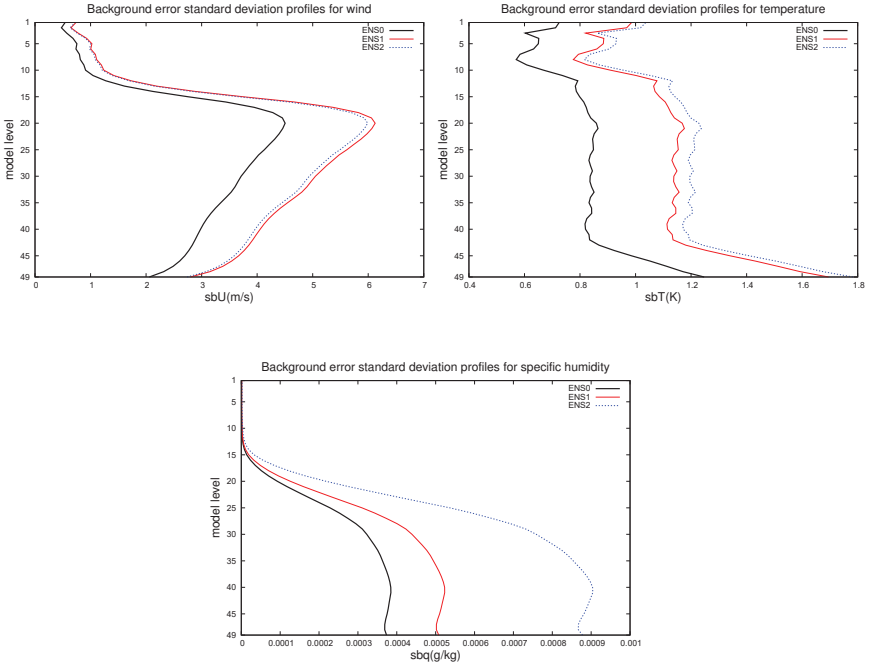

Figure 5.3: Predefined (**ENS0**) and tuned (**ENS1** and **ENS2**) profiles of total background error standard deviations. Top left: wind speed ($m\ s^{-1}$), Top right: temperature (K), Bottom: specific humidity ($g\ kg^{-1}$).

5.2 Diagnosis and tuning of the multivariate statistical balance

The ALADIN 3DVAR is a multivariate analysis system provided by the statistical balance described by [53] *Rabier et al.* (1998), [17] *Courtier et al.* (1998), [10] *Berre* (2000) and [35] *Gustafsson et al.* (2001). In short, this statistical balance couples the analyzed variables in a meteorologically mean-

ingful way by propagating a part of the increments of a given variable to those of another one. This ensures the dynamical balance of the variables in the analysis. Experiments done at HMS showed that temperature observations have a large impact on the relative humidity analysis, which results in degradation of the relative humidity analysis and forecast verification scores in some weather situations. On the other hand, the humidity observations influence the temperature analysis in a very limited extent. This asymmetry in the multivariate balance brought us to study the analysis equation in a simplified framework and to propose a tuning of the error variances for a more symmetric balance.

5.2.1 Theoretical considerations

It can be shown that in a single point model (i.e., $\mathbf{H} = \mathbf{I}$, where $\mathbf{I}$ is the identity matrix), restricting to two variables only (T: temperature and Rh: relative humidity), the analysis equation (5.1) can be written as:

$$\delta T = \frac{cov(\boldsymbol{\epsilon}_{b,T}, \boldsymbol{\epsilon}_{b,Rh})}{\sigma^2(\boldsymbol{\epsilon}_{b,Rh}) + \sigma^2(\boldsymbol{\epsilon}_{o,Rh})} \Delta Rh \tag{5.13}$$

where δ denotes the analysis increment (analysis minus background) and Δ stands for the observation increment or innovation (observation minus background). Based on [19] *Daley* (1991) and [37] *Hollingsworth* (1987), equation (5.13) can be decomposed as:

$$\delta Rh = \frac{\sigma^2(\boldsymbol{\epsilon}_{b,Rh})}{\sigma^2(\boldsymbol{\epsilon}_{b,Rh}) + \sigma^2(\boldsymbol{\epsilon}_{o,Rh})} \Delta Rh \tag{5.14}$$

$$\delta T = \frac{cov(\boldsymbol{\epsilon}_{b,T}, \boldsymbol{\epsilon}_{b,Rh})}{\sigma^2(\boldsymbol{\epsilon}_{b,Rh})} \delta Rh \tag{5.15}$$

where equation (5.14) stands for the univariate or filtering step, which provides humidity analysis increment from the humidity innovation and equation (5.15) represents the multivariate propagation step, which transforms the humidity analysis increment to temperature analysis increment. Multiplying and dividing the right-hand side of equation (5.15) with $\sigma(\boldsymbol{\epsilon}_{b,T})$ and using the definition of the correlation, (5.15) can be rewritten as:

$$\delta T = corr(\boldsymbol{\epsilon}_{b,T}, \boldsymbol{\epsilon}_{b,Rh}) \frac{\sigma(\boldsymbol{\epsilon}_{b,T})}{\sigma(\boldsymbol{\epsilon}_{b,Rh})} \delta Rh \tag{5.16}$$

In case of a temperature innovation, one can write the corresponding equations similarly to (5.14) and (5.15) as follows:

$$\delta T = \frac{\sigma^2(\boldsymbol{\epsilon}_{b,T})}{\sigma^2(\boldsymbol{\epsilon}_{b,T}) + \sigma^2(\boldsymbol{\epsilon}_{o,T})} \Delta T \tag{5.17}$$

$$\delta Rh = corr(\boldsymbol{\epsilon}_{b,T}, \boldsymbol{\epsilon}_{b,Rh}) \frac{\sigma(\boldsymbol{\epsilon}_{b,Rh})}{\sigma(\boldsymbol{\epsilon}_{b,T})} \delta T \tag{5.18}$$

The asymmetry in the multivariate propagation step can be quantified as the ratio of T and Rh analysis increments induced by T and Rh innovations:

$$S = \left(\frac{\delta Rh}{\delta T}\right)_{\Delta T} / \left(\frac{\delta T}{\delta Rh}\right)_{\Delta Rh} \tag{5.19}$$

The ratio S was computed within the ALADIN 3DVAR system using single observations ($\Delta T = 1K$ and $\Delta Rh = 2\%$), taking the analysis increments right at the origin point (Fig.5.4-5.7). Note that the single observation experiments were run using NMC background error statistics sampled from differences of 36- and 12-hour forecasts of the operational ALADIN model over the period May-July 2004. Substituting the analysis increments shown in Fig.5.4-5.7 into equation (5.19), $S \approx 3688$ was found. It is easier to interpret this value if one writes up (5.19) using the equations (5.16) and (5.18), which gives:

$$S = \left(\frac{\sigma(\boldsymbol{\epsilon}_{b,Rh})}{\sigma(\boldsymbol{\epsilon}_{b,T})}\right)^2 \approx 3688 \tag{5.20}$$

This shows that the symmetry of the multivariate coupling depends only on the variance ratios of the two variables. Taking the square root of the above equation one gets:

$$\sqrt{S} = \frac{\sigma(\boldsymbol{\epsilon}_{b,Rh})}{\sigma(\boldsymbol{\epsilon}_{b,T})} \approx 60\frac{\%}{K} \tag{5.21}$$

According to the above equation, a $1K$ temperature error is associated to a 60% error in relative humidity and vice versa, which points out the rather asymmetric behavior of the multivariate propagation steps taking into account typical changes of temperature and humidity in the troposphere. The proposal for the tuning is thus to decrease the above ratio of standard deviations, which can be done either by increasing $\sigma(\boldsymbol{\epsilon}_{b,T})$ or by decreasing $\sigma(\boldsymbol{\epsilon}_{b,Rh})$. Examining the univariate steps in case of the T (Fig.5.4) and Rh innovations (Fig.5.5), one can see that the Rh analysis increment is about the 80% of the Rh innovation, while the T analysis increment is about the 60% of the T innovation. This means that the trust in the humidity background is indeed very small, which was the basis for assuming that $\sigma(\boldsymbol{\epsilon}_{b,T})$ is well chosen and $\sigma(\boldsymbol{\epsilon}_{b,Rh})$ is overestimated. As a consequence, it was decided to run tuning experiments by reducing the humidity background error standard deviations. An additional remark is that beside reducing humidity background error standard deviations, we considered to reduce also the humidity observation error standard deviations in order to keep the univariate filtering step (equation (5.14)) unchanged. It should be clarified here, that the ALADIN 3DVAR uses specific humidity (q) instead of relative humidity as analysis control variable, which also implies that the $\sigma(\boldsymbol{\epsilon}_{b,q})$ specific humidity background error standard deviations were chosen for tuning instead of $\sigma(\boldsymbol{\epsilon}_{b,Rh})$. The reason for using Rh in the above elaboration was that the asymmetry of the multivariate balance was observed first in relative humidity scores, and also the reader might judge relative humidity changes in the atmosphere easier than those of specific humidity.

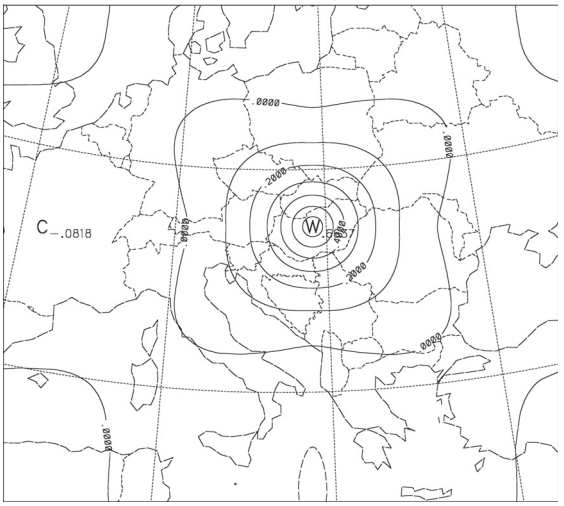

Figure 5.4: Temperature analysis increment induced by a temperature innovation ($\Delta T = 1K$, $\sigma(\epsilon_{o,Rh}) = 0.12\%$, $\sigma(\epsilon_{o,T}) = 1.1K$)

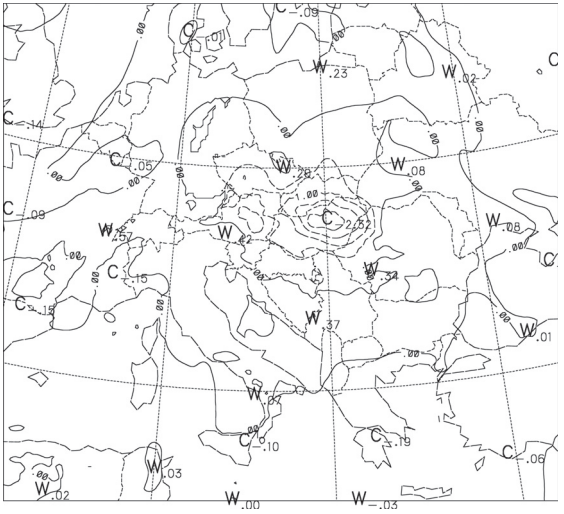

Figure 5.5: Relative humidity analysis increment induced by a temperature innovation ($\Delta T = 1K$, $\sigma(\epsilon_{o,Rh}) = 0.12\%$, $\sigma(\epsilon_{o,T}) = 1.1K$)

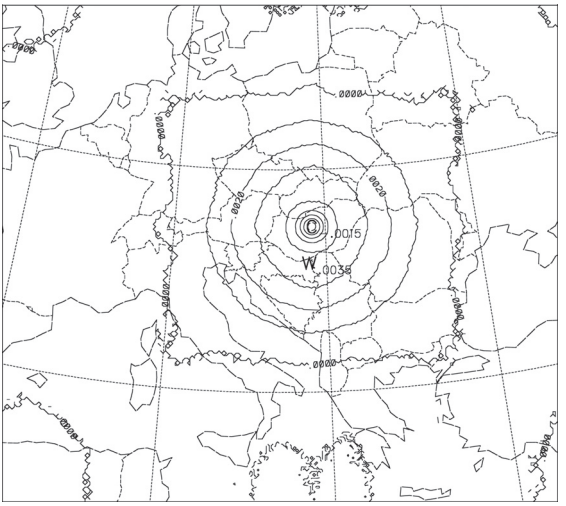

Figure 5.6: Temperature analysis increment induced by a relative humidity innovation ($\Delta Rh = 2\%$, $\sigma(\epsilon_{o,Rh}) = 0.12\%$, $\sigma(\epsilon_{o,T}) = 1.1K$)

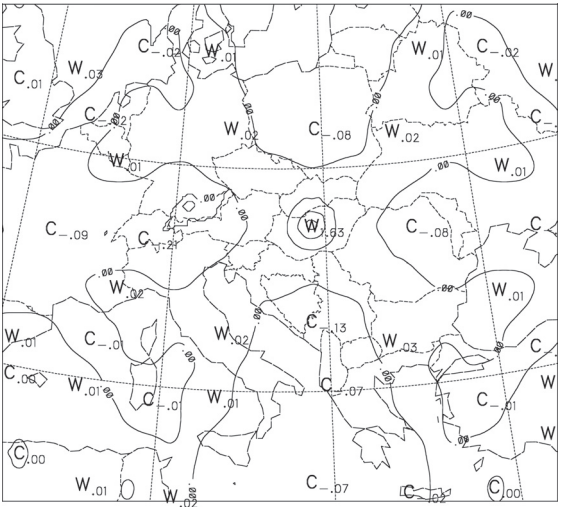

Figure 5.7: Relative humidity analysis increment induced by a relative humidity innovation ($\Delta Rh = 2\%$, $\sigma(\epsilon_{o,Rh}) = 0.12\%$, $\sigma(\epsilon_{o,T}) = 1.1K$)

Another feature that requires explanation here is that Rh single observation increments in Fig.5.5 and Fig.5.7 show some obvious anisotropy in spite of the fact that the ALADIN horizontal background error structure is designed to be isotropic by origin ([10] *Berre* 2000). The clue for this seeming contradiction is that the anisotropy is not included by the structure functions directly but rather by the computation Rh from q. Namely, to derive and plot relative humidity increments, first the $q \rightarrow Rh$ computation is performed both on the background and analysis fields, and then their difference is taken. As the $q \rightarrow Rh$ computation is a non-linear function of specific humidity and temperature, the resulting relative humidity increment will not keep the isotropic structure even if both specific humidity and temperature increments alone are isotropic.

5.2.2 The tuning of background and observation error standard deviations for humidity

The extent of reduction of humidity errors was determined on the basis of an error estimation proposed by [36] *Hollingsworth and Lönnberg* (1986) (HL method), which is independent from the NMC method. In short, the HL method estimates the observation and background errors based on the first equation of (5.2), where the innovations are composed by the difference of radiosonde observations and model forecasts. By sorting the innovations in vertical and horizontal distance categories, one can estimate a vertical profile of observation and background error standard deviations and horizontal correlation length-scales. This independent method was used as a guideline for estimating new background and observation standard deviations for humidity within our analysis system. The HL method was applied for the same period as the one used for the NMC sampling (May 2 - August 2, 2004). The HL standard deviations were first computed on the standard levels of the radiosonde observations, and then they were interpolated on the model levels for the comparison with the NMC statistics. In Fig.5.8 the ratio of HL and NMC background error standard deviations are shown for specific humidity. Levels under 850 hPa were not considered for the tuning due to the small amount of radiosonde observations. Despite the strong vertical variability, the ratio is smaller than 1 for all the vertical levels, which means that the HL estimation of $\sigma(\boldsymbol{\epsilon}_{b,q})$ is smaller than the NMC one in the whole troposphere. This is in accordance with the notion of $\sigma(\boldsymbol{\epsilon}_{b,q})$ being overestimated in the NMC statistics, which was also suggested by the theoretical considerations described earlier. Thus, it was decided to tune the $\sigma(\boldsymbol{\epsilon}_{b,q})$ and $\sigma(\boldsymbol{\epsilon}_{o,q})$ profiles used in the ALADIN 3DVAR experiments according to the ratio profile shown in Fig.5.8. Additionally, in some of the experiments $\sigma(\boldsymbol{\epsilon}_{b,q})$ was drastically reduced (multiplied by a factor of 0.005) above 250 hPa in order to prevent to propagate high altitude humidity increments to the lower troposphere. This latter modification was based on the experiences at ECMWF ([2] *Andersson et al.* 1998). The tuning experiments were run with the following three settings:

- Experiment **EX1Q**: modified $\sigma(\epsilon_{b,q})$ between 850 and 250 hPa according to the HL/NMC ratio, reduced $\sigma(\epsilon_{b,q})$ above 250 hPa.
- Experiment **EX2Q**: same as in **EX1Q** but also $\sigma(\epsilon_{o,q})$ is reduced in the same heights and in the same extent as $\sigma(\epsilon_{b,q})$.
- Experiment **EX3Q**: same as **EX2Q** except that there was no tuning applied above 250 hPa.
- Experiment **REFQ**: reference run using the predefined $\sigma(\epsilon_{b,q})$ and $\sigma(\epsilon_{o,q})$ values.

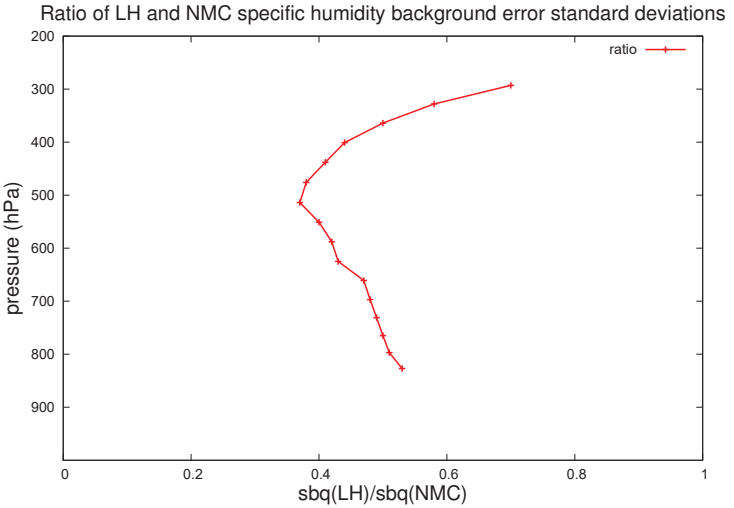

Figure 5.8: Vertical profile of specific humidity background error standard deviation ratios obtained by the HL and NMC methods.

As a first step, the computation of equation (5.19) was repeated with the tuned error standard deviations based on single observation experiments again. It was proven that the tuning indeed reduced the asymmetry in the expected way as was found with the **EX1Q** and was obtained with the **EX2Q** settings. As a second step, complete assimilation cycles were run for a two-week period (August 29-September 10, 2004) with all the above experimental settings in order to see the impact of the tuning in a real operational-like context. The assimilation cycles were run with a 6-hour frequency, using surface, radiosonde, aircraft, and satellite (ATOVS AMSU-A and B) observations. Production forecasts (up to 48 hours) were run from the 00:00 UTC analyzes. In general, the tuning had a smaller

impact in these real cycling experiments than expected in terms of verification scores, which was surprising after the firm effect in the single observation experiments. This can be explained by the fact that the single observation experiments are much closer to the simplified system (5.13)-(5.19) than the complex assimilation cycling experiments, where also the spatial correlations may play an important role. The largest impact was found for the experiment **EX2Q**, which will be referred to in the further comparison against the reference run **REFQ**. In Fig.5.9 and Fig.5.10, BIAS and RMSE scores for the analyzes are shown for the **EX2Q** and **REFQ** runs. The tuning resulted in a better (worse) fit to the observations concerning the temperature (humidity) analysis RMSE. The impact on the wind analysis is rather mixed.

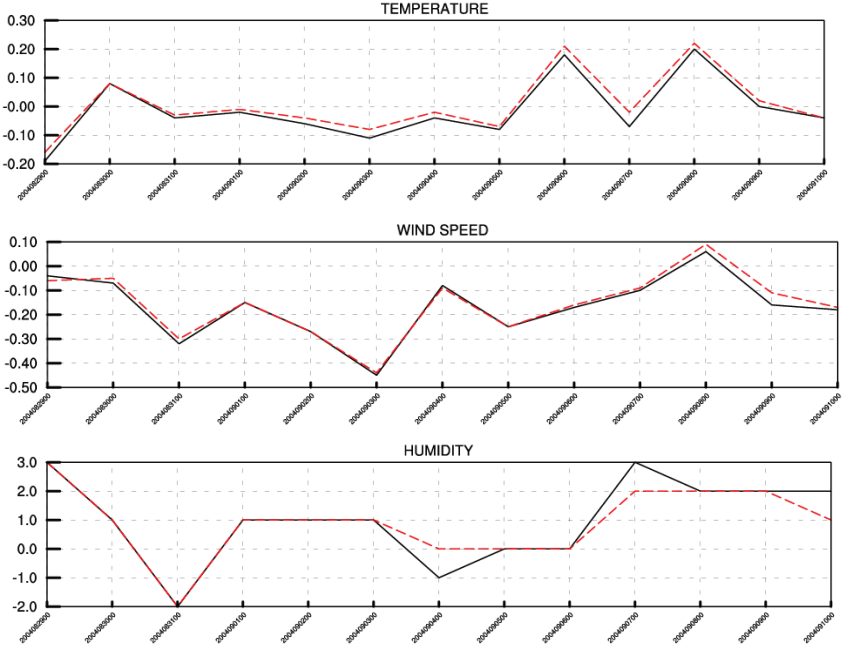

Figure 5.9: Evolution of analysis BIAS scores for the experiments **EX2Q** (solid line) and the reference **REFQ** (dashed line). Top: temperature at 850 hPa (K), Middle: wind speed at 500 hPa ($m\ s^{-1}$), Bottom: relative humidity at 700 hPa ($\%$). The scores are computed over the period August 29 - September 10, 2004.

In our explanation the good fit of temperature comes indeed from the improved multivariate analysis, namely from a larger multivariate propagation of the humidity increments into those of temperature through the process described by equation (5.14). On the other hand, the increased analysis departure of humidity may have two reasons:

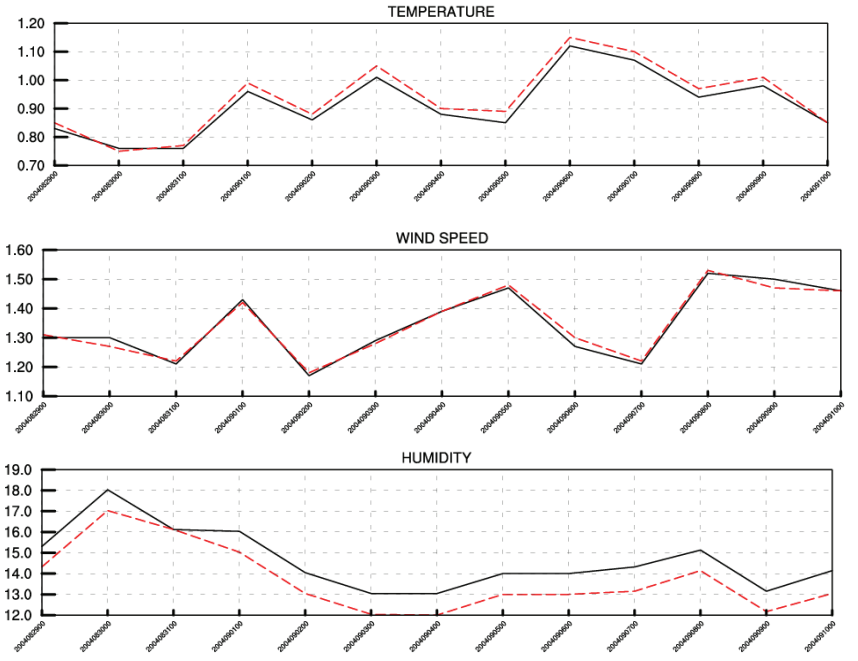

Figure 5.10: Evolution of analysis RMSE scores for the experiments **EX2Q** (solid line) and the reference **REFQ** (dashed line). Top: temperature at 850 hPa (K), Middle: wind speed at 500 hPa ($m\ s^{-1}$), Bottom: relative humidity at 700 hPa ($\%$). The scores are computed over the period August 29 - September 10, 2004.

1. Multivariate humidity increments induced by those of temperature and wind became too small by excessively decreasing $\sigma(\boldsymbol{\epsilon}_{b,q})$.

2. The univariate step of the humidity analysis equation (5.15) was degraded by reducing $\sigma(\boldsymbol{\epsilon}_{b,q})$, in spite of our compensation by reducing $\sigma(\boldsymbol{\epsilon}_{o,q})$ at the same time.

Fig.5.11 and Fig.5.12 show that the positive impact on temperature decreases quickly with the forecast range. Nevertheless, humidity 6-hour forecast scores are improved by the performed tuning both in terms of BIAS and RMSE. The impact on wind is kept mixed for this forecast range, while the overall effect of the tuning on longer forecast ranges is rather neutral (not shown).

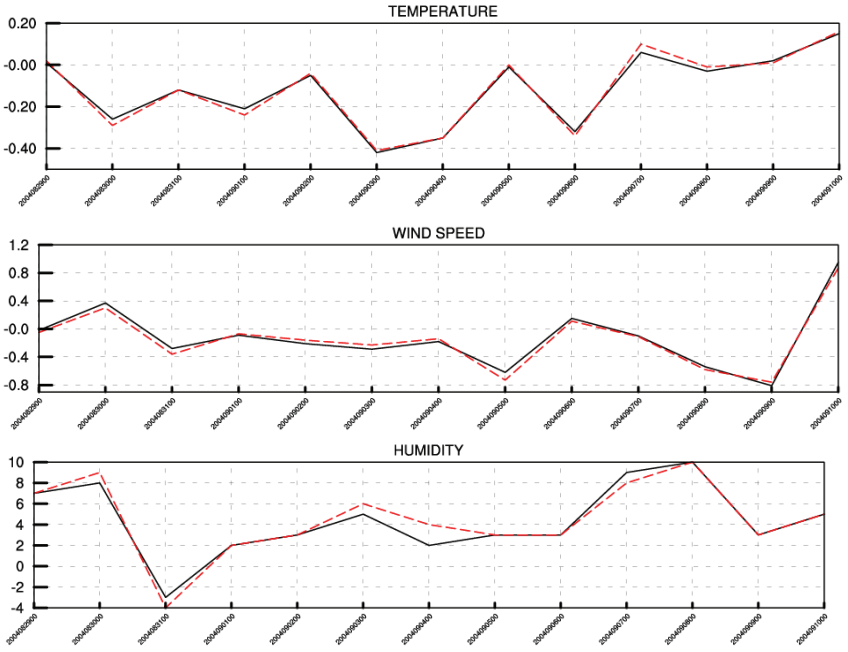

Figure 5.11: Evolution of 6 hour forecast BIAS scores for the experiments **EX2Q** (solid line) and the reference **REFQ** (dashed line). Top: temperature at 850 hPa (K), Middle: wind speed at 500 hPa ($m\ s^{-1}$), Bottom: relative humidity at 700 hPa (%). The scores are computed over the period August 29 - September 10, 2004.

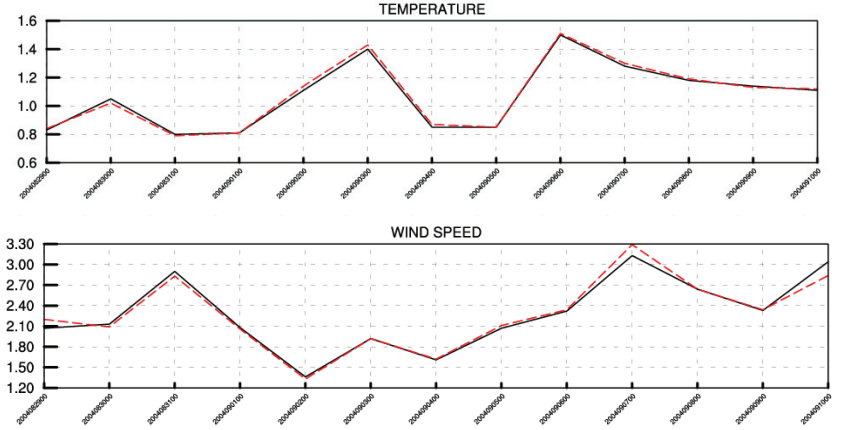

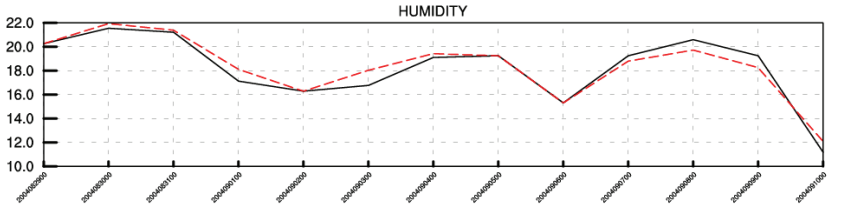

Figure 5.12: Evolution of 6 hour forecast RMSE scores for the experiments **EX2Q** (solid line) and the reference **REFQ** (dashed line). Top: temperature at 850 hPa (K), Middle: wind speed at 500 hPa ($m\ s^{-1}$), Bottom: relative humidity at 700 hPa ($\%$). The scores are computed over the period August 29 - September 10, 2004.

5.3 Discussion

Two attempts to improve the Hungarian version of the ALADIN 3DVAR analysis system were described. Both of them involve the tuning of the background and observation error standard deviations "a posteriori", but on a different theoretical basis.

The first tuning shown is based on the statistical optimality criteria derived by [22] *Désroziers et al.* (2006) and aims to tune the errors for the full set of the background variables. The tuning was applied both in a variable dependent way and also as a uniform tuning for all the variables. A clear positive impact of the uniform tuning was found, while in the variable dependent case the verification showed a degradation of the forecasts. This seems to be a contradiction, as the more complex tuning had a worse impact than the simpler one. A probable explanation of this feature is that no vertical dependence of the tuning was included in any of the experiments, but a vertically averaged tuning ratio was used instead, being a considerable limitation of the approach. It is assumed that the degrading effect of the vertical averaging appears more intensively in the variable dependent tuning if the background error of the given variable shows a large vertical dependence (i.e., in the case of temperature and humidity). The uniform tuning has been introduced in the operational ALADIN 3DVAR data assimilation system of HMS after the experiments.

The second tuning shown is based on the simplified BLUE analysis equations, proposing a modification only for the humidity errors. On the basis of single observation experiments, it was shown that the predefined error statistics produce an asymmetric multivariate balance between humidity and the other variables. Namely, humidity increments due to wind and temperature innovations are excessive compared to temperature and wind increments due to humidity innovations. On the basis of the simplified BLUE equations(5.13)-(5.19), it was derived that the asymmetry can be decreased by reducing the background error standard deviations of humidity, which was demonstrated in a set of single observation experiments. To estimate the decrease in the humidity background error standard

deviations the HL method was used ([36] *Hollingsworth and Lönnberg* 1986), which suggested a decrease of approximately half of the predefined standard deviation values on average. Full-observation experiments were performed with the modified multivariate propagation step, as well as experiments where the observation error standard deviations of humidity were also decreased to the same extent in order to keep the univariate analysis step unchanged. In real assimilation cycling experiments, the overall impact of the tuning was found to be quite moderate. This was probably caused by additional effects of spatial correlations of background errors, which were not taken into account in the simplified equations used as the basis of the tuning. However, a positive impact on 6-hour humidity forecasts was found with the application of the tuning procedure, suggesting that methodology and humidity tuning performed have a potential to improve humidity scores of numerical weather prediction models, at least for the shorter forecast ranges.

Note that the two tuning approaches described in the paper were performed independently from each other, mainly because they were motivated by independent problems. However, the two approaches are surely in a strong interaction, as both of them account for the modification of background error standard deviations. One can notice that the two tuning approaches propose to modify the humidity background error standard deviations in the opposite direction. This probably comes from the important fact that the tuning by residual covariances (Section 5.1) was based on predefined statistics sampled with the Ensemble method, while in the tuning of the multivariate balance (Section 5.2), the predefined statistics were sampled by the NMC method. Namely, background error standard deviations sampled by the Ensemble method are found to be smaller than those sampled by the NMC method ([3] *Belo Pereira and Berre* 2006, [58] *Stefanescu et al,* 2006), which may explain the seemingly opposing guidance on humidity tuning by the two tuning experiments. The change in the sampling method was due to better performance of the ALADIN 3DVAR system of HMS using the Ensemble method, which entailed also its operational use. It is, thus, desirable to repeat the tuning of the multivariate balance within the Ensemble sampling framework in the future and to see its interaction with the tuning based on residuals covariances.

Chapter 6

Improvements in the horizontal spectral representation of background errors

As mentioned in section 2.4, a spectral representation of background errors is used in the ALADIN model primarily. In this chapter two developments are presented aiming to improve two different aspects of this representation. The goal of the first development is to apply the isotropy assumption of horizontal background error correlations in a more exact way under the spectral representation. The second development aims to avoid some shortcomings in the horizontal background error correlations due to the bi-periodicity of the Fourier space.

6.1 Improving the isotropy assumption in spectral space

The content of this section was published in the ALADIN Newsletter ([7] *Bölöni et al.* 2003). Only the format is slightly modified here in order to fit to the thesis.

In the ALADIN 3DVAR scheme, background error structure functions are defined as horizontally homogeneous and isotropic in physical space. This means, that horizontal covariances are supposed to be invariant to the horizontal translation and direction, they depend thus only on the horizontal separation distance ([10] *Berre* 2000). However, due to the spectral representation of background errors, some anisotropy is implemented into the structure functions, which we illustrate on Fig.6.1. The picture shows a simple graphical test of the isotropy, namely the resulting analysis increment field (i.e. observation minus background field) of a single observation experiment. In an ideal case, isotropic increments would be fully spherical around the location of the observation. In Fig.6.1 the increment isolines are not spherical, especially at a larger distance from the location of the observation, which obviously indicates anisotropy. This section is dealing with one possible reason for the deviation of structure functions from the full isotropy and describes the experiment we have performed in order to get rid of the problem.

6.1.1 Discretisation of the isotropy assumption

As mentioned by [10] *Berre* (2000) or in chapter 2.4 of this thesis, in the ALADIN model, the covariance computations between the (m,n) spectral coefficients of the background errors are greatly simplified because of the homogeneity assumption. For example, for a given variable x the covariance is computed as:

$$cov(x_{m,n}, x_{m',n'}) = \delta_m^{m'} \delta_n^{n'} cov(x_{m,n}, x_{m,n}) = \delta_m^{m'} \delta_n^{n'} \sigma^2(x_{m,n}) \tag{6.1}$$

where $\delta_m^{m'}$ is the Kronecker delta. It means, that only the covariances between the same (m,n) pairs are considered. The isotropy assumption is applied then by an averaging of the $\sigma^2(x_{m,n})$ spectral variances over the (m,n) pairs corresponding to the same $k^*_{m,n}$ total wavenumber, that is:

$$k^*_{m,n} = N\sqrt{\left(\frac{m}{M}\right)^2 + \left(\frac{n}{N}\right)^2} \tag{6.2}$$

where M and N are the maximum wavenumbers in x and y directions. As a consequence, the covariances are not any more dependent on m and n separately, which ensures the invariance to the horizontal direction in physical space. The problem here is that the different (m,n) pairs never correspond exactly to the same real $k^*_{m,n}$ value, so within the averaging a discretisation of the real $k^*_{m,n}$ total wavenumber vector and the real $\sigma^2(x_{m,n})$ variance spectrum is introduced as follows next. Let's denote by k^*_i the nearest integer to the real $k^*_{m,n}$ total wavenumber ($k^*_i = 0, 1, ..., N$). The average mentioned above determines the isotropic spectral variance spectrum in the function of the k^*_i integer total wavenumber vector:

$$\sigma^2(x_{k^*_i}) = \frac{1}{J} \sum_{m=0}^{M} \sum_{n=0}^{N} \sigma^2(x_{m,n}) \tag{6.3}$$

for which,

$$k^*_{m,n} = k^*_i \pm \epsilon. \tag{6.4}$$

In (6.3) J is the number of (m,n) pairs for which (6.4) is true and ϵ is a constant real number specifying the half interval for which the isotropic average above is done. As a consequence the B matrix finally consists of a set of isotropic spectral variances representing horizontal scales corresponding to the k^*_i integer total wavenumber vector.

On the other hand, in the J_b part of the 3DVAR code, the change of variable $\chi = B^{-1/2}\delta x$ ([25] *Fischer* 2002) is done for the usual spectral coefficients corresponding to (m,n) wave pairs and not to the integer total wavenumbers k^*_i. It is clear then, that an inevitable estimation of the real $\sigma^2(x_{m,n})$ variances should be done from the available $\sigma^2(x_{k^*_i})$ isotropic variances, in order to do the following normalization:

$$\chi_{m,n} = \delta x_{m,n} / \hat{\sigma}(x_{m,n}), \tag{6.5}$$

where $\hat{\sigma}(x_{m,n})$ is the square-root of $\hat{\sigma}^2(x_{m,n})$, which is the estimation of the real $\sigma^2(x_{m,n})$. The presently used estimation, is very simple, namely

$$\hat{\sigma}^2(x_{m,n}) = \sigma^2(x_{k_i^*}) \tag{6.6}$$

where k_i^* is the nearest integer to the given $k_{m,n}^*$.

An other thing to be considered is how the normalization above acts in case of a rectangular domain. If the domain is rectangular, that is $M \neq N$, then

$$k_{m,n}^* \neq k_{n,m}^* \tag{6.7}$$

with

$$m \neq n \qquad m = 0, ..., M \qquad n = 0, ..., N. \tag{6.8}$$

Substituting into (6.2), one can easily see that $k_{0,1}^* = 1$ and $k_{1,0}^* = N/M$ for example, which means that having only one wave in x or y directions leads to total wavenumbers that differ by the N/M ratio. On the other hand, using the estimation (6.6) in (6.5), the normalization for $\delta x_{m,n}$ and $\delta x_{n,m}$ will be done both by the same $\sigma^2(x_{k_i^*})$ variance, because $k_{m,n}^*$ and $k_{n,m}^*$ are corresponding to the same k_i^* value. It is a rough approximation of the isotropy assumption, because x is assumed to have the same variance on both horizontal scales corresponding to (m, n) and (n, m). On the contrary, the exact isotropy would rather mean that only those spectral variables were normalized with the same variance, which are corresponding to (m, n) wavenumber pairs, which belong exactly to the same $k_{m,n}^*$ total wavenumber.

6.1.2 Experiment with a new isotropy assumption

The goal of this experiment was to try to make the approximation of the isotropy assumption more realistic by applying the following estimation of $\sigma^2(x_{m,n})$ instead of (6.6):

$$\hat{\sigma}^2(x_{m,n}) = \sigma^2(x_{k_i^*})\frac{k_{i+1}^* - k_{m,n}^*}{k_{i+1}^* - k_i^*} + \sigma^2(x_{k_{i+1}^*})\frac{k_{m,n}^* - k_i^*}{k_{i+1}^* - k_i^*} \tag{6.9}$$

which is a linear interpolation between the two neighboring $\sigma^2(x_{k_i^*})$ variances of the given $\sigma^2(x_{m,n})$. Note, that taking into account that $(k_{i+1}^* - k_i^* = 1)$, the interpolation above can be written in a simpler form:

$$\hat{\sigma}^2(x_{m,n}) = \sigma^2(x_{k_i^*})(k_{i+1}^* - k_{m,n}^*) + \sigma^2(x_{k_{i+1}^*})(k_{m,n}^* - k_i^*) \tag{6.10}$$

In Fig.6.2 one can see the result of the same single observation experiment as shown in Fig.6.1, but using the interpolation above instead of the original nearest integer estimation. It is noticeable, that the increment isolines are closer to be spherical at a larger distance from the observation, in comparison

with Fig.6.1, however the shape of the increments is not visually changed near the observation point. The same features were observed making comparison of vertical cross-sections.

In order to be able to make a more reliable comparison of the isotropic properties of the analysis increments, we have prepared a simple tool that measures quantitatively the degree of anisotropy. We have defined the measure of the anisotropy by the absolute value of the ratio

$$\frac{\delta x_{dx}}{\delta x_{dy}}, \tag{6.11}$$

where δx_{dx} and δx_{dy} are the analysis increment values, at the same d horizontal distance from the observation point, in x and y directions (Fig.6.3). The result of this diagnostic, comparing the (6.6) and (6.9) estimations is shown on the right side of Fig.6.3. The two most obvious things that one can see on the plot, are that the degree of anisotropy is increasing with the distance for both experiments and that for a given distance the degree of anisotropy is smaller for the experiment using the linear interpolation of the $\sigma^2(x_{k_i^*})$ variances than for the one using the nearest integer estimation.

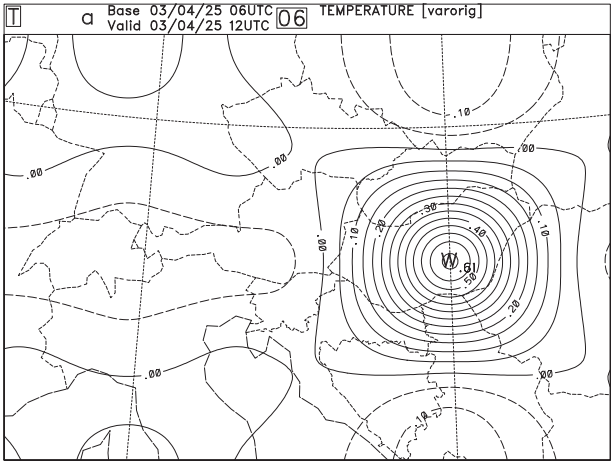

Figure 6.1: Temperature analysis increment field on model level 16, due to a temperature single observation at 500 hPa. Original implementation of the isotropy assumption

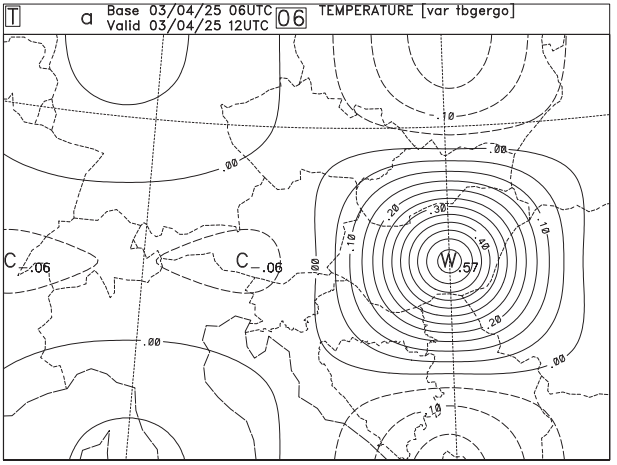

Figure 6.2: Temperature analysis increment field on model level 16, due to a temperature single observation at 500 hPa. Improved implementation of the isotropy assumption

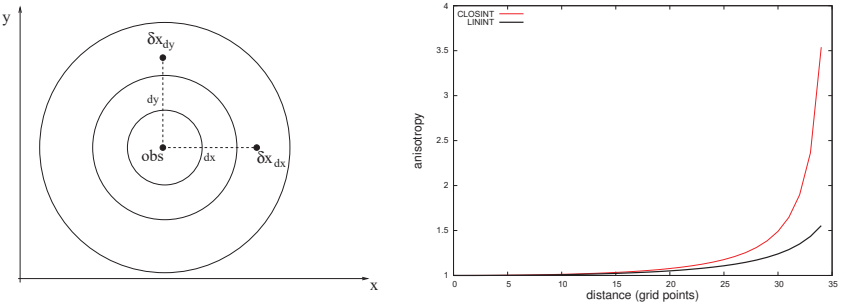

Figure 6.3: Left: a visual interpretation of the chosen diagnostic to measure anisotropy ($\delta x_{dx}/\delta x_{dy}$), which is the ratio of analysis increments at a given distance from the observation in x and y directions. Right: Degree of anisotropy in the function of horizontal distance (number of grid-points). CLOSINT: nearest integer estimation (equation (6.6)), LININT: linear interpolation (equation (6.9))

6.2 Improving the sampling of background error forecast differences in the spectral representation

Background errors are sampled from forecast differences as discussed in chapter 3. In case of the ALADIN model these differences are created in spectral space given the fact that the J_b part of the ALADIN variational cost function is mostly computed in spectral (Fourier) space, as presented in section 2.4. The transformation of meteorological fields between the grid-point and the spectral spaces requires bi-periodic fields in both x and y directions, however applying the model dynamics and physics, the bi-periodicity is not necessarily fulfilled. As a solution, the extension zone is defined (Fig.2.1), where a smooth transition of the fields to those of the opposite side of the domain is ensured before each transformation from grid-point to spectral space. The spectral forecast differences include also information from the grid-point fields of the extension zone through the direct Fourier transform. These contributions are fully artificial and have no meteorological meaning. With other words, the direct Fourier transform introduces waves in the spectral forecast differences, which are partly based on the non-physical grid-point values of the extension zone. This may affect all computations in spectral space, especially in case of large extension zones, i.e. when the number of grid-points of the extension zone becomes comparable with the full number of grid-points in one horizontal direction. This section discusses the above problematics with a special emphasis on the background error computations.

6.2.1 Necessity of a large extension zone and related difficulties

The default size of the extension zone in the ALADIN model is 11 grid-points in both x and y directions. A recent track of research related the ALADIN code is to use a larger extension zone than that. Using a large extension zone is a potential cure of a long standing shortcoming of the horizontal analysis increment propagation in the ALADIN model. This shortcoming is the bi-periodic propagation of analysis increments as also seen in Fig.6.1 and 6.2. It is sensible in the figures that the analysis increment due to the observation placed over Hungary reduces quasi-isotropically to zero, but additionally also produces increments on the domain borders in both horizontal directions. This problem originates from the spectral construction of the ALADIN variational code (and especially J_b), which, as explained, involves bi-periodicity through the Fourier transforms. As mentioned, besides several other attempts (*Claude Fischer personal communication*), one way to go to avoid the periodic increments is to enlarge the extension zone in a manner that it becomes larger than horizontal correlation length-scales. On the other hand, the difficulty of sampling using large extension zones (described at the beginning of the section) has to be considered, otherwise artificial noise may be introduced to the background error covariance matrix. Indeed, background error statistics and diagnostics sampled

from forecast differences with large extension zones turned out to be rather noisy and suspicious, based on the experience of the Swedish NWP team (*Magnus Lindskog personal communication*).

6.2.2 Experiments by suppressing the effect of the extension zone from the background error sampling

In order to diagnose, how much the grid-points in the extension zone affect the background error computations, the following experiment was done. The software for forecast difference creation was modified in order to nullify the forecast differences in the extension zone. To do this, after taking the difference of spectral fields of both forecasts in play, an inverse Fourier transform is applied, on the difference fields which brings the meteorological information to grid-point space. The grid-points located in the extension zone are identified and their values are replaced by zero. This is followed by a direct Fourier transform, which brings the forecast differences back to spectral space but without any contribution from the artificial information of the extension zone. One has to add, that in order to be able to apply the direct Fourier transform back to spectral space, the suppression of differences in the extension zone should be done so that bi-periodicity still holds. This is achieved by defining

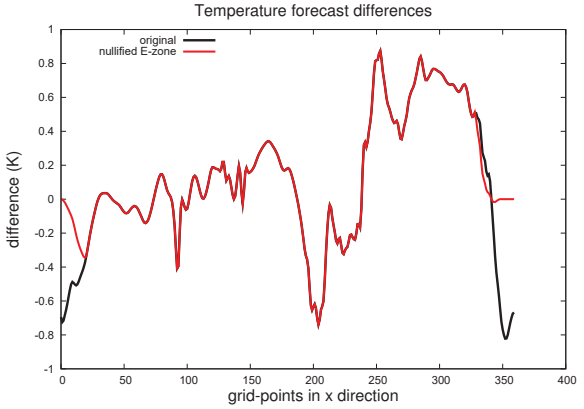

Figure 6.4: Temperature forecast difference values (K) of ALADIN/HU in the grid-points along the x direction at a chosen latitude (y=100) including the extension zone. Black: with the original code including differences in the extension zone, Red: with nullified values in the extension zone

a transition zone along the domain boundaries, in which a 2 dimensional mask ensures a smooth transition of the fields in the $C + I$ zones (Fig.2.1) to zero towards the extension zone (i.e. towards North and East) and also towards the opposite directions (West and South). The definition of the

2 dimensional mask was already introduced in the ALADIN code by [25] *Fischer* (2002), which enabled a simple implementation of the above procedure.

As a test of the above code modification, the temperature difference of two arbitrary forecasts was plotted along the grid-points in the x direction of the ALADIN/HU domain through the $C+I$ and E zones for a selected y coordinate (Fig.6.4). It is sensible from the figure, that in a large part of the $C+I$ zones the grid-point values are the same for the original and for the modified forecast differences. On the other hand, both in the West (left) and in the East (right) sides of the domain, the modified grid-point values smoothly tend to zero from the inner- towards the outer-edge of the transition zone (which is the inner-edge of the E zone in the North and in the East). In the E zone, the values are fully zeroes. Note, that in the experiments, the transition zone was chosen to include 20 grid-points in each direction along the boundaries of the $C+I$ zones, and the E zone included 11 grid-points.

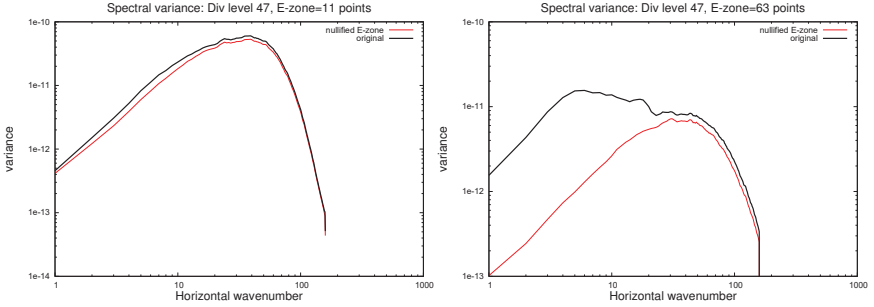

Figure 6.5: Spectra of divergence background error variances (s^{-1}) at $\approx$ 1000 hPa (model level 47) computed on a 10 day sample. Black: forecast differences were computed with the original code including differences in the extension zone, Red: forecast differences were computed with nullified values in the extension zone. Left: small extension zone (11 grid-points), Right: large extension zone (63 grid-points)

After the verification of the above procedure, the effect on the background error statistics was evaluated. To do this, a small sample (10 elements) of forecast differences were prepared with both the original and the modified forecast difference sampling. Based on both samples, background error covariance matrices were computed and diagnosed. The test was performed both with small (11 grid-points) and large (63 grid-points) extension zones. Fig.6.5 demonstrates the results from the test showing spectra of background error variances for divergence at $\approx$ 1000 hPa (model level 47). It can be seen, that using a small extension zone, the spectra of variance obtained with the modified

sampling (i.e. the suppression of forecast differences from the extension zone) does not differ much from those obtained with the original sampling. On the other hand, in case of a large extension zone, the modification of the sampling does make a huge effect on the spectra of variance, especially on the large scales, where the original sampling results in rather erroneous variance spectrum. This shows, that the artificial contribution to the spectral differences from the extension zone points affect mostly the long waves (large scales).

6.3 Discussion

Two attempts to improve the spectral representation of background errors in the ALADIN model were described in the present chapter. The first one aimed to improve the implementation of the isotropy assumption for horizontal background error covariances. This proved to be partly successful, as the proposed modifications resulted in somewhat more isotropic analysis increments, however the difference from those obtained with the original code were small. As a consequence, this development was not included into the reference version of the ARPEGE/ALADIN code.

The second attempt aimed to improve the spectral representation of background errors by suppressing artificial information of the extension zone. The proposed technical development was indeed successful in removing suspicious, artificial features of background error covariances, which appear mainly in case of large extension zones. The related code modifications are proposed to be included into the reference version of the ARPEGE/ALADIN code.

Chapter 7

Discussion and Conclusions

The thesis is dealing with the estimation and modeling of background errors in a LAM framework. The related work included numerical experiments with the ALADIN LAM NWP model and especially its data assimilation (3 dimensional variational assimilation) counterpart. Related to some of the aspects discussed in the thesis, scientific and technical developments on the background error estimation and data assimilation codes of the ALADIN model have been assessed. After introducing the reader into data assimilation and background error modeling in chapter 2, specific aspects of these science areas were discussed in more detail with the following results.

Chapter 3 discussed the error simulation (sampling) techniques applied in LAM assimilation systems, as well as the contribution of different uncertainties (i.e. analysis, lateral boundary and model uncertainties) to the full background forecast uncertainty. All these sources of background forecast uncertainties have been diagnosed separately and have been compared with each other. It was found that, given the short range of background forecasts (6 hours), the analysis uncertainty and the model uncertainty have more important contributions to the full background errors than the uncertainty in the lateral boundary conditions. Two different representations of the analysis uncertainty in the background error computations have been compared, namely the dynamical downscaling of analysis uncertainty from global models (use of global Ensemble Assimilation systems for sampling) and a direct representation of the LAM analysis uncertainty itself (use of a LAM Ensemble Assimilation system for sampling). The latter was found to be more efficient to represent LAM background errors both in terms of a direct diagnosis and in terms of verification scores coming from assimilation and forecast experiments applying the relevant background error covariance matrices. The representation of uncertainty in the lateral boundary conditions was assessed by coupling the LAM error simulation experiments to global ensemble assimilation systems. An attempt has been made to represent model errors in the background error simulation procedure. This was done by introducing model physics perturbations into the error simulation runs, assuming that an important part of the model error originates from the imperfections of physical parametrizations. The physics perturbations resulted in

reasonable additional simulated error structures compared to the perfect model approach. The background error covariance matrix involving the additional representation of model errors was tested in real assimilation and forecast experiments, showing an ability to improve short range forecasts of certain parameters.

The weather dependence or time variability of background errors has been studied in chapter 4, within a simplified framework. Namely, the seasonal and diurnal variability of background error diagnostics has been assessed by running background error simulation experiments over different seasons and valid for different times of the day (monthly aggregates). For the investigation of the seasonal variability, background error diagnostics have been compared based on a summer and a winter error simulation period. Background errors of the summer period were found to be larger than those of winter, especially on small spatial scales and close to the ground surface (i. e. in the PBL), which was attributed to more active (and less predictable) convective processes during the summer. A sensitivity of the forecast quality to the seasonal variability of background errors was noticed. The representation of this variability however did not lead to clearly better forecasts according to experiments done. The diurnal variability of background errors was assessed by sampling and comparing diagnostics of two background error covariance matrices based on simulated errors valid at night- and day-times (i.e. at 00 and 12 UTC). Background errors valid at day-time were found to be larger than those valid at night-time, especially for small scales and for the lower troposphere. Again, this difference was interpreted by more active convection during day-time than during night. An improvement of the forecast was found for some parameters due to the representation of the diurnal variability of background errors, however some other parameters were degraded by, or found to be rather insensitive to such changes in the assimilation system. This suggests that instead of using monthly (climatological) aggregates for sampling, probably a more advanced, real flow dependent framework (e.g. Ensemble Kalman Filtering, Ensemble of Variational Data Assimilations) is needed for a proper representation of the time variability in background errors.

It was shown in chapter 5, that an "a posteriori" diagnosis and tuning of background errors is important, given the fact that not any error simulation technique is perfect. Two approaches for the "a posteriori" tuning were applied and presented in this chapter. The first one was applied on all analysis variables and was based on criteria of the optimal estimation theory. The second one was applied on humidity (especially on the multivariate propagation of its analysis increments into increments of other variables) and was based on rather empirical considerations. It was shown that both "a posteriori" tuning trials were successful in improving the analyzes and forecasts of the ALADIN model.

Chapter 6 described two independent attempts to improve the spectral representation of background errors in the ALADIN assimilation system. The first one tackled the implementation of the isotropy assumption within the spectral construction of the background error covariances. This included a more exact, and less orientation dependent normalization with spectral background error standard deviations within the ALADIN 3DVAR code. This modification, however, did bring only

very slight improvements, i.e. it lead to very slightly more isotropic analysis increments. The second development aimed to suppress noise from the background errors, which were due to the propagation of artificial grid-point field values from the extension zone to the spectral forecast differences used for sampling (background error simulation) through the direct Fourier transform. It was shown that this noise is relevant only in case of large extension zones (i.e. when the number of grid-points in the extension zone is comparable with those of the full model domain in one direction), and the replacement of forecast differences in the extension zone by zero values was proposed in order to get rid of it. The modification was tested on a small size sample and it was shown that it removes the unwanted noise from the background error statistics.

Bibliography

[1] Adamcsek, E., Bölöni, G., Csomós, P. and Horányi, A., 2010: Application of the Ensemble Transform Kalman Filter technique at the Hungarian Meteorological Service: Preliminary results. *Időjárás*, **114**, 21-37.

[2] Andersson, E., Haseler, J., Undén, P. Courtier, P., Kelly, G., Vasiljevic, D., Brankovic, C. Gaffard, C., Hollingsworth, A., Jakob, C., Janssen, P., Klinker, E., Lanzinger, A., Miller, M., Rabier, F., Simmons, A., Strauss, B., Viterbo, P., Cardinali, C., Thépaut, J-N., 1988: The ECMWF implementation of three-dimensional variational assimilation (3D-Var). III: Experimental results. *Q J Roy Meteor Soc*, **124**, 1831-1860.

[3] Belo Pereira, M. and Berre, L., 2006: The use of an ensemble approach to study the background error covariances in a global NWP model. *Mon Weather Rev*, **134**, 2466-2489.

[4] Bishop, C. H., Etherton, B. J.and Majumdar, S. J., 2001: Adaptive sampling with the Ensemble Transform Kalman filter. Part I: Theoretical aspects. *Mon Weather Rev*, **129**, 420-436.

[5] Bouttier, F. and Courtier, P., 1999: Data Assimilation concepts and methods. *ECMWF Lecture Series: Data assimilation and use of satellite data*, 72 pp.

[6] Bölöni, G., 2001: Az ALADIN modell adatasszimilációban alkalmazható elörehelzési hibastatisztikáinak vizsgálata. *Diplomamunka*, ELTE-TTK, Meteorológiai Tanszék 65 pp.

[7] Bölöni, G., C. Fischer and L. Berre, 2003: (An)isotropy of background error structure functions. *ALADIN Newsletter* **25**, 48-50.

[8] Bölöni, G., 2006: Development of a variational data assimilation system for a limited area model at the Hungarian Meteorological Service. *Időjárás*, **110**, 309-327.

[9] Bölöni, G. and K. Horvath, 2010: Diagnosis and tuning of background error statistics in a variational assimilation system. *Időjárás*, **114**, 1-21.

[10] Berre, L., 2000: Estimation of Synoptic and Mesoscale Forecast Error Covariances in a Limited-Area Model. *Mon Weather Rev*, **128**, 644-667.

[11] Berre, L., 2001: Représantation des Covariances Spatiales des Erreurs de Prévisions pour une Assimilation Variationelle dans un Modèle Atmospherique à Aire Limitée. *Ph.D. thesis, Université de Toulouse III. - Paul Sabatier*, 250 pp.

[12] Berre, L., Stefanescu, E.S. and Belo Pereira, M., 2006: The representation of the analysis effect in three error simulation techniques. *Tellus*, **58**, 196-209.

[13] Bougeault, P., 1985: Parametrization of cumulus convection for GATE. A diagnostic and semi-prognostic study. *Mon Weather Rev*, **113**, 2108-2121.

[14] Bubnová, R., Horányi, A. and Malardel, S., 1993: International project ARPEGE/ALADIN. *EWGLAM Newsletter* **22**, 117-130.

[15] Buhner M., 2005: Ensemble-derived stationary and flow-dependent background-error covariances: Evaluation in a quasi-operational setting. *Q J Roy Meteor Soc*, **131**, 1013-1043.

[16] Chapnik, B., Désroziers, G., Rabier, F., Talagrand, O., 2004: Properties and first application of an error- statistics tuning method in variational assimilation. *Q J Roy Meteor Soc*, **130**, 2253-2275.

[17] Courtier, P., Andersson, E., Heckley, W., Pailleux, J., Vasiljevic. D., Hamrud, M., Hollingsworth, A., Rabier, F., and Fisher, M., 1998: The ECMWF implementation of three dimensional variational assimilation (3D-Var). Part I: Formulation. *Q J Roy Meteor Soc*, **124**, 1783-1808.

[18] R. Czelnai, L. S. Gandin, W. I. Zachariew, 1976: Statistische Struktur der Meteorologischen Felder. *Országos Meteorológiai Szolgálat hivatalos kiadványai*, **XLI** kötet

[19] Daley, R., 1991: Atmospheric Data Analysis. Cambridge, Atmospheric and Space Science Series, 457 pp.

[20] Davies, H.C, 1976: A lateral boundary formulation for multi-level prediction models. *Q J Roy Meteor Soc*, **102**, 405-418.

[21] Deckmyn A. and Berre, L., 2005: A Wavelet Approach to Representing Background Error Covariances in a Limited-Area Model., *Mon Weather Rev*. **133**, 1279-1294.

[22] Désroziers, G., Berre, L., Chapnik, B. and Poli, P., 2006: Diagnosis of observation, background and analysis error statistics in observation space. *Q J Roy Meteor Soc*, **131**, 3385-3396.

[23] Désroziers, G. and S. Ivanov, 2001: Diagnosis of adaptive tuning of information error parameters in a variational assimilation. *Q J Roy Meteor Soc*, **127**, 1433-1452.

[24] Evensen, G., 1994: Sequential data assimilation with a nonlinear quasi-geostrophic model using Monte Carlo methods to forecast error statistics. *J Geo Res*, **99 C 5**, 10,143-10,162.

[25] Fischer, C., 2002 : The variational computation inside ARPEGE/ALADIN cycle CY25T1. *ALADIN Technical documentation*, 59 pp.

[26] Fischer, C., Montmerle, T., Berre, L., Auger, L., Stefanescu, S. 2005: An overview of the variational assimilation in the Aladin/France numerical weather prediction system. *Tellus*, **131**, 3477-3492.

[27] Fisher, M., 1998: Development of a simplified Kalman filter. *ECMWF Technical Memorandum*, No. 260.

[28] Fisher, M., 2003: Background error covariance modelling. *Proceedings of the ECMWF seminar on Recent developments in data assimilation for atmosphere and ocean, Reading*, 45-63.

[29] Gandin, L.S, 1963: Objective analysis of meteorological fields. *Gidrometeorologicheskoe Izdatelstvo*, Leningrad, English translation by Israeli Program for Scientific Translations, Jerusalem, 1965, 242 pp.

[30] Geleyn, J-F., 1987: Use of a modified Richardson number for parametrizing the effect of shallow convection. *J. Meteor. Soc. Japan., Special NWP Symposioum issue*, 141-159.

[31] Geleyn, J-F., Catry, B., Bouteloup, Y. and Brozková, R., 2008: A statistical approach for sedimentation inside a micro-physical precipitation scheme. *Tellus*, **60A**, 649-662.

[32] Gerard, L., 2007: An integrated package for sub-grid convection, cloud and precipitation compatible with the meso-omega scales. *Quart. J. Roy. Meteor. Soc.*, **133**, 711-730.

[33] Gerard, L., Piriou, J. M., Brozková, R. Geleyn, J-F. and Banciu D., 2009: Cloud and Precipitation Parameterization in a Meso-Gamma-Scale Operational Weather Prediction Model. *Mon. Wea. Rev.*, **137**, 3960-3977.

[34] Götz G. and F. Rákóczi, 1981: A dinamikus meteorológia alapjai. Budapest, *Tankönyvkiadó*, 483 pp.

[35] Gustaffson, N., Berre, L., Hörnquist, S., Huang, X.-Y., Lindskog, M., Navascués, B., Mogensen, K.S., and Thorsteinnson, S., 2001: Three-dimensional variational data assimilation for a limited area model. Part I: General formulation and the background error constraint. *Tellus*, **53A**, 425-446.

[36] Hollingsworth, A. and Lönnberg, P., 1986: The statistical structure of short-range forecast errors as determined from radiosonde data. Part I. The wind field. *Tellus*, **38A**, 111-136.

[37] Hollingsworth A., 1987: Objective analysis for numerical weather prediction. Short and medium-range numerical weather prediction. *Proceedings of the WMO/IUGG NWP Symp., Tokyo*, Meteorological Society of Japan, 11-59.

[38] Holton, J. K., 2004: An Introduction to Dynamic Meteorology., London, 4th edition, *Elsevier Academic Press*, 529 pp.

[39] Horányi, A., Ihász, I. and Radnóti, G., 1996: ARPEGE/ALADIN: a numerical weather prediction model for Central-Europe with the participation of the Hungarian Meteorological Service. *Időjárás*, **100**, 277-301.

[40] Houtekamer P.L., Mitchell H.L. and Deng X., 2009: Model Error Representation in an Operational Ensemble Kalman Filter. *Mon Weather Rev*, **137**, 2126-2143.

[41] Isaksen L., Fisher M. and Berner, J., 2007: Use of analysis ensembles in estimating flow-dependent background error variance. *Proceedings of ECMWF Workshop on Flow-dependent aspects of data assimilation, 11-13 June 2007, Reading*, 65-86.

[42] Joly, A., 1992: ARPEGE/aladin: adiabatic model equations and algorithm. *Météo-France Technical Memorandum*, available from the author of this thesis or from the Météo-France GMAP team

[43] Kalman E. R., 1960: A new approach to linear filtering and prediction problems. *Journal of Basic Engineering*, **82**, 35-45.

[44] Kalnay, E., 2003: Atmospheric Modeling, Data Assimilation and Predictability. *Cambridge University Press*, 341 pp.

[45] Kessler, E., 1995: On the continuity and distribution of water substance in atmospheric circulations. *Atm. Research*, **38**, 109-145.

[46] Li, H., Kalnay, E., Miyoshi, T., Danforth, C.M., 2009: Accounting for model errors in Ensemble Data Assimilation. *Mon Weather Rev*, **137**, 3407-3419.

[47] Lorenc, A.C., 1986: Analysis methods for numerical weather prediction. *Q J Roy Meteor Soc*, **112**, 1177-1194.

[48] Lönnberg, P. and Hollingsworth, A., 1986: The statistical structure of short-range forecast errors as determined from radiosonde data. Part II: The covariance of height and wind errors. *Tellus*, **38A**, 137-161.

[49] Lynch, P. and Huang, X-Y, 1992: Initialization of the HIRLAM model using a Digital Filter. *Mon Weather Rev*, **120**, 1019-1034.

[50] Monteiro, M. and Berre, L., 2010: A diagnostic study of time variations of regionally-averaged background error covariances. *Journal of Geoph. Res.*, **115**, 1-14.

[51] Parrish, D. F. and Derber, J. C., 1992: The National Meteorological Centre's spectral statistical interpolation system. *Mon Weather Rev*, 1747-1763.

[52] Práger T., 1982: Numerikus prognosztika I.: A hidrodinamikai elörejelzés története, Budapest, *Tankönyvkiadó*, 327 pp.

[53] Rabier, F., E. Andersson, A. McNally, P. Courtier, P. Undén, J. Eyre, A. Hollingsworth, F. Bouttier, 1998: The ECMWF implementation of three-dimensional variational assimilation (3D-Var). II: Structure functions. *Q J Roy Meteor Soc*, **124**, 1809-1829.

[54] Radnóti, G. and coauthors, 1995: The spectral limited area model ARPEGE/ALADIN. *PWPR Report series* **7**, *WMO-TD* **699**, 111-117.

[55] Randriamampianina, R., 2006: Impact of high resolution observations in the ALADIN/HU model. *Idöjárás* **110**, 329-349.

[56] Sadiki, W. and Fischer, C., 2005: A posteriori validation applied to the 3D-VAR ARPEGE and ALADIN data assimilation system. *Tellus*, **57A**, 21-34.

[57] Siroká, M., Fischer, C., Cassé, V., Brozková, R. and Geleyn, J-F., 2003: The definition of mesoscale selective forecast error covariances for a limited area variational analysis. *Meteor Atmos Phys*, **82**, 227-244.

[58] Stefanescu, S.E., Berre, L., and Belo Pereira, M., 2006: The evolution of dispersion spectra and the evaluation of model differences in an ensemble estimation of error statistics for a limited area analysis. *Mon Weather Rev*, **134**, 3456-3478.

[59] Storto A. and Randriamampianina R., 2010: Ensemble variational assimilation of background error covariances in a high-latitude regional model. *Journal of Geophys. Res.*, **115**, D17.

[60] Talagrand, O., 1998: A posteriori evaluation and verification of analysis and assimilation algorithms., *Workshop on Diagnosis of Data Assimilation Systems, 2-4 November 1998, ECMWF*, 17-18.

[61] Thépaut, J.-N. and P. Courtier, 1991: Four-dimensional data assimilation using the adjoint of a multilevel primitive equation model. *Q J Roy Meteor Soc*, **117**, 1225-1254.

[62] Vána, F., Bénard, P., Geleyn, J-F, Simon A. and Seity Y., 2008: Semi-Lagrangian advection scheme with controlled damping: An alternative to nonlinear horizontal diffusion in a numerical weather prediction model. *Q J Roy Meteor Soc*, **134**, 523-537.

[63] Zupanski, D. and Zupanski, M., 2006: Model Error Estimation Employing an Ensemble Data Assimilation Approach. *Mon Weather Rev*, **134**, 1337-1354.

[64] Wei M., and Tóth Z., 2003: A New Measure of Ensemble Performance: Perturbation versus Error Correlation Analysis (PECA). *Mon Weather Rev*, **131**, 1549-1565.

[65] Wilks, D.S., 1995: Statistical Methods in the Atmospheric Sciences. *Academic Press, San Diego, California*, 467 pp.